ABSTRACT

SEARCH FOR CHARGED HIGGS BOSONS IN THE τ+LEPTON FINAL STATE WITH 36.1 fb^{-1} OF PP COLLISION DATA RECORDED AT $\sqrt{S} = 13$ TEV WITH THE ATLAS EXPERIMENT

Blake Burghgrave, Ph.D.
Department of Physics
Northern Illinois University, 2018
Dhiman Chakraborty, Director

This dissertation describes a search for charged Higgs bosons decaying to a tau and a neutrino ($H^+ \rightarrow \tau^+ \nu_\tau$ or the charge-conjugate process) in association with a leptonically decaying top quark, using 36.1 fb^{-1} of pp collision data collected with $\sqrt{s} = 13$ TeV by the ATLAS detector. The theoretical motivation, including a review of the Standard Model, is given, along with a description of the ATLAS detector and particle reconstruction. A multi-variate analysis approach uses stochastic gradient boosted decision trees to improve the separation between $H^\pm$ signal and background. The semi-leptonic channel described in this thesis is used in combination with a fully hadronic channel to search for charged Higgs bosons in a mass range of 90 GeV $\leq m_{H^\pm} \leq$ 2000 GeV. Finding no significant excess, limits are set at the 95% confidence level on the charged Higgs production cross section times the branching fraction into $\tau\nu$ ranging from 4.2 pb to 2.5 fb. These limits are interpreted in the hMSSM benchmark scenario as an exclusion at 95% confidence on $\tan\beta$ as a function of $m_{H^\pm}$. In this scenario, for $\tan\beta = 60$, the $H^\pm$ mass range up to 1100 GeV is excluded, with all values of $\tan\beta$ exclude for $m_{H^\pm} \lesssim 160$ GeV.

NORTHERN ILLINOIS UNIVERSITY

DE KALB, ILLINOIS

AUGUST 2018

SEARCH FOR CHARGED HIGGS BOSONS IN THE τ+LEPTON FINAL STATE WITH 36.1 fb^{-1} OF PP COLLISION DATA RECORDED AT $\sqrt{S} = 13$ TEV WITH THE ATLAS EXPERIMENT

BY

BLAKE BURGHGRAVE

© 2018 Blake Burghgrave

A DISSERTATION SUBMITTED TO THE GRADUATE SCHOOL

IN PARTIAL FULFILLMENT OF THE REQUIREMENTS

FOR THE DEGREE

DOCTOR OF PHILOSOPHY

DEPARTMENT OF PHYSICS

Dissertation Director:
Dhiman Chakraborty

ProQuest Number: 10839888

ProQuest 10839888

ACKNOWLEDGEMENTS

First of all, I would like to thank my advisor, Dhiman Chakraborty, for his wisdom and guidance these past years. He introduced me to nearly every topic described in this thesis, a host of others, and encouraged me to work on each contribution described later in the text.

Serban Protopopescu has earned a heartfelt thanks for acting in a similar role during a fellowship at Brookhaven National Lab, where the lion's share of my work on the MVA analysis occurred. Thanks also to Michael Begel for acting as my official host while at the lab.

I would also like to thank everyone from the NIU ATLAS group during my time as a grad student. Extra thanks go to Pawel Klimek for organizing the $H^\pm \to \tau\nu$ analysis and for his help on the $\tau + \ell$ channel, to Jahred Adelman and Liza Brost for their thoughtful comments, to Jerry Blazey and Adam Yurkewicz for their help on my authorship qualification task, to Guilherme Lima for teaching me how to work with the Tile conditions database, and to Yuri Smirnov for taking over that indescribably tedious task. Thanks go to past grad students, Rob Calkins, Chad Suhr, and especially Stephen Cole, for their help getting started on ATLAS in general and Tile in particular. They say the best way to learn is to teach, and there are certainly things that I learned by helping newer grad students, so I'd like to thank Puja Saha, Tyler Burch, Elliot Parish, Brianna Stamas, and Rafael Madriz, for just generally being around and asking questions.

I can't begin to express my appreciation for the rest of the $H^\pm \to \tau\nu$ analysis group. It's safe to say that the analysis, and therefore thesis, wouldn't have happened without you. Thanks go to Michael Pitt for organizing the analysis and providing the data driven jet $\to \tau$ fake modeling, including the Smirnov transformation of the Υ variable. Thanks also

TABLE OF CONTENTS

LIST OF TABLES

LIST OF FIGURES

LIST OF APPENDICES

PREFACE

Particle physics is the study of the most fundamental particles and forces known to modern science, including the search for deviations from our best current model at small distance and large energy scales. The Standard Model (SM) describes all the particles and forces directly observed today, with a few notable exceptions[1], but it has a number of other limitations. More concerning, it has difficulty accommodating the level of matter/anti-matter asymmetry in the observable universe, it doesn't predict that neutrinos have non-zero masses, and it has no candidate for Cold Dark Matter, which most simply explains a host of astrophysical observations. A number of Beyond Standard Model (BSM) theories have been introduced that can account for one or more of these phenomena, and generally introduce new particles as part of the theory. A common trend among many such BSM theories is an extended Higgs sector, which often includes electrically charged Higgs bosons.

This dissertation describes a search for charged Higgs bosons ($H^{\pm}$) produced in association with a top quark (t), where the former subsequently decays to a charged tau lepton ($\tau^{\pm}$) and tau-neutrino (ν_{τ} or anti-neutrino $\bar{\nu}_{\tau}$, respectively), and the latter decays to a semi-leptonic final state consisting of a jet initiated by a bottom quark (b) and a light charged lepton and neutrino pair ($\ell\nu_{\ell}$, where ℓ is an electron e or muon μ).

The thesis begins with a theoretical motivation for a search for $H^{\pm}$ bosons in the $\tau\nu$ channel. First, the SM is reviewed, including a description of the quarks and leptons that make up conventional matter, the gauge bosons that mediate interactions, and the SM Higgs sector and its role in electroweak symmetry breaking. Next, there is a brief introduction to

---

[1]These include gravity and dark energy.

Supersymmetry (SUSY) as a BSM theory that motivates a search for $H^{\pm}$, including a particular emphasis on the Minimal Supersymmetric Standard Model (MSSM)-like Higgs sector. Finally, the theory chapter concludes with a description of charged Higgs phenomenology, as motivation for searching in the $H^{\pm} \rightarrow \tau\nu$ channel.

The next section of the thesis describes the experimental apparatus used in this search. This section begins with a brief description of the Large Hadron Collider, currently the world's most energetic particle accelerator. The focus then switches to the ATLAS[2] experiment, the detector used to collect the data for this analysis. This includes a general description of each subdetector system and their roles in the detection of different types of particles.

The experimental apparatus section is followed by a description of object and event reconstruction. This includes a brief introduction to the ATLAS trigger system, which reduces the event rate to something which can reasonably be recorded for data analysis. This section then describes track and calorimeter cluster reconstruction, followed by a description of the high-level objects of interest in this analysis and their reconstruction from tracks, clusters, and other low-level objects. In particular, this covers electron and muon reconstruction and identification, jet reconstruction, and jet flavor tagging, including jets from hadronic tau decays, as well as missing transverse energy ($E_{\mathrm{T}}^{\mathrm{miss}}$) reconstruction.

The last major section of this thesis concerns the charged Higgs search itself. This includes object definitions and the selection applied to identify $H^{\pm}$ candidate events, along with the a short description of the physics data and simulations used for background estimates. A detailed description of the background modeling strategy is given, including simulated backgrounds for Standard Model processes with true hadronically decaying tau leptons, and events with $\ell \rightarrow \tau$ fakes. A data-driven background estimation is used for jet $\rightarrow \tau$ fakes, to

---

[2]A Toroidal Lhc ApparatuS

better model multi-jet / QCD-like events, which is shared with the complimentary search in a fully hadronic final state. The analysis strategy is then described, which consists primarily of a Multi-Variate Analysis (MVA) approach based on Boosted Decision Trees (BDTs). This includes a cross-check of each feature used in the MVA across several control and validation regions, along with validation of the resulting BDT scores in these regions. The systematic uncertainties considered in the analysis are then described. Finally, the results of the analysis are presented using a combined fit between the $\tau+e$ and $\tau+\mu$ final states[3], the complimentary $\tau+$ jets final state, and a dilepton control region used to constrain the dominant standard model background from top quark ($t\bar{t}$ and Wt) production.

My most direct contribution comes from acting as the primary analyzer for the semi-leptonic final state of the analysis, as well as development and maintenance of many tools used by both channels in the analysis. Of particular significance, this includes the design of the MVA approach and the first implementation of the MVA framework used by both channels of the analysis, the optimization, training, and evaluation of the BDT models used in the $\tau+\ell$ channel, and providing assistance in the adaptation of the tools and approach to the $\tau+$ jets channel.

During the course of my doctoral research, I also contributed to several areas of more general interest, most notably development and maintenance of software for the ATLAS tau working group, and serving as a Data Quality Coordinator for the ATLAS Tile Calorimeter. These are briefly described in the Appendices A and B, respectively. As part of my qualification task for authorship in the ATLAS collaboration, I also contributed to the Fast TracKer (FTK), including performance studies for the FTK Technical Design Report [1].

---

[3]Collectively labeled $\tau+\ell$.

CHAPTER 1

THEORY

This chapter describes the theory and motivation behind a search for $H^+ \rightarrow \tau^+ \nu_\tau$, or the charge conjugate process $H^- \rightarrow \tau^- \bar{\nu}_\tau$, collectively referred to as $H^\pm \rightarrow \tau\nu$ throughout the rest of the text. It begins with a short review of the SM particles and interactions. Next comes a brief overview of SUSY, particularly the MSSM, as it is a specific BSM theory that is both well known and requires the existence of $H^\pm$. The chapter concludes with a description of the Type II 2-Higgs Doublet Model (2HDM), such as is found in the MSSM, with its implications for the charged Higgs production cross section and branching ratio into SM particles, which motivates the choice of $H^\pm \rightarrow \tau\nu$ as a process of particular interest.

The Standard Model

The Standard Model is built around an $\mathrm{SU}(3)_C \times \mathrm{SU}(2)_L \times \mathrm{U}(1)_Y$ gauge group, where the $\mathrm{SU}(3)_C$ term governs the strong interaction [2, 3], and $\mathrm{SU}(2)_L \times \mathrm{U}(1)_Y$ describes the electroweak [4] portion of the theory. These interactions, or "forces", are mediated by fundamental particles called "bosons". Such forces are responsible for phenomena such as nuclear decay, the scattering that occurs when objects collide, and the tendency for the lightest fundamental particles to form stable bound states. Fundamental matter particles, or "fermions", are divided into quarks and leptons, where only quarks carry color charge and participate in strong interactions. All fermions participate in electroweak interactions, with the electromagnetic portion being limited to charged fermions (all quarks, and the lep-

tons that are not neutrinos). Fermions obey the Pauli Exclusion Principle: two fermions cannot share the same quantum state. As quantum state is often correlated with position, this causes fermions to occupy space[1], scatter off each other when colliding, and otherwise behave the way one expects from "matter".

A number of symmetries and corresponding conservation laws dictate the rates of interactions allowed the SM. CPT symmetry – that is, symmetry under simultaneous charge conjugation, mirror reflection, and time reversal – is assumed to be a good symmetry. CP can be violated in weak interactions, and implies a broken symmetry between the behaviors of matter and antimatter, but the symmetry holds under electromagnetic and strong interactions. Baryon number (equal to one third the number of quarks, minus one third the number of antiquarks) and lepton number are normally conserved in standard model interactions[2]. The number of particles of each lepton generation – but not each quark generation – is conserved under SM interactions[3]. Beyond that, electric and color charges are conserved, along with 4-momentum[4]. Also conserved is angular momentum, of which spin is typically the relevant form.

---

[1]Not in the sense that they have a volume, but that but that there's room for finitely many in any given bound state. For example, there is only room for 1 electron of each spin state per orbital around an atomic nucleus, and the energy level of each spin state correlates with the average distance from the nucleus, which itself governs the size of the atom.

[2]A non-perturbative chiral anomaly can result in "sphaleron" solutions to the electroweak field equations, permitting exchanges of 3 baryons for 3 anti-leptons or vice-versa, which can either explain or hinder baryogenesis and leptogenesis, depending on the order of the phase transition during electroweak symmetry breaking. Needless to say, this has not been observed, so for practical purposes we shall assume that baryon and lepton number are conserved independently.

[3]Ignoring neutrino oscillation.

[4]Energy and the familiar 3-momentum from Newtonian mechanics.

Particles

Particles in the SM can be broadly categorized as either fermions are bosons. Fermions have half-integer spin, and can be further categorized as either quarks or leptons. Bosons have integer spin, and are divided into gauge or vector bosons (with spin $s = 1$) and the scalar Higgs boson (spin $s = 0$) (Figure 1.1).

Fermions

Fermions carry half-integer spin ($\frac{1}{2}$, $\frac{3}{2}$, ...) and make up the matter part of the Standard Model. The Standard Model's fundamental fermions all carry a spin of $\frac{1}{2}$ and are divided into leptons and quarks.

Quarks come in three generations, each consisting of an $SU(2)_L$ doublet. Quarks interact through the electromagnetic, weak, and strong forces. The strong force couples to "color charge", denoted by R, G, and B, with anti-quarks carrying a conjugate charge $\bar{R}$, $\bar{G}$, or $\bar{B}$. Quarks interacting through the strong force form color-neutral bound states called hadrons, with either three different colored quarks (anti-quarks) for the fermionic baryons (anti-baryons), or as oppositely colored quark/anti-quark pairs forming bosonic bound states called mesons. The first generation of quarks is comprised of the up quark (u, charge $= +\frac{2}{3}$) and the down quark (d, charge $= -\frac{1}{3}$), with their anti-matter counterparts having opposite charge. The second generation of quarks contains a charm [6,7] and strange (c, s), and the third contains top and bottom (t, b), each with charges replicating the first generation, but having larger masses.

Leptons also come in three generations, each consisting of an $SU(2)_L$ doublet. Leptons are color-neutral, and therefore only interact through the electromagnetic and weak forces,
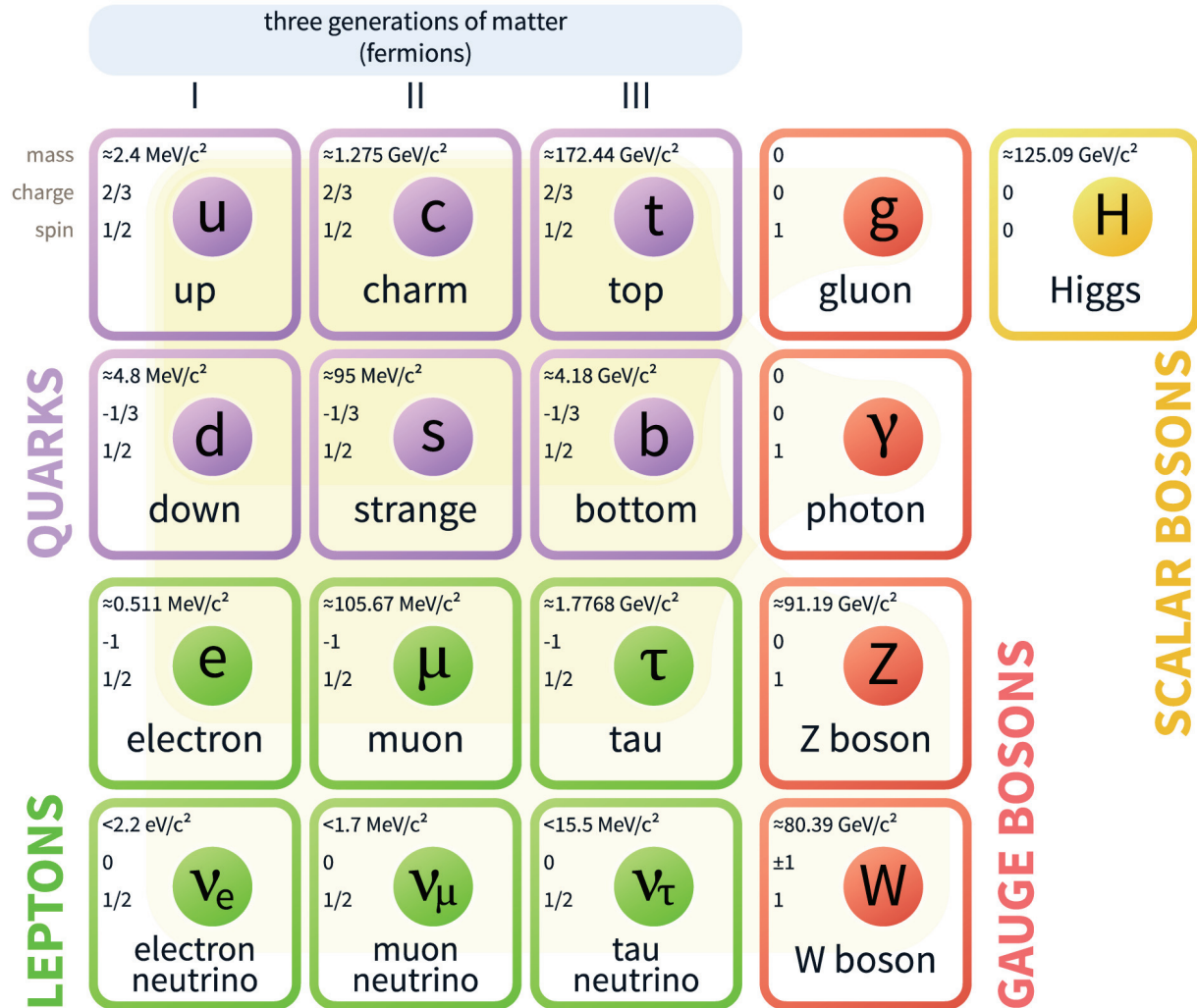
The 12 fundamental fermions and 5 fundamental bosons. Shaded loops indicate which bosons couple to which fermions. [5]

Figure 1.1: Standard model of elementary particles.

but not through the strong force. However, each generation of leptons contains one charged particle and one neutral particle, so only the charged particles may interact electromagnetically. The charged leptons (anti-leptons) are the electron (e), the muon (μ), and the tauon (τ), with a charge of -1 (+1). Neutrinos, the neutral leptons in each generation are, named after their corresponding charged partners (ν_e, ν_μ, ν_τ). As with the quarks, each generation's charged lepton is heavier than the last. In the standard model, no mechanism imparts mass to the neutrinos, but neutrino flavor oscillation experiments indicate that the mass difference between the neutrino flavors is non-zero, indicating that the neutrinos acquire a small amount of mass through some mechanism beyond the SM.

Bosons

Bosons carry integer spin (0, 1, 2, . . .) and may include composite and fundamental particles. Composite bosons are generally made up of fermions and vector bosons (e.g. the quark/gluon bound states forming mesons or even-numbered atomic nuclei), and are omitted from further discussion.

Tensor bosons, with spin 2, are not described by the Standard Model. If a graviton exists, then it is expected to be a massless[5] spin-2 boson, but it is difficult to comment on further without a theory of quantum gravity.

The vector bosons carry spin 1 and act as force carriers of the fundamental interactions in the Standard Model. Photons, which carry no color, electric charge, or weak isospin, mediate the electromagnetic force. Eight color-charged gluons mediate the strong force. Weak interactions (including decays or weak neutral currents) are mediated by the charged W^+ and W^- bosons and the neutral Z^0 boson. The W and Z [8, 9] bosons are conspicu-

---

[5]Inferred from the apparently infinite range of the gravitational force.

ously massive, due to the effects of spontaneous symmetry breaking [10, 11] via the Higgs mechanism [12–14], as described later.

Scalar bosons carry no spin, and thus far the only fundamental scalar boson observed is a SM-like Higgs boson H. The Higgs boson, and the Higgs mechanism's role in spontaneous symmetry breaking, is described further in its own section.

Interactions

The SM interactions are responsible for phenomena including the formation and transition between bound states[6], scattering, and the production and decay of fermions and bosons.

Electromagnetic Interaction

The familiar electromagnetic interaction arises from a broken $SU(2)_L \times U(1)_Y$ electroweak symmetry. This is described further in the section of the Higgs mechanism. The mediator of the electromagnetic force is the photon (γ), which couples to the (conserved) electric charge. As such, the quarks and charged leptons, as well as the charged $W^\pm$ bosons, can interact electromagnetically. The neutrinos, gluons, and the Z^0 and H bosons do not participate in electromagnetic interactions. Due to the massless nature of the photon, the electromagnetic force has an unlimited range.

---

[6]I.e. protons, atomic nuclei, atoms, and chemistry.

Weak Interaction

The weak interaction comes from the remainder of the broken $\mathrm{SU}(2)_L \times \mathrm{U}(1)_Y$ electroweak symmetry. As a consequence of the breaking of this symmetry, the $W^\pm$ and Z^0 bosons acquire relatively large masses, which causes the weak vector bosons to decay quickly, thus severely limiting the range of weak interactions. The $W^\pm$ bosons only couple to fermions with left chirality, or anti-fermions with right-handed chirality. Gluons and photons do not participate in the weak interaction. The CP symmetry is violated in weak interactions.

Strong Interaction

The strong interaction is driven by "color" charge. Color charged is so named because it obeys a $\mathrm{SU}(3)$ symmetry, which is isomorphic to the interaction between the primary colors of light. As such, color charges are denoted as Red (R), Green (G), or Blue (B), with their opposites given by a bar $(\bar{R}, \bar{G}, \bar{B})$[7]. As with light, each color is canceled by equal portions of the other two ($R + G + B$ is color neutral).

The driving force behind the strong interaction is that particles with color charge form color-neutral bound states called hadrons. Bound states between quarks (or anti-quarks) are held together with gluons, the boson which mediates strong interactions. The gluon is believed to be massless, like the photon, but as with the weak interaction the range of the strong force is limited. This is caused by the non-Abelian nature of the symmetry group, such that the gluons carry color charge and are likewise confined to bound states. If, for example, sufficient energy were added to a system to separate a quark or gluon from the

---

[7]To continue the analogy, these would correspond to the primary pigment colors: Cyan, Yellow, and Magenta.

rest of a hadron, then additional gluons and quark-antiquark pairs are produced, which form two color-neutral hadrons. Because of this, tightly clustered hadronic "jets" of particles are common in events where the strong interaction plays a role.

The Higgs Mechanism

Recall that the electroweak component of the SM gauge group is $SU(2)_L \times U(1)_Y$. The SU(2) component introduces weak isospin[8] T_1, T_2, T_3, and bosons W_1, W_2, and W_3. The $U(1)_Y$ portion introduces a weak hypercharge Y and a boson B^0. Now suppose there is a scalar field in the form of a SU(2) doublet with U(1) charge equal to 1. If this scalar field is given a non-zero vacuum expectation value, then its presence breaks the symmetry of $SU(2)_L \times U(1)_Y$. As the Higgs field is a complex doublet, this vacuum expectation value is defined by four components, such as $(t + iu, v + iw)$. With no loss of generality, the coordinate system may rotated such that the non-zero portion of the vacuum expectation value lies along only one component, such as $(0, v)$.

Now consider how this vector transforms in under SU(2). The possible transformations are given by the Pauli matrices σ_x, σ_y, and σ_z for rotations about the x, y, and z axes. A rotation about either the x or the y axis cause the two terms of the vector to mix, so it is apparent that the symmetry has been broken and that these two degrees of freedom have been lost. Rotation by an angle ϕ about the z-axis, corresponding to the generator T_3, gives $(0, ve^{-\frac{1}{2}i\phi})$. Meanwhile, a rotation in U(1) by $\frac{1}{2}\phi$ gives $(0, ve^{\frac{1}{2}i\phi})$. So one degree of symmetry can still be preserved if a rotation about the z-axis is combined with a rotation by half that amount in U(1).

---

[8]Named as such because it is isomorphic to spin, with values of $\pm\frac{1}{2}$ for the SM fermions and 0 or 1 for the SM bosons.

It therefore becomes convenient to define a generator for this transformation as $Q = T_3 + \frac{Y}{2}$. The conserved quantity which arises from this symmetry is *electric charge*.

After symmetry breaking, the $W^{\pm}$ bosons emerge from a mixing between the W_1 and W_2 with two degrees of freedom from the Higgs potential. The Z arises from the mixing of W_3 and B^0 with the third lost degree of freedom in the Higgs potential. The remaining mixture of W_3 and B^0 does not mix with the Higgs, and forms the photon. The one degree of freedom from the Higgs potential that was not lost during symmetry breaking gives rise to H, the sole physical Higgs boson of the Standard Model.

Supersymmetry

Despite the Standard Model's success at describing the known particles and interactions, it has a number of shortcomings. The SM has difficulty accommodating the degree of matter-antimatter asymmetry observed in the universe, it includes no cold dark matter candidate, and it offers no description of quantum gravity, to name a few.

There is also the issue of the "hierarchy problem", which may be exacerbated by new physics unless the new physics conspires with the SM to resolve the issue. While the observed mass of the Higgs boson is close to the electroweak scale, particles introduced by new physics apply corrections to the mass of the Higgs proportional to the (much higher) energy scale of the new physics.

Evidently, whatever new physics remains to be discovered, the net effect must be that the corrections applied to the Higgs mass happen to almost perfectly cancel out, and this leaves behind a Higgs boson with a mass near the electroweak scale. While it is technically possible that unrelated corrections could happen to cancel each-other in aggregate, this requires a high degree of fine tuning.

Corrections to the Higgs mass from fermions and bosons enter with a relative minus sign. If a symmetry between fermions and bosons is introduced, then the corrections from new physics may cancel without significant fine tuning. This symmetry between fermions and bosons is what we call Supersymmetry (SUSY).

There is a range of models built around SUSY. The Minimal Supersymmetric Standard Model [15] (MSSM) is the smallest extension to the SM needed to introduce SUSY, and is the obvious target for physics searches. The remainder of this section considers the MSSM, and primarily summarizes introductory material from [16].

MSSM Particles

In SUSY, each SM particle appears in a supermultiplet with its supersymmetric partners. The particles in a supermultiplet contain the same quantum numbers except for spin, and in an unbroken supersymmetry they have equal masses. As the supersymmetric parters (sparticles) haven't been discovered yet, supersymmetry must be a broken symmetry, which gives masses to the sparticles on the order of TeV[9] or more.

The SM gauge bosons are members of gauge supermultiplets, each of which contains one spin-1 gauge boson and one spin-$\frac{1}{2}$ fermion called a gaugino. The left and right handed helicity states of the guagino transform symmetrically under the gauge group transformations, so the gaugino does not participate in weak interactions, and therefore it cannot be associated with a standard model fermion.

The superpartners of the gluons (g) are called gluinos ($\tilde{g}$), which are Majorana fermions carrying the same color charges as the gluons. The superpartners of the $SU(2)_L \times U(1)_Y$

---

[9]Tera (trillion) electron-volts. In particle physics, mass an energy are often exchanged via the $E = mc^2$ relationship, so it becomes convenient to quote masses in terms of eV/c^2 or eV.

electroweak fields are the winos ($\tilde{W}^{\pm}$ and $\tilde{W}^0$) and the bino ($\tilde{B}^0$). Electroweak symmetry breaking causes the neutral wino and bino to mix and form the zino and photino.

A chiral supermultiplet contains a spin-$\frac{1}{2}$ fermion and two spin-0 bosons. Recall that the electroweak interaction requires left handed fermions to transform differently under the gauge group. This property is satisfied only by chiral supermultiplets, so the SM fermions must be members of chiral supermultiplets. The superpartners of the SM quarks and leptons are called squarks and sleptons. Each squark or slepton is the superpartner of either the left handed or right handed helicity state of an SM quark or lepton, so e.g. a squark of flavor $q = u, d, c, s, t, b$ is denoted $\tilde{q}_L$ or $\tilde{q}_R$ based on the handedness of its superpartner. As the SM only includes left-handed neutrinos[10], the sneutrino is only subscripted by lepton flavor: $\tilde{\nu}_e$, $\tilde{\nu}_\mu$, $\tilde{\nu}_\tau$.

A chiral supermultiplet is also required for the Higgs boson. As discussed in a later section, the MSSM requires the introduction of a second Higgs doublet. The superpartners of the Higgs bosons are called Higgsinos. Through electroweak symmetry breaking, these mix (together with the zino and the photino) to form the charginos ($\tilde{\chi}_1^{\pm}$, $\tilde{\chi}_2^{\pm}$) and the neutralinos ($\tilde{N}_i^0$ for $i=1\ldots4$, ordered lightest to heaviest, or sometimes $\tilde{\chi}_i^0$).

R-Parity

While not crucial to this analysis, it's important to note that, other than spin, the supersymmetric parters carry the same quantum numbers as their SM partners. In particular, they can carry baryon and lepton number, so a naive MSSM may not conserve these quantities.

Since experimental results are consistent with baryon and lepton numbers being conserved, this must be accounted for by some mechanism in the theory. A simple approach is

---

[10]Which is technically incorrect, given their non-zero masses, but close enough for most purposes.

to introduce a new R-parity $P_R = (-1)^{3B+L+2s}$, where B and L denote baryon and lepton numbers, and s is spin. Under this definition, the SM particles all have an R-parity $P_R = +1$, while their supersymmetric partners have $P_R = -1$.

Conservation of R-parity leads to a number of restrictions on the production and decay modes available to supersymmetric particles. One particularly notable consequence is that the lightest supersymmetric particle (LSP) must be stable. An electrically neutral colorless LSP[11] could be a strong candidate for cold dark matter.

The MSSM Higgs Sector

Suppose that there was only the SM Higgs field. In a supersymmetric theory, this places the Higgs boson within a chiral supermultiplet, where its superpartner, a higgsino, is an isodoublet with weak hypercharge $\pm\frac{1}{2}$. With only a single Higgs chiral supermultiplet, this higgsino causes a gauge anomaly, which can be cancelled by introducing two doublets with $Y = \frac{1}{2}$ and $Y = -\frac{1}{2}$. Furthermore, the structure of the MSSM superpotential requires two doublets, one of which gives masses to the up-type quarks, and another to the down-type quarks and charged leptons. In the taxonomy of BSM theories, this is known as a Type II Two-Higgs Doublet Model (2HDM).

Therefore, in an MSSM-like 2HDM, the Higgs sector is described by two complex-valued Higgs doublets, with a total of eight degrees of freedom. One of the doublets couples to the up type quarks, and the other doublet couples to the down-type quarks and charged leptons. As in the SM, three degrees of freedom are lost through spontaneous symmetry breaking, which gives mass to the W^+, W^-, and Z bosons, and the remaining degrees of freedom manifest as physical bosons. These bosons are a light neutral scalar h^0, a heavy

---

[11]I.e. the lightest neutralino $\tilde{N}_1^0$.

neutral scalar H^0, a neutral pseudoscalar A^0, and two charged scalar H^+ and H^- bosons. The free parameters of the Higgs sector are then the masses of the bosons and the ratio of the vacuum expectation value of the second doublet to the first, denoted by $\tan\beta$. In this model, the light neutral scalar h^0 is the prime candidate for the SM-like neutral scalar boson at 125 GeV discovered at the LHC by the ATLAS and CMS experiments in 2012 [17, 18]. The remaining masses and the $\tan\beta$ parameter must be constrained experimentally, though very small values of $\tan\beta$ are disfavored, since they cause top quark Yukawa couplings to become non-purturbative.

Charged Higgs Bosons

Because the Higgs field couplings to the fermions are proportional to the fermion masses[12], the leading order $H^\pm$ production diagrams at the LHC are expected to be via a vertex with a top and bottom quark or anti-quark (Figure 1.2). These modes resemble either $t\bar{t}$ or Wt production in the SM, but with a $W^\pm$ replaced by $H^\pm$, and as such have an associated top in the final state. The $H^\pm$ production cross section is expected to decrease rapidly with increasing $m_{H^\pm}$, as shown in Figure 1.3, based on the collision energy in the center-of-mass frame and the fermionic couplings of $H^\pm$.

The branching fractions of the charged Higgs depend on $\tan\beta$ due to its fermion-mass-dependent coupling to either up-type quarks or down-type quarks and charged leptons, and on $m_{H^\pm}$ due to phase space constraints. The predicted branching fractions in several MSSM benchmark scenarios are shown in Figure 1.4. Generally speaking, $H^\pm \to \tau\nu$ is the only decay mode with a significant branching fraction at low mass ($m_{H^\pm} < m_t$), due to phase space constraints. At higher masses, if $\tan\beta$ is not very large, then bosonic decay modes

---

[12]Excluding the neutrinos, which must acquire mass through another mechanism.
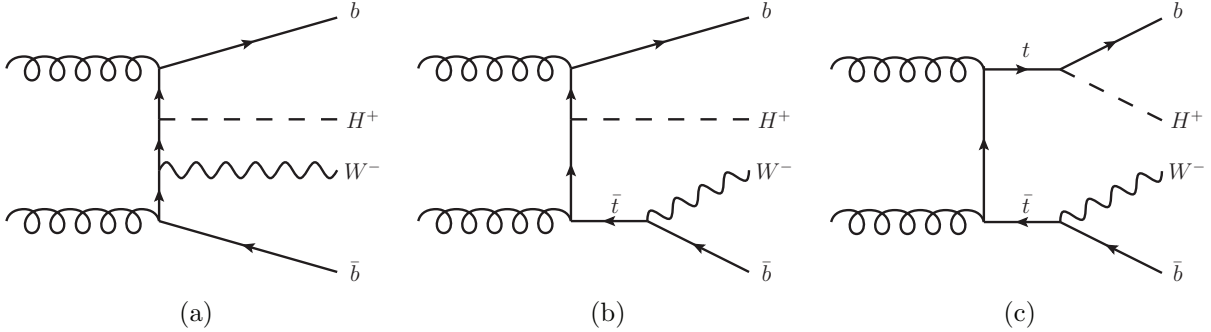
(a) non-resonant top-quark contribution, (b) single-resonant top-quark contribution that domi-
nates at large $H^\pm$ masses, and (c) double-resonant top-quark contribution that dominates at low
$H^\pm$ masses. The interference between these three main diagrams becomes most relevant in the
intermediate-mass region. [19]

Figure 1.2: Example of leading-order Feynman diagrams contributing to the production of
charged Higgs bosons in pp collisions.

may dominate. For high values of $\tan\beta$ and masses above approximately m_t, the largest

branching fraction goes to $H^\pm \to tb$, with $H^\pm \to \tau\nu$ at the second place retaining a sizeable

branching fraction.

The associated top quark may decay either hadronically or semi-leptonically. As such,

the $H^\pm \to \tau\nu$ analysis is split into $\tau + \text{jets}$ and $\tau + \ell$ final states, with this thesis focused on

the latter.

Prior Results

It is important to note, for context, that searches for $H^\pm \to \tau\nu$ have been performed in

the past. Prior results were taken into account when deciding on a strategy for this analysis,

so it may be useful to review these results.
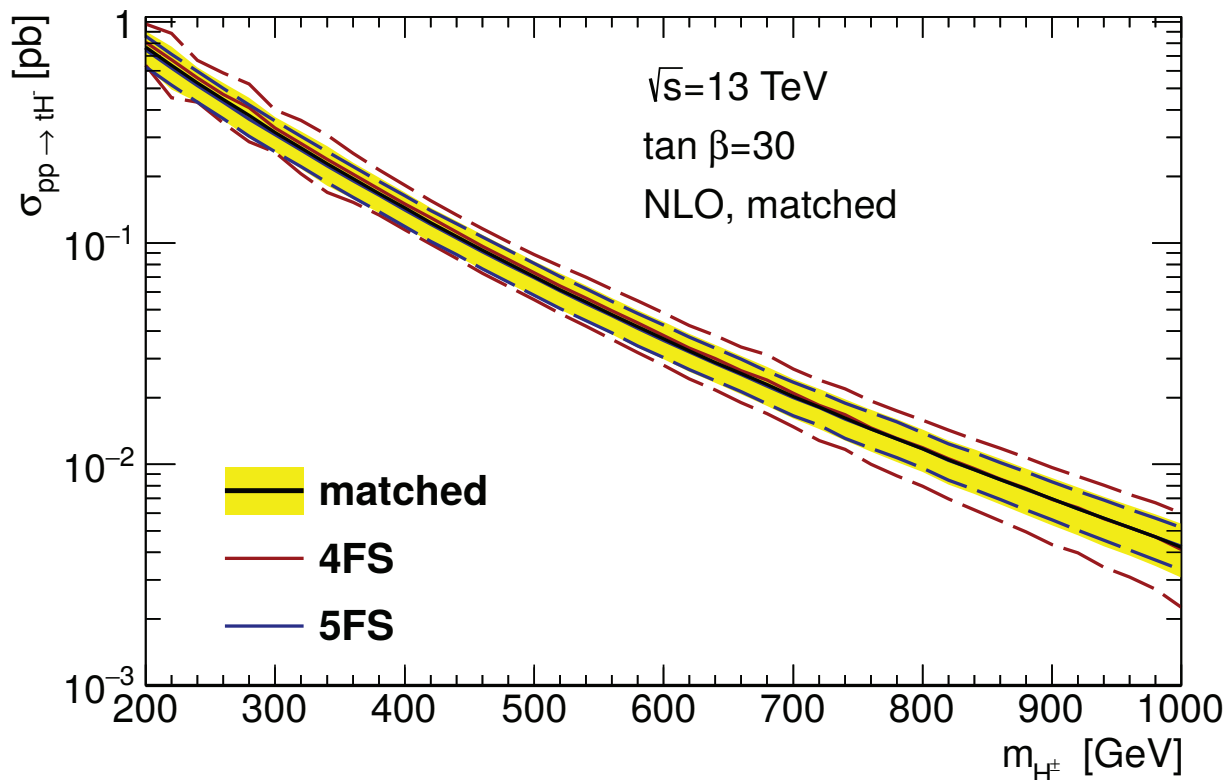
Shown as a function of $m_{H^\pm}$ [20]. σ is the cross-section (proportional the probability of production) and $\sqrt{s}$ is the collision energy in the center-of-momentum frame. 4FS denotes a 4-flavor-scheme parton distribution function, in which the b-quark flavor content of the proton is negligible. 5FS is a 5-flavor-scheme, in which the b-quark flavor content of the proton is significant.

Figure 1.3: Predicted $\sigma(pp \rightarrow H^\pm + X)$ at $\sqrt{s} = 13$ TeV for $\tan\beta = 30$.
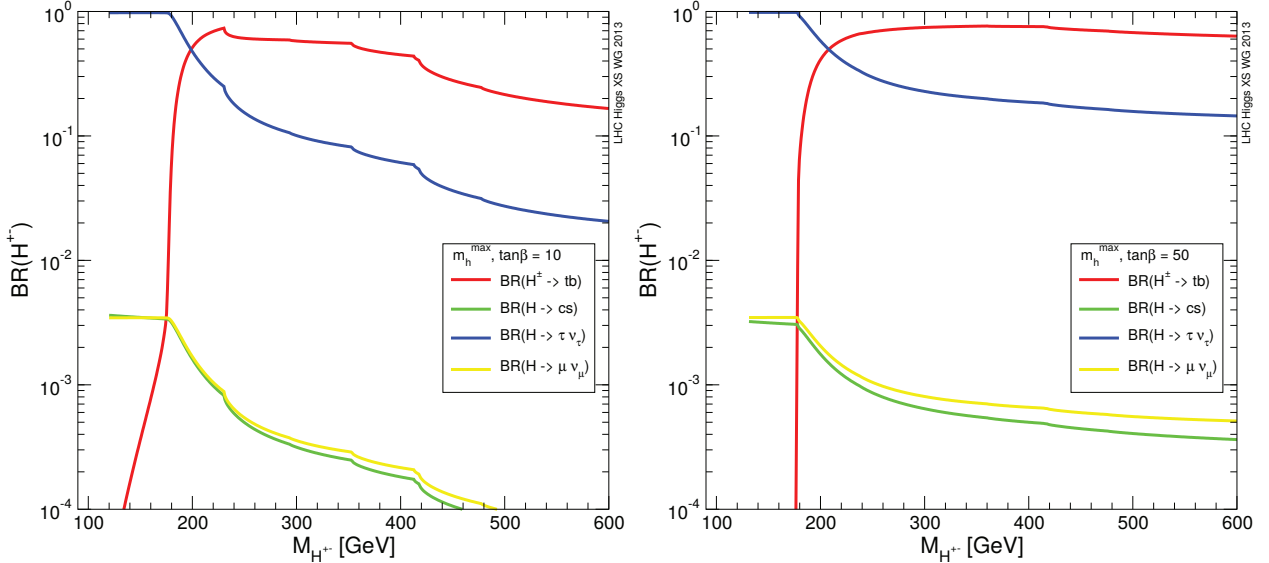
Shown as a function of $m_{H^\pm}$ at $\tan\beta = 10$ (left) and $\tan\beta = 50$ (right) [21] in the $m_h^{\max}$ MSSM benchmark scenario [22]. The $m_h^{\max}$ scenario seeks to maximize the value of m_h for a given $\tan\beta$ hypothesis (for fixed values of other parameters).

Figure 1.4: $H^\pm$ branching fractions.

ATLAS released a conference note for ICHEP[13] 2016 [23], superseding the results from an earlier paper [24], with both instances focusing on the τ+jets final state and $m_{H^\pm} \geq 200$ GeV. The high-mas ATLAS results correspond to a production cross section times branching fraction $\sigma(pp \to H^\pm) \times \mathrm{BR}(H^+ \to \tau\nu)$ in a range of 2.0 to 0.008 pb[14] for masses between 200 and 2000 GeV. For $m_{H^\pm} \leq 160$ GeV, the most recent ATLAS result [25] was from Run 1 at $\sqrt{s} = 8$ TeV (Figure 1.5), corresponding to a branching fraction $\mathrm{B}(t \to bH^+) \times \mathrm{BR}(H^+ \to \tau\nu)$ between 0.23% and 1.3% for $H^\pm$ in the mass range from 80 to 160 GeV. The CMS experiment's latest result [26] considers $m_{H^\pm} \geq 180$ GeV and $m_{H^\pm} \leq 160$ GeV (Figure 1.6).

[13]International Conference on High-Energy Physics

[14]Pico-barn. One "barn" is 100 fm^2, or approximately the cross-sectional area of a uranium nucleus.

In all cases, these results consider only the $\tau + \text{jets}$ final state, and do not consider charged Higgs masses near the top quark mass (from about 160 to 180 GeV).
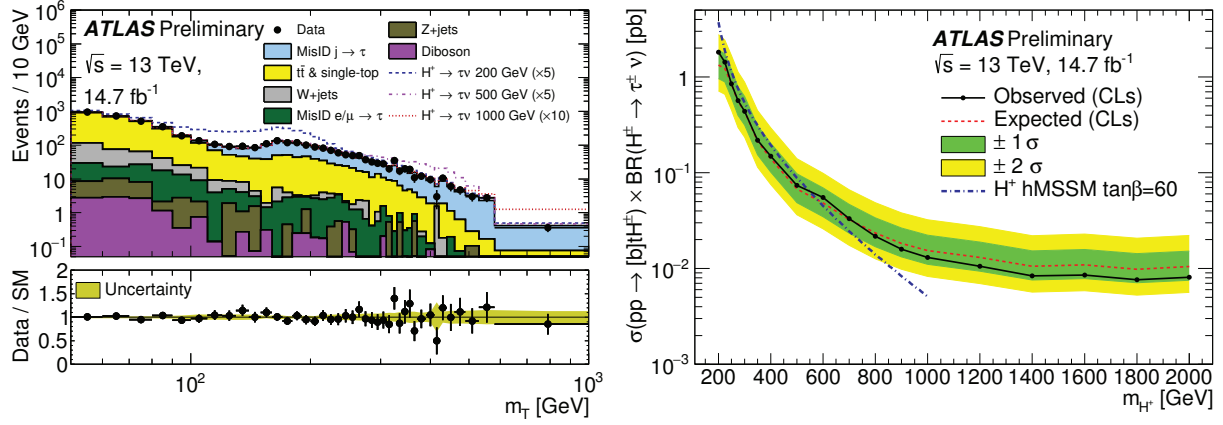
(a) Discriminant Variable, high-mass

(b) Observed Limits, high-mass
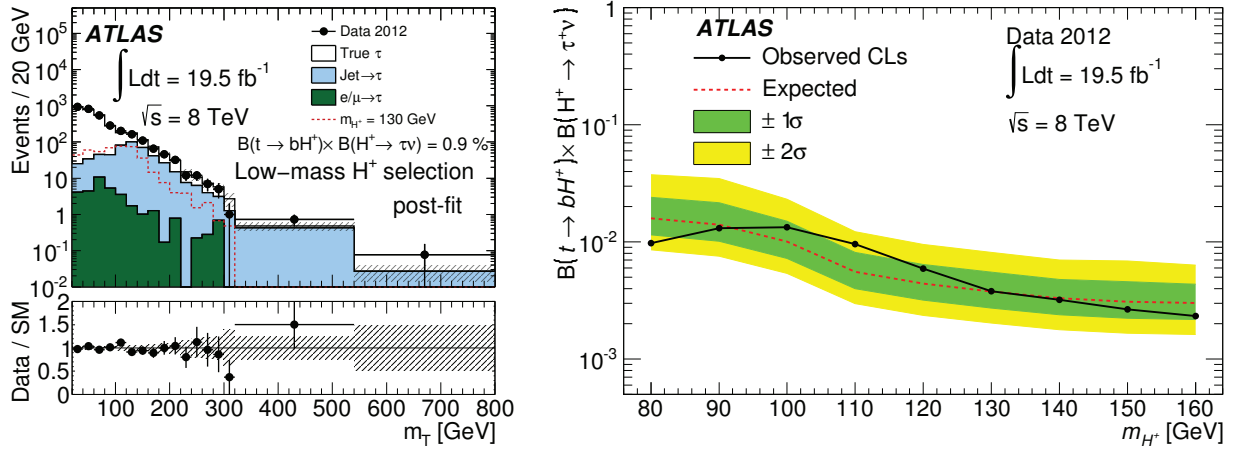
(c) Discriminant Variable, low-mass

(d) Observed Limits, low-mass

Figure 1.5: Discriminant variable and observed limits from prior ATLAS searches for $H^{\pm} \to \tau\nu$.
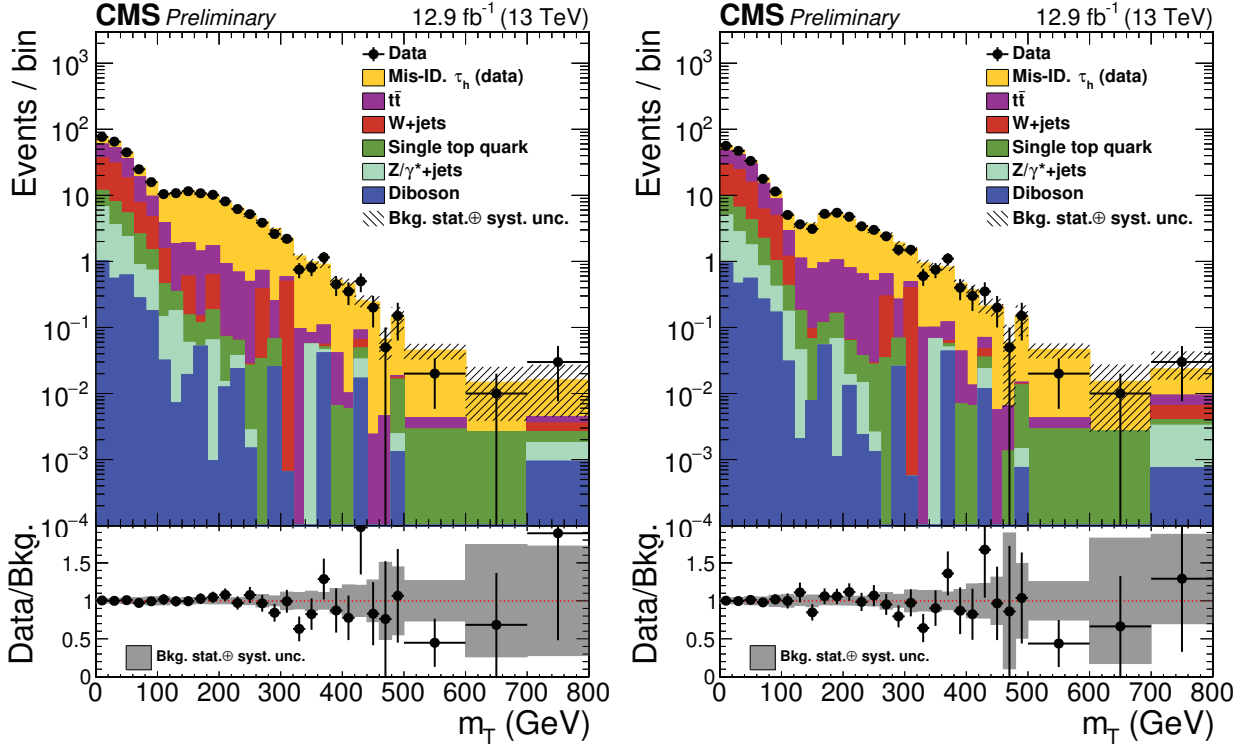
(a) Discriminant Variable, low-mass selection
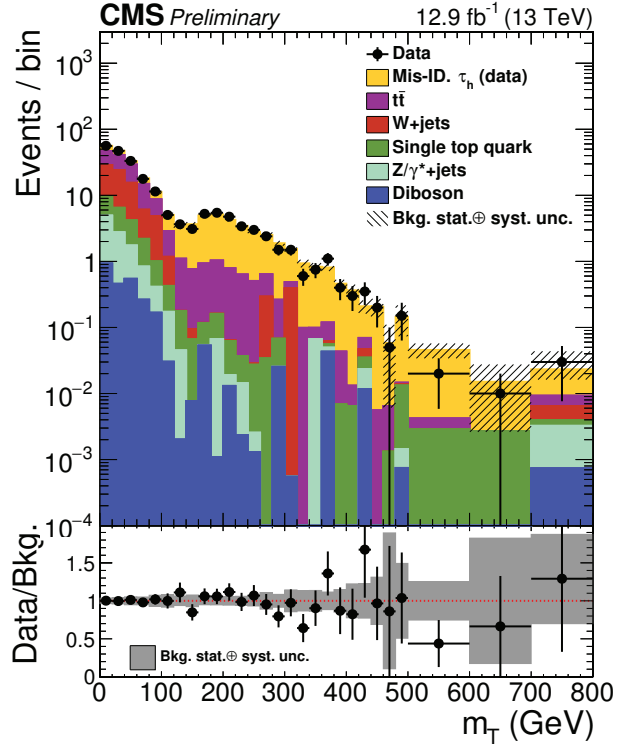
(b) Discriminant Variable, high-mass selection
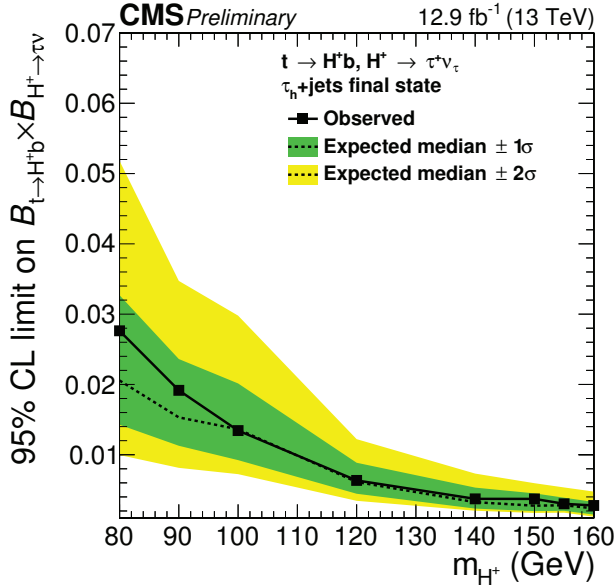
(c) Limits, low-mass
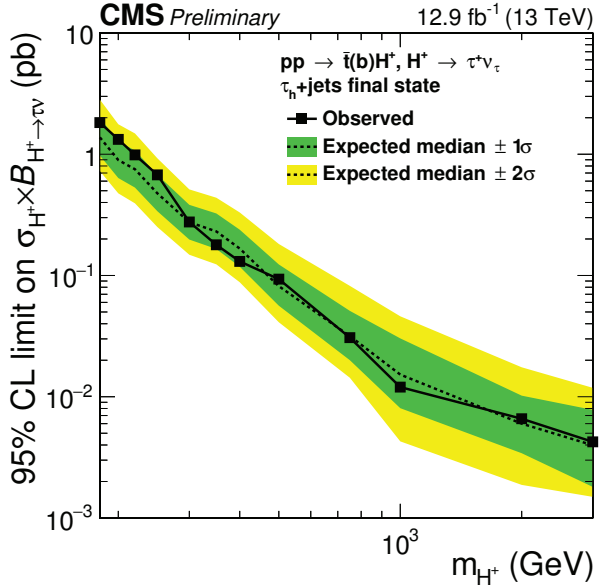
(d) Limits, high-mass

Figure 1.6: Discriminant variable and observed limits from prior CMS searches for $H^{\pm} \rightarrow \tau\nu$.

CHAPTER 2

EXPERIMENTAL APPARATUS

LHC

The Large Hadron Collider (LHC) is a particle accelerator operating at CERN, spanning the Franco-Swiss border, with headquarters just outside Meyrin in the canton of Geneva, Switzerland. Built in an existing tunnel from the LEP experiment [27], the LHC is a hadron collider capable of proton-proton, proton-lead, or lead-lead collisions. Designed for a proton-proton collision center of mass energy $\sqrt{s} = 14$ TeV, the LHC operated at $\sqrt{s} = 7$ TeV or 8 TeV during the Run 1 period, from late 2009 to early 2012, and has operated at $\sqrt{s} = 13$ TeV since LHC Run 2 began in 2015. The LHC's design luminosity is 10^{34} cm^{-2}s^{-1}, with a record peak luminosity of 2.06×10^{34} cm^{-2}s^{-1} as of the end of 2017, reaching up to approximately 60 interactions per bunch crossing [28].

The main ring of the LHC has a circumference of 27 km and is located in a tunnel $50 - 175$ m under ground. Radiofrequency (RF) cavities are used to accelerate particles in the LHC. An RF cavity provides an oscillating electromagnetic field to accelerate particles and sort them into bunches, based on the relative timing of the particle and the phase of the wave as the particle passes through the RF cavity, while magnet systems bend and focus the beam of particles as they travel about the LHC main ring and are steered to collide at the center of the LHC detectors [29]. Four main detectors sit around the LHC ring: ALICE, ATLAS, CMS, and LHCb. ATLAS and CMS are general purpose detectors designed to perform precision measurements of known physics processes and search for a broad range of

new physics. ALICE is designed for heavy-ion physics, while LHCb is optimized for precision b-quark physics.

ATLAS

ATLAS (A Toroidal LHC ApparatuS) [30] is one of the four main experiments at the LHC. As a general purpose detector, ATLAS was designed to search for, and make precision measurements of, a wide range of physics processes. Most notably, this includes a SM-like Higgs boson, the discovery of which was announced jointly with the CMS collaboration in July 2012.

The overall composition of ATLAS is similar to that of other general purpose particle detectors. It is cylindrical in shape, with collisions taking place near the center of the detector. As particles produced in the collision, or their decay products, travel away from the interaction point, they pass through a number of subdetector systems shown in Figure 2.1. Each subdetector interacts with certain classes of particles and measures some of their properties, as shown in Figure 2.2. Roughly speaking, the subdetectors can be grouped into the Inner Detector (ID), the calorimeters, and the muon system.

ATLAS uses a right-handed coordinate system defining the positive x-axis to point towards the center of the LHC, and the y-axis points up. The z-axis is tangent to the counterclockwise direction when the LHC is viewed from above, and corresponds to the axis of the cylindrical ATLAS detector. The angle about the z-axis is denoted by ϕ, while the angle with respect to the positive z-axis is denoted by θ. Pseudorapidity $\eta \equiv -\ln(\tan\frac{\theta}{2})$ is generally used instead of θ, as angular distances between objects in η are invariant under Lorentz boosts along the z-axis.
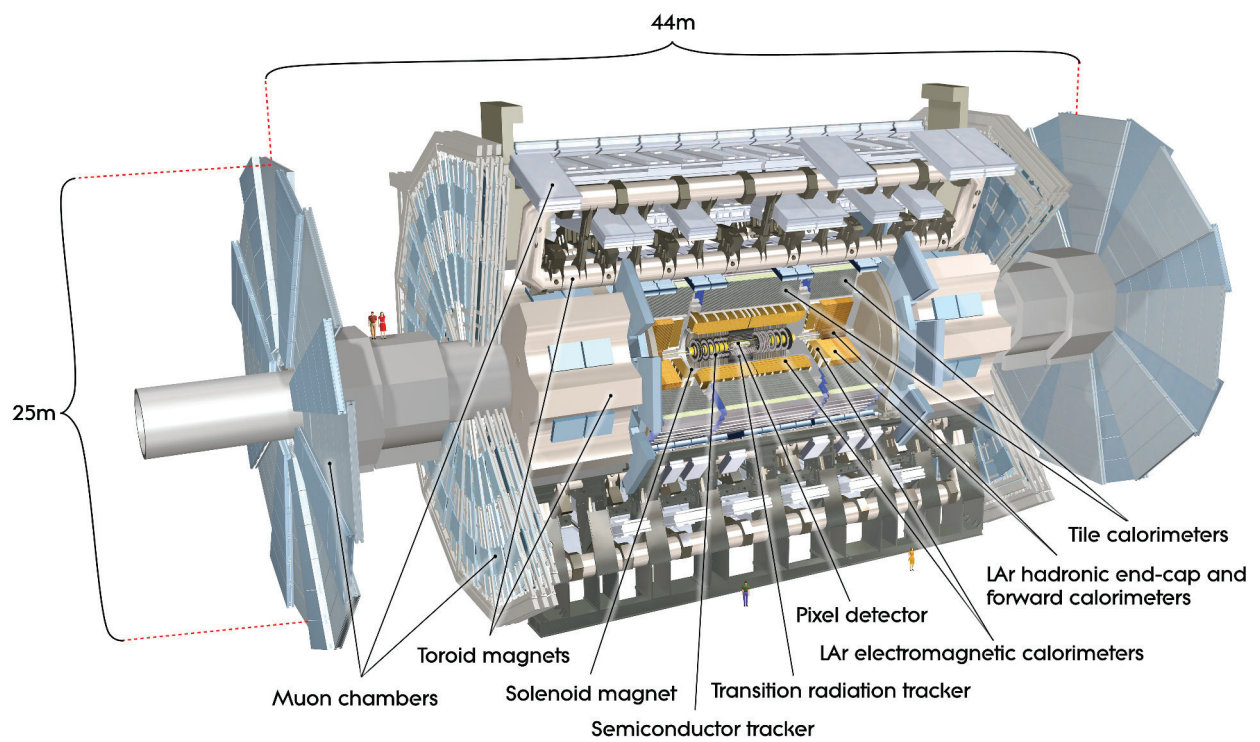
The dimensions of the detector are 25 m in height and 44 m in length. The overall weight of the detector is approximately 7000 tonnes. [30, 31]

Figure 2.1: Cut-away view of the ATLAS detector.
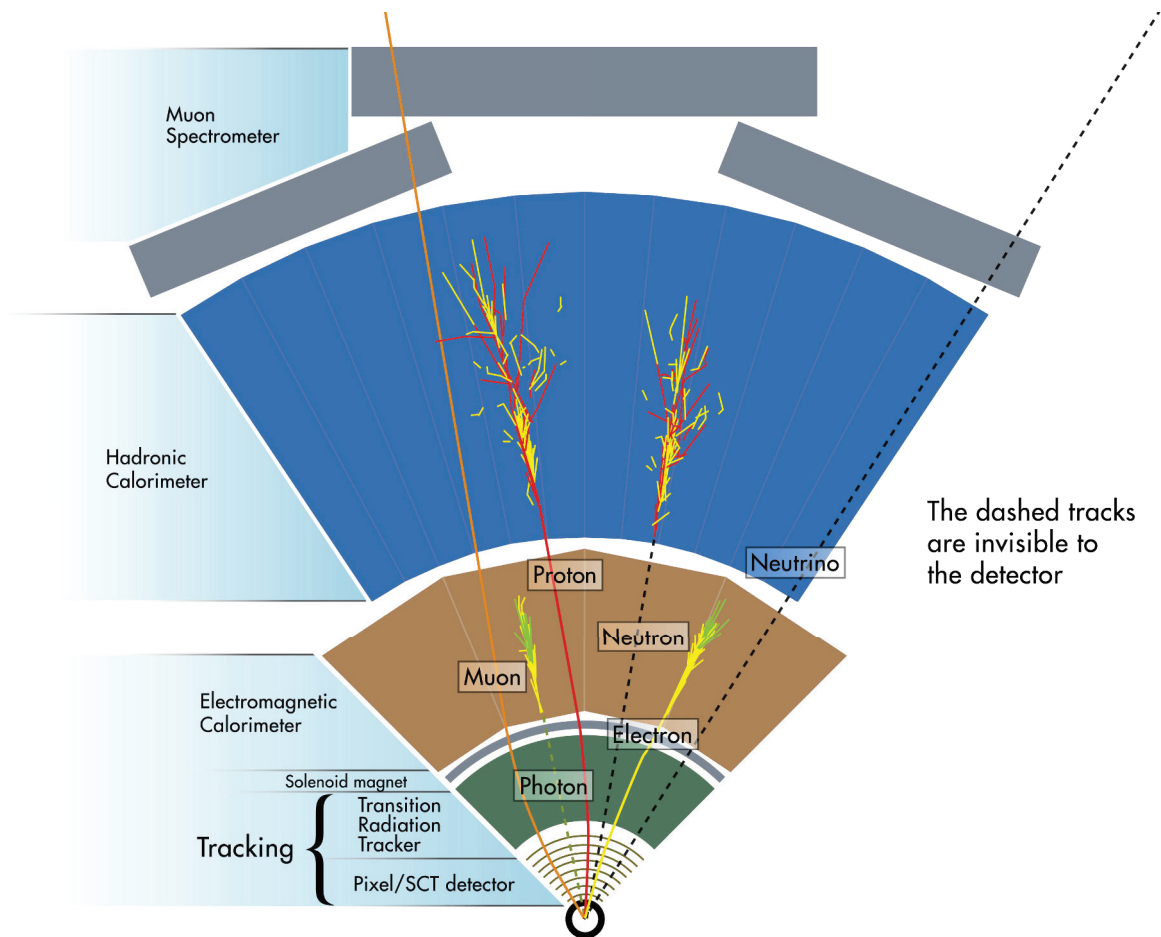
The detector has azimuthal symmetry about the z-axis and is reflectively symmetric about the $z = 0$ plane.

Figure 2.2: The role of each subdetector system in particle detection [32].

The following sections describe the ATLAS subdetectors which comprise the Inner Detector, the Liquid Argon and Tile Calorimeters, and the Muon Spectrometer, as well as the magnets used by the ID and Muon systems. Several smaller detectors sit in the extreme forward region. These include Luminosity measuring Using Cherenkov Integrating Detector (LUCID) , Absolute Luminosity For ATLAS (ALFA), and the ATLAS Zero Degree Calorimeter (ZDC). LUCID and ALFA perform luminosity measurements, and ZDC is used in heavy-ion collisions.

Inner Detector

The ATLAS Inner Detector [33], shown in Figure 2.3, consists of the pixel, silicon microstrip tracker (SCT), and transition radiation tracker (TRT) subdetectors. These subdetector systems work together to provide precision tracking of electrically charged particles over the $|\eta| < 2.5$ range. Precise and accurate tracking is crucial for primary vertex identification, object reconstruction and identification, and to suppress objects from unrelated events caused by multiple interactions per bunch crossing or noisy beam conditions (pileup).

Pixel

The Pixel detector is the first active detector region encountered by particles produced in a collision, as they travel outward from in the direction transverse to the beam line. The Pixel detector is organized into barrel and end-cap regions, with three[1] layers of silicon pixel modules in 112 barrel staves, and a total of 48 end-cap sectors organized into three layers

---

[1]Not counting the IBL.

6.2m

2.1m

Barrel semiconductor tracker

Pixel detectors

Barrel transition radiation tracker

End-cap transition radiation tracker

End-cap semiconductor tracker
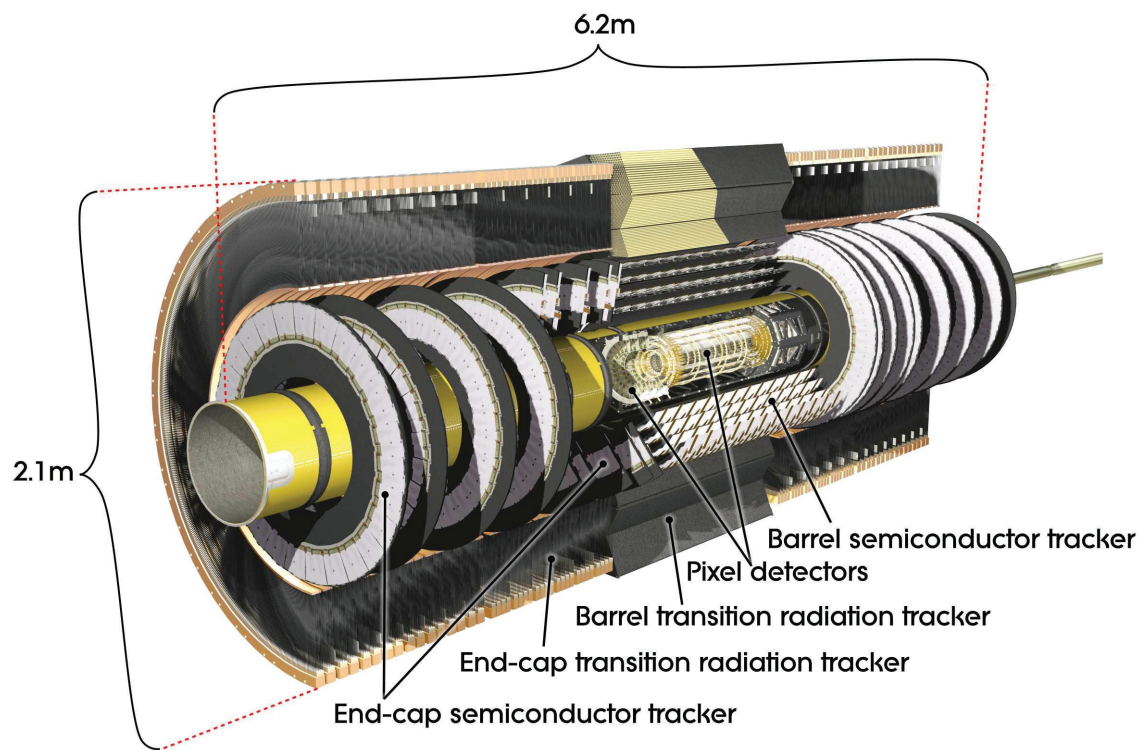
Figure 2.3: Cut-away view of the ATLAS Inner Detector [30].

of eight sectors in each pixel end-cap. This covers a pseudorapidity range of $|\eta| < 2.5$. The Insertable B Layer (IBL) [34], the innermost layer of the ATLAS detector, was installed in 2014 to cope with the increased demand of Run 2 data taking conditions and test technology planned for future ATLAS upgrades.

SCT

The Semiconductor Tracker (SCT) sits outside the pixel detector and consists of four barrel and nine end-cap layers. Each layer is made from two parallel silicon microstrip layers, the strips on each perpendicular to those on the other, and extending to a maximum pseudorapidity of $|\eta| = 2.5$. This approach reduces the complexity and the required number of readout channels, when compared with the Pixel detector, but leads to reduced hit resolution and higher occupancy. As such, it is better suited to tracking particles as they pass further from the beam line, where this causes less of an effect on angular resolution.

TRT

The Transition Radiation Tracker (TRT) sits outside the SCT, with respect to the beam line, and makes up the outermost tracking component of the ID. The TRT consists of interleaved straw tubes and radiator material surrounded by a (typically Xenon-based) gas mixture, with a total of 73 straw planes in the barrel region and 160 in the end-caps. The straw tube drift chambers contain gold-plated tungsten wires, and use drift time to measure radial coordinates from about 36 hits per track, but the TRT lacks the Pixel and SCT's ability to precisely measure track coordinates in z. Charged particles can emit X-ray transition radiation when passing through the surface of the radiator material, with an intensity that

scales as a function of the particle's relativistic Lorentz factor ($\gamma = (1 - v^2/c^2)^{-1/2}$), which is used for electron identification. As such, the TRT plays a direct role not only in tracking, but also in particle identification.

Calorimeters

Calorimeters Figure 2.4 measure the energy of particles absorbed by the calorimeter's active material. In particular, this includes electrons and photons in the electromagnetic calorimeters, and hadrons in the hadronic calorimeters. The ATLAS liquid argon (LAr) calorimeter [35] provides electromagnetic calorimetry over the full η (up to $|\eta| < 3.2$), and hadronic calorimetry in the forward and end-cap regions ($1.5 < |\eta| < 4.9$). The tile calorimeter (TileCal) [36] is the hadronic calorimeter in the barrel and extended barrel regions of the detector ($|\eta| < 1.7$), as well as the gap/crack regions between the LAr barrel and end caps, and includes minimum bias trigger scintillator in the forward regions.

LAr

The Liquid Argon calorimeter is a sampling calorimeter segmented into up to 4 layers by depth, with Liquid Argon as the active material, and either lead, copper, or a tungsten/copper alloy as passive material in the electromagnetic barrel (EMB) and endcap (EMEC), the hadronic endcap (HEC), and forward calorimeter (FCal) regions, respectively. Liquid Argon is ionized by high-energy charged particles or photons, and the freed electrons drift to copper readout electrodes. The LAr EMB covers $|\eta| < 1.5$, the EMEC+HEC cover $1.4 < |\eta| < 3.2$, and the FCal covers the $3.1 < |\eta| < 4.9$ region with a depth of about 10 interaction lengths (λ). In total, LAr has approximately 180,000 readout channels.

Tile barrel

Tile extended barrel

LAr hadronic
end-cap (HEC)

LAr electromagnetic
end-cap (EMEC)

LAr electromagnetic
barrel

LAr forward (FCal)
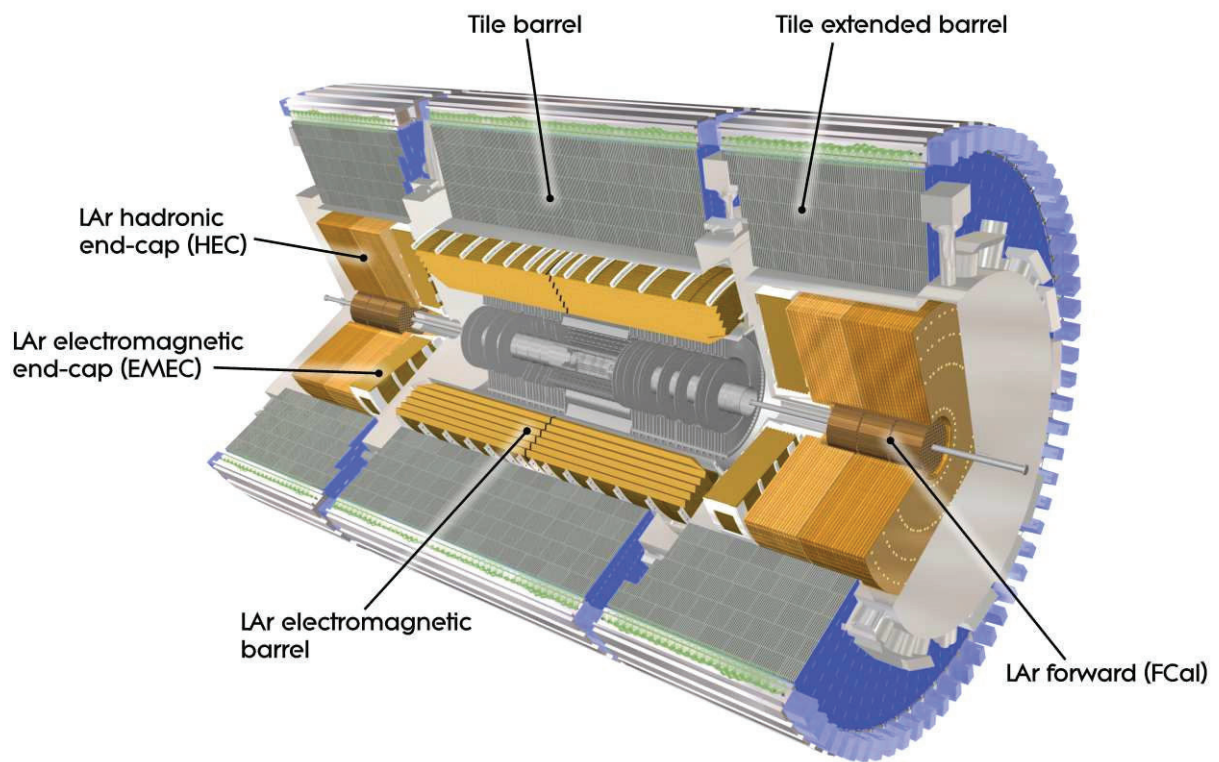
Figure 2.4: Cut-away view of the ATLAS calorimeter system [30].

Tile

The Tile Calorimeter envelopes the LAr calorimeter in the $|\eta| < 1.7$ region, including cells in the crack region between the Tile long barrel and extended barrel, and the LAr EMB and HEC sections. The Minimum Bias Trigger Scintillator (MBTS), used by the trigger system in low-luminosity runs, covers the $2.1 < |\eta| < 3.9$ region. TileCal uses plastic tiles with scintillating dye and alternated with steel absorber plates. Hadrons passing through the tiles and absorbers begin to shower, with most of the energy being deposited in the absorber plates. Some fraction of energy is converted to scintillation photons as the particles pass through the tiles. The light is carried by fibers to one of approximately 10,000 photomultiplier tubes (PMTs), where it is converted to an electrical signal and amplified for the readout system. Muons that pass through the TileCal leave a measurable signature, but are not stopped by the absorber plates. TileCal is segmented into 3 layers with thicknesses of about 1.5, 4.1, and 1.8 λ in the barrel region, and 1.5, 2.6, and 3.3 λ in the extended barrel [30].

Muon Chambers

Muons typically pass through the detector without being stopped. The muon chambers [37], shown in Figure 2.5, make up the outermost subdetector systems, which are in effect an outer layer of tracking subsystems, and cover up to $|\eta| < 2.7$. Tracks left in the muon chambers can be extrapolated and matched to tracks in the ID for muon reconstruction and identification.
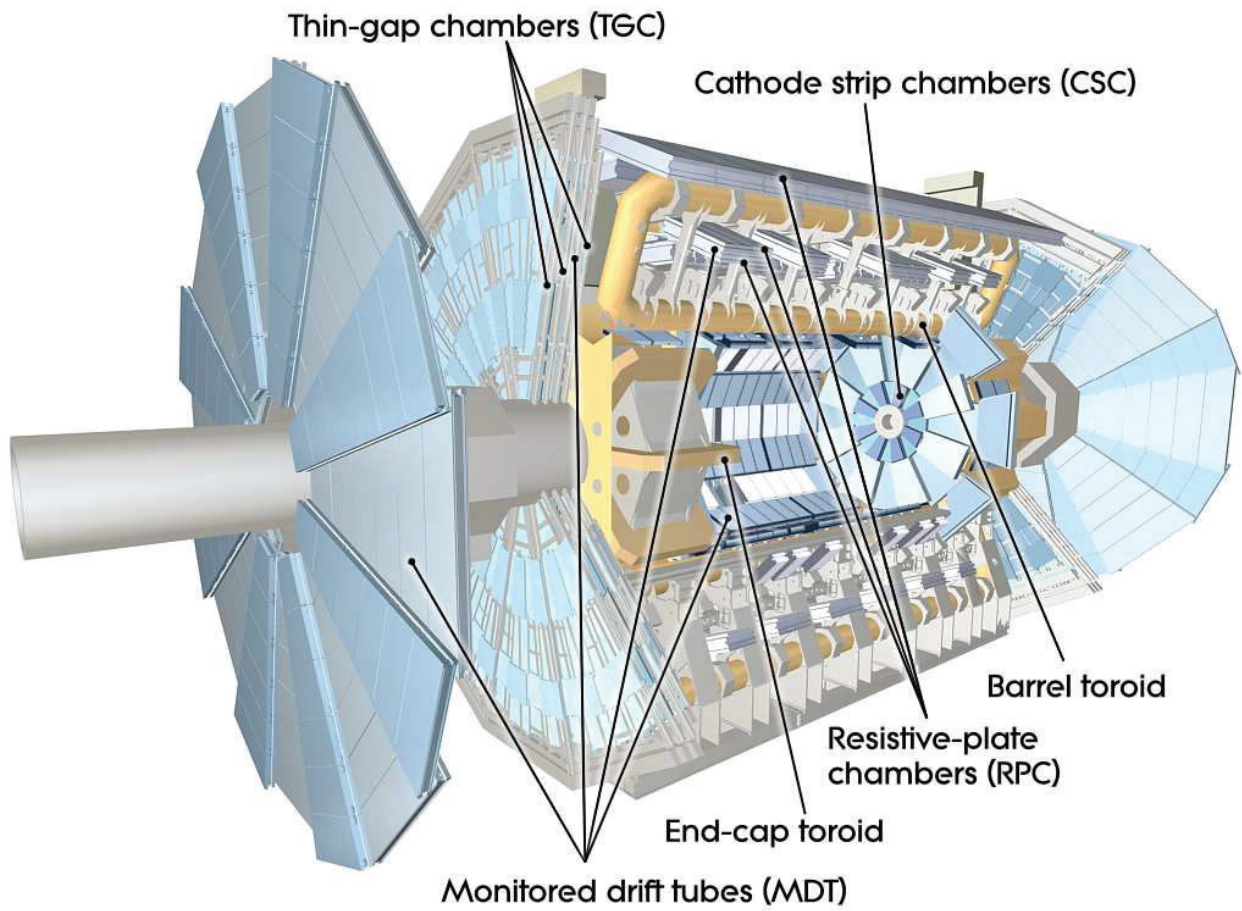
Figure 2.5: Cut-away view of the ATLAS muon system [30].

MDT

The Monitored Drift Tubes (MDTs) are used up to the maximum $|\eta|$ of 2.7, but the innermost layer only extends to $|\eta|$ of 2.0. Each drift tube is filled with an Argon-based gas mixture, and a tungsten-rhenium wire held at a 3080 V potential. When muons pass through the tube, the gas becomes ionized, and the freed electrons are picked up by the readout wire. [30]

CSC

The Cathode Strip Chambers (CSCs) are used as the innermost plane of the muon system at $|\eta|$ ranges above 2.0. In the high $|\eta|$ range, data rates become too high for MDT to be effective, so CSCs with a higher granularity are used. The CSCs consist of multiple positively charged anode wires, oriented in the radial direction, and multiple cathode strips oriented at a right angle with respect to the anodes. Each chamber is filled with an Argon-based gas mixture. Muons passing through the CSC ionize the gas, and the freed electrons are attracted to the anodes. Interaction with the gas en-route leads to an electron avalanche, which is read by a readout attached to the anode. The positively charge ions, also produced by the avalanche, are attracted to the cathode strips. The orientation of the anode wires and cathode scrips allows for the position of the muon to be reconstructed in the two dimensional plane of the end-cap.

RPC

The Resistive Plate Chambers (RPCs) are used by the muon trigger system and cover the barrel region of the detector, up to a maximum $|\eta|$ of 1.05. Each RPC is built from parallel electrode-plates separated by 2 mm, with a 4.9 kV/mm potential, and filled with a $C_2H_2F_4$-based gas mixture. Under normal operation, the RPC operates in an avalanche mode, similar to the CSC. Muons traveling through the chamber free electrons from the gas mixture, which form an electron avalanche on the way to the anode plate, while the positively charged ions are attracted to the cathode plate.

TGC

The Thin Gap Chambers (TGCs) are used in the end-caps of the muon trigger system, for $|\eta|$ between 1.05 and 2.7, but with a maximum $|\eta|$ of 2.4 used for triggering. TGCs operate on the same basic principle as CSCs, with multiple anode wires between cathode strips oriented at a right angle, but with a few notable differences in design, namely that the distance between the anode wires and cathode strips is smaller than the anode wire-to-wire distance. A 55/45 mixture of CO_2 and n-C_5H_{12} is used, with a cell geometry that allows for operation in a quasi-saturated mode [30]. Compared to RPCs, TGCs are able to handle the higher noise rates found in the forward regions of the detector, but have a somewhat slower response time.

Magnets

The electric charges of particles passing through the ID and muon spectrometer systems are determined by the deflection of those particles by the Coulomb force as they pass through a magnetic field. The ATLAS magnet systems [38] include a central solenoid magnet [39], surrounding the ID, and toroid magnet systems [40, 41] enveloping the muon spectrometer.

Solenoid

The solenoid magnet system sits between the inner detector and the LAr calorimeter, and provides a 2 T magnetic field parallel to the beam axis. This field causes the trajectory of charged particles to curve about the axis of the beam line while they pass through the inner detector's tracking systems. The direction of this curvature allows for the sign of the particle's charge to be deterimed, while the radius of curvature, when compared with the track's momentum, indicates the charge/mass ratio.

Toroid

The toroid magnets are used by the muon system, and are comprised of a set of 0.5 T barrel toroid magnets and two sets of 1 T end-cap toroids. The toroids produce magnetic fields with a normal axis parallel to the beam line, causing muon tracks to curve along the direction of the beam axis.

CHAPTER 3
EVENT RECONSTRUCTION

Events recorded by ATLAS are reconstructed multiple times. Initially, they are reconstructed online[1] by the ATLAS Trigger systems. The trigger performs a simplified version of the full event reconstruction, to limit the rate at which events are collected while still capturing events which may be of physics interest. A subset of events are then reconstructed offline[2] and used for data quality and calibration purposes. After calibration, the final bulk reconstruction takes place for the full dataset.

The remainder of this chapter briefly describes how events are reconstructed in the online trigger and offline subdetector systems, as well as particle level reconstruction and identification. Some emphasis is placed on the systems and objects of relevance to the analysis described later in this thesis.

Trigger

The ATLAS Trigger is structured in multiple levels. The Level-1 Trigger uses information from the calorimeters and the muon system to select regions of the detector which are likely to contain common physics objects, such as muons, electrons, or energetic jets. The High-Level Trigger (HLT) takes events passing the Level-1 Trigger and performs full event reconstruction. The HLT selects events based on relationships between high-level objects,

---

[1]During data taking, where latency is important.

[2]Not part of data taking, so latency is less critical.

such as events with significant missing transverse energy ($E_\mathrm{T}^\mathrm{miss}$), events with multiple high-energy jets, or combinations of different objects ($\tau + E_\mathrm{T}^\mathrm{miss}$, etc.), and the selected events are saved to tape for later analysis.

A trigger menu, defining the set of available triggers, can be altered throughout the year due to changes in run conditions, with the general trend that the available triggers become more restrictive[3] at higher luminosities. For the $H^\pm \to \tau\nu$ analysis described later in this thesis, the tau+lepton channel ($\tau + \ell$) uses the lowest (in p_T) available single lepton triggers, with thresholds up to 26 GeV, depending on the year and data taking period, for both the $\tau + e$ and $\tau + \mu$ final states. The complementary $\tau + \mathrm{jets}$ channel, with which the analysis shares tooling and some common background modeling, uses $E_\mathrm{T}^\mathrm{miss}$ triggers with thresholds of 70, 90, or 110 GeV, depending on the year and data taking period.

Inner Detector

The ID is used primarily for track reconstruction, with transition radiation in the TRT playing an additional role in electron identification. When charged particles pass through the inner detector, they interact with layers of active detector material, which are counted as hits. In the barrel region of the detector, this typically includes one hit in each of the 8 layers of the IBL+Pixel and SCT trackers, and ~30 in the TRT [42].

Tracks are reconstructed by extrapolating between hits across layers of the inner detector, first by using a rough clustering algorithm that identifies hits along a possible track trajectory, and then by filtering these track candidates with an ambiguity solver based on the relative quality of the fitted tracks [43], to reconstruct silicon-only tracks from hits in the IBL+Pixel and SCT trackers. These tracks are then extended from the silicon trackers to the TRT,

---

[3]I.e. have harsher thresholds, and so they select fewer events.

where TRT hits are associated with each track based on their compatibility with the silicon track seed, but the extension is not permitted to remove silicon hits from the track. This may be done by either fitting individual TRT hits, or fitting on clusters of hits. An outside-in approach may also be used, where TRT hits are extrapolated to the silicon trackers, which may allow additional tracks to be reconstructed in cases where there are ambiguous hits from multiple overlapping tracks in the silicon trackers.

Tracks play an important role in the identification of electrons and muons, distinction between electrons and photons, and jet flavor tagging, including the reconstruction of hadronic decays of taus, as described further in this chapter.

Calorimeters

Topologically adjacent calorimeter cells with significant energy are clustered to form higher level objects, called topo-clusters, which are used to reconstruct physics objects. In particular, topo-clusters are used to seed jet reconstruction, and clusters in the EM calorimeter are used for photon reconstruction and/or associated with electrons as part of the Egamma reconstruction algorithm.

Topo-cluster reconstruction begins with calorimeter cells, which are subject to noise from the readout electronics and pileup[4], so clustering is based on the energy in a cell relative to the cell's expected noise, also called the significance. Topo-clusters are typically seeded by cells with a significance greater than 4, which forms a proto-cluster. Neighboring cells are added to the proto cluster if their significance is above 2, with adjacent clusters merging, and a final set of neighboring cells is added from the boundary of a cluster if their significance exceeds

---

[4]From multiple interactions per bunch crossing, often on the order of 50 in LHC Run 2, or collisions in adjacent bunch crossings effectively superimposed due to longer response times of some detector material and readout electronics.

0 but fails to pass the usual threshold of 2. This procedure happens at the Electromagnetic (EM) scale, which reconstructs the energy of electrons and photons correctly, but does not apply hadronic calibrations to correct for the non-compensating nature of the calorimeters.

Large proto-clusters may be split if multiple local maxima are present. A cell which lies on the boundary between multiple local maxima is associated with the two high energy local maxima in the proto-cluster, such that each cell is shared by at most two clusters. The energy in such a cell is split between the two clusters using weights based on the relative sizes of the local maxima and their distance from the shared cell [44].

Muon

This analysis primarily uses combined muons, which are reconstructed from tracks in both the Muon Spectrometer (MS) and the inner detector. Hits in the MS are used to reconstruct track segments for muon candidates, corresponding to a straight-line fit between hits. These segments are then used to construct tracks in the MS, where a χ^2 fit is used to reject low quality tracks. The MS track is then extrapolated to a matching track in the inner detector. A combined refit is the performed, using hits from both the ID and the MS [45].

The $\tau + \mu$ and dilepton regions of this analysis use muons passing the tight identification criteria. This corresponds to combined muons with a tight $\chi^2 < 8$ requirement, hits in at least two stations of the MS, and at least 3 hits overall in the MDT. A loose selection on the compatibility between ID and MS momentum measurements is applied to suppress the contamination due to hadrons misidentified as muons, with a charge/momentum significance required to be less than 7. In about 0.5% of cases, the track uses an inside-out extrapolation from the ID to the MS, instead of the usual outside-in approach [45]. Events with loose muons are rejected by the other final states, which includes all muons passing the above

tight criteria excluding the $\chi^2 < 8$ and two station cuts. Additional muon reconstruction approaches are allowed in place of combined muons for loose muons in the $|\eta| < 0.1$ and $|\eta| > 2.5$ regions, as described in [45].

Egamma

Egamma objects (an electron e or photon γ) are characterized by significant energy in the electromagnetic calorimeter, with a relative absence of energy in either the hadronic calorimeter or the muon spectrometer. Electrons include a track from the inner detector extrapolated to the calorimeter cluster, as shown in Figure 3.1, while photons are nominally trackless. Photons that interact with material in the inner detector can produce conversion tracks, made up of e^+e^- pairs, which are characterized by a displaced vertex and a reduced number of hits in the inner detector.

"Loose", "medium", and "tight" electron identification working points are defined with 95%, 90%, and 80% efficiencies [47], respectively, using a likelihood-based discriminant. This likelihood-based discriminant is also used to reject $e \rightarrow \tau$ fakes in tau reconstruction. In this analysis, the tight working point is used to select electrons in the $\tau + e$ final state and the dilepton control region, while loose identification is used to reject events with unwanted electrons in other final states..

Jets

Jets in ATLAS are reconstructed from calorimeter clusters and any associated tracks [48]. While there are multiple ways to reconstruct jets, and multiple widths that may be used when clustering and associating tracks, many analyses in ATLAS, including the analysis
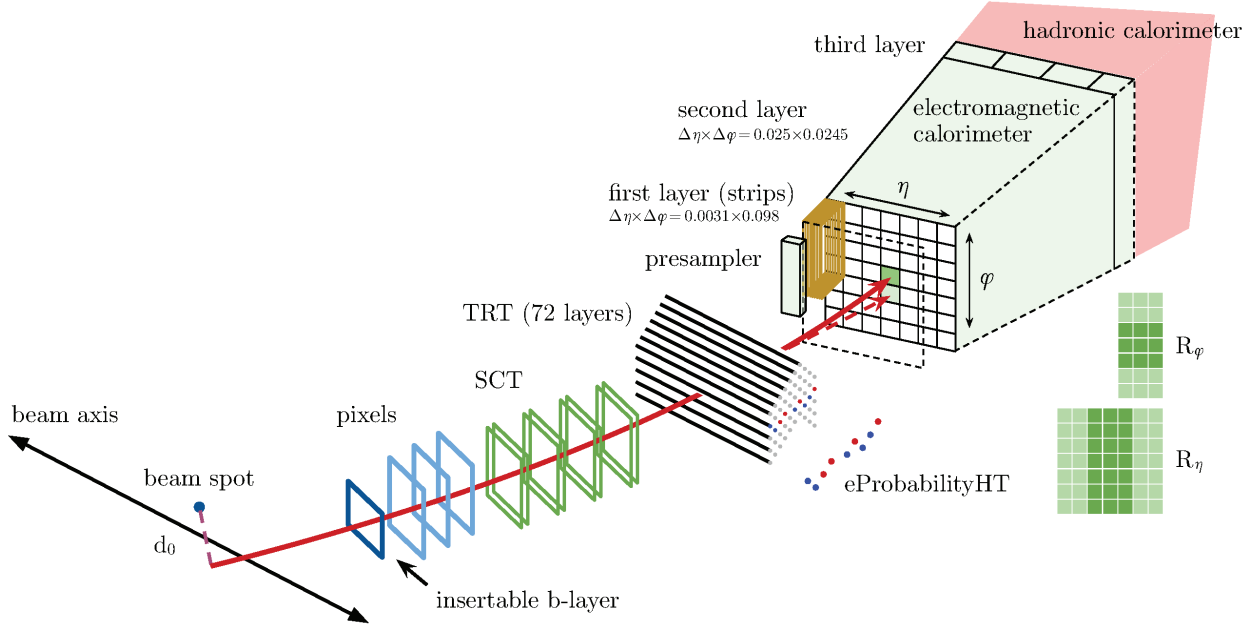
Figure 3.1: Schematic view of electron reconstruction and identification [46].

described in this thesis, use jets reconstructed with the anti-k_t [49] algorithm with a jet width of 0.4 in the $\eta\phi$ plane.

Flavor Tagging

Jets consist primarily of hadronized quarks and gluons produced from either the decay products of particles produced by the collision, or scattering of the initial particles. The flavor content of a jet (in terms of the presence of b, c, or lighter quarks) is useful for identifying events likely to contain other objects of interest[5]. Flavor tagging in ATLAS uses a Multi-Varate Analysis (MVA) approach to distingush between b, c, or light jets [50].

---

[5]E.g. a b-jet is present in virtually all t quark decays.

<u>Tau</u>

Taus are a notable exception to the rest of jet reconstruction and flavor tagging. About 65% of the time, tau leptons decay hadronically. This typically produces 1 or 3 charged mesons, most often pions ($\pi^{\pm}$) and 0 or more neutral mesons, typically neutral pions (π^0) [51]. Hadronic tau reconstruction is seeded with jets containing at most 5 tracks in a $\Delta R < 0.4$[6]. The tau cadidate is associated with tracks in $\Delta R < 0.2$ radius and energy calibrations are applied [Aad:2014rga]. The quality of the tau candidate is then assessed with a Boosted Decision Tree (BDT) identification algorithm [52], to reject fakes from hadronic jets, and a similar ID algorithm to reject $e \to \tau$ fakes.

Further details on τ reconstruction, along with a summary of my own contributions to it, are outlined in Appendix A.

$E_{\mathbf{T}}^{\mathbf{miss}}$

Missing transverse energy ($E_{\mathrm{T}}^{\mathrm{miss}}$) is used to infer the presence of undetectable particles, such as neutrinos (ν). This works because the initial particles are traveling along the direction of the beam line, so the momentum transverese to the direction of travel is negligible in the initial state. If the momentum of the final state particles are projected onto the plane transverse to the beam line, and a non-negligible net momentum is observed, then we know[7] that one or more undetected particles must account for the balance[8]. $E_{\mathrm{T}}^{\mathrm{miss}}$ is reconstructed

---

[6]Within a radius of 0.4 in the η/ϕ plane, with respect to the center of the seed jet.

[7]From conservation of momentum.

[8]With some random noise, as reconstruction, calibration, and energy resolution are all imperfect.

from energy in the calorimeter, with additional corrections from reconstructed tracks and calibrations from the objects reconstructed in the event [53].

CHAPTER 4

SEARCH FOR CHARGED HIGGS BOSONS

This chapter describes a search for charged Higgs bosons decaying to a charged tau lepton and a neutrino ($H^{\pm} \to \tau\nu$) in association with a leptonically decaying top quark. This is referred to as the tau+lep ($\tau + \ell$) final state, and serves to complement the τ+jets final state and other charged Higgs searches. Compared to τ+jets, $\tau + \ell$ has a lower branching fraction, but the presence of a charged e or μ allows the use of single-lepton triggers and helps to suppress background from QCD jet $\to \tau$ fakes. This reduces the impact of some systematics and improves sensitivity at low $m_{H^{\pm}}$, but the presence of an additional neutrino (the other final state object from the $W \to \ell\nu$ side of the top decay) makes separation of signal from background more difficult, as a significant portion of the total $E_{\mathrm{T}}^{\mathrm{miss}}$ in an event may come from objects not associated with the $H^{\pm}$ decay.

The rest of this chapter is structured as follows. It begins with a review of the expected signature of $H^{\pm}$ events, including object definitions and event selection, before moving on to a description of the analysis datasets and approach to background modeling, including control region studies. The analysis strategy is then described, with emphasis on the separation of signal from background. The topic then switches to modeling systematic uncertanties, and concludes with the fit results and limits that follow from the null search.

Signature and Event Selection

As described in the theory chapter, charged Higgs bosons are expected to be produced in association with a top quark, via a mass-dependent process that either resembles Standard Model $t\bar{t}$ or Wt production, but with $H^{\pm}$ substituting for a W. Therefore, an event should contain one or two b-jets, the hadronic or leptonic decay products of the W from the associated t decay, and the decay products of the chaged Higgs boson. In the $\tau + \ell$ channel, this consists of the τ, the ℓ (either e or μ), and significant $E_{\mathrm{T}}^{\mathrm{miss}}$ from at least three neutrinos – one prompt ν_τ from the $H^{\pm}$ decay, another from the τ decay, and a ν_ℓ from the leptonic decay of the t.

Object Definitions

Electrons must have $E_{\mathrm{T}}^e > 20$ GeV and $|\eta^e| < 2.7$, excluding a region $1.37 < |\eta^e| < 1.52$ at the boundary between the barrel and end-cap regions of the calorimeters. For the runs taken in 2015, the HLT required an electron to pass medium identification with $p_{\mathrm{T}}^e > 24$ GeV seeded by an L1 EM 20 GeV trigger object, or pass medium identification with $p_{\mathrm{T}}^e > 60$ GeV, or pass loose identification with $p_{\mathrm{T}}^e > 120$ GeV. In 2016, the electron trigger requirements are tight identification with $p_{\mathrm{T}}^e > 26$ GeV with a variable loose isolation requirement[1], or medium identification with $p_{\mathrm{T}}^e > 60$ GeV, or loose identification with $p_{\mathrm{T}}^e > 140$ GeV.

---

[1]The track-based e isolation requirement begins at $\Delta R = 0.2$ and shrinks with increasing p_{T}. with a calorimeter-based isolation requirement on energy deposited in a fixed cone with a radius of $\Delta R = 0.2$. This corresponds to an overall efficiency of 96%.

Muons must be trigger matched and have $p_T^{\mu} > 20$ GeV and $|\eta^{\mu}| < 2.5$, with a loose isolation requirement[2]. The muon trigger for 2015 requires $p_T^{\mu} > 20$ GeV with isolation and matched to a L1 muon above 15 GeV, or else $p_T^{\mu} > 50$ GeV. For the 2016 muon trigger, $p_T^{\mu} > 26$ GeV with isolation is required, or $p_T^{\mu} > 50$ GeV.

Jets are reconstructed using the anti-k_T algorithm with a radius of 0.4 in the $\eta\phi$ plane of the detector. Jets are required to have $p_T^{\text{jet}} > 25$ GeV and $|\eta^{\text{jet}}| < 2.5$. A Jet Vertex Tagger (JVT) [54] requirement is applied to jets with $p_T^{\text{jet}} < 60$ GeV and $|\eta^{\text{jet}}| < 2.4$, to select jets originating from the hard scatter vertex. Jets from b quarks are identified using a b-tagging algorithm [50] at a 70% efficiency working point. The visible decay products of hadronically decaying tau leptons must have $p_T^{\tau} > 30$ GeV and $|\eta^{\tau}| < 2.3$, excluding the transition between the barrel and end-cap regions of the calorimeters. A BDT-based τ-ID is used to distinguish the visible products of a hadronic τ decay from other sources of hadronic jets, with a medium ID working point defiend at 55% (40%) efficiency for 1-track (3-track) τs. Events are vetoed if they contain any additional loose or tighter τs, based on a 70% efficiency working point definition. In addition, and overlap-removal-based e-veto is applied, which removes τs if they overlap a reconstructed electron, at a 95% efficiency working point.

In cases multiple selected objects overlap, an overlap removal process is applied [19], in the following order: τ objects are discarded if they overlap within $\Delta R < 0.2$ of an electron or muon, which must pass a looser identification with $E_T > 20$ GeV or $p_T > 7$ GeV. Electrons are removed if they share an inner detector track with a muon. Electrons or muons within $\Delta R < 0.4$ of a b-tagged jet are discarded. Finally, jets are discarded if they are within $\Delta R < 0.2$ of the highest-p_T τ candidate or any remaining muons or electrons.

Missing transverse energy is defined as the transverse component of the negative vectoral sum of the identified physics objects, plus an additional soft term from energy in the

---

[2]Similar to the electron requirement, but the track-based isolation begins at $\Delta R = 0.3$. The isolation requirements has an efficiency of 99% for muons.

calorimeter and tracks originating from the primary vertex that are not associated with any selected object.

Event Selection

The $\tau + \ell$ signal region (SR) is split into $\tau + e$ and $\tau + \mu$ final states, which are defined as follows:

- Exactly 1 ℓ (e or μ), with $p_T^\ell > 30$ GeV, which must be trigger matched.
- Exactly 1 medium τ, with no additional loose or tighter τs in the event.
- The ℓ and τ must be of opposite sign.
- $E_T^{\mathrm{miss}} > 50$ GeV.
- ≥ 1 b-tagged jets.

This selection ensures orthogonality with the control regions, which are defined upon first use later in this chapter, as well as the fully hadronic $\tau + $ jets final state described in [19]. The object p_T and E_T^{miss} thresholds are set based on trigger and background modeling requirements.

Datasets

This analysis uses data collected by the ATLAS experiment from 36.1 ± 1.28 fb^{-1} of proton-proton collisions produced at $\sqrt{s} = 13$ TeV by the LHC in 2015 and 2016. This dataset includes events in the ATLAS "good run list" (GRL), which requires that all detector subsystems be operating within their normal range of acceptable parameters. Additional cleaning cuts are applied, which remove events where a reconstructed jet may have been

produced by noise or non-collision background. The $\tau + \ell$ channel uses a dataset that applies a loose preselection, with a requirement of at least 1 reconstructed electron or muon and 1 reconstructed jet.

Events with fake τ leptons arising from a misidentified jet are modeled with a data-driven approach using the dataset described in the next section. Standard Model backgrounds with true τ leptons, or $\ell \to \tau$ fakes, are modeled with Monte Carlo simulated events. This includes $t\bar{t}$ and single top, W+jets, Z/γ^*+jets, and diboson[3] events. This procedure is described in [19], and briefly restated as follows.

The backgrounds arising from $t\bar{t}$ and single top quark events in the Wt or s-channels are generated with Powheg-Box v2 [55–57] using the CT10 [58] PDF set. Single top t-channel events are generated with Powheg-Box v1 with the 4-flavor scheme[4] (4FS) at next-to-leading-order (NLO) and use the CT10f4 [59] fixed 4-flavor PDF set. Pythia v6.428 [60] is used with the CTEQ6L1 [61] PDF set for the underlying event, fragmentation, and parton showering, with the Perugia 2012 tune [62].

Backgrounds from W + jets or Z + jets processes are simulated with Sherpa v2.2.1 [63] together with the NNPDF3.0NNLO [64] PDF set. Matrix elements are calculated for up to two partons at NLO and four partons at LO using Comix [65] and OpenLoops [66], and they merged with the Sherpa parton shower [67] according to the ME+PS@NLO prescription [68] and normalized to the NNLO cross sections from FEWZ [69–71].

Diboson processes (WW, WZ and ZZ) are simulated at NLO using the Powheg-Box v2 generator, interfaced to the Pythia v8.186 parton shower model. The CT10nlo PDF set is used for the hard-scatter process, while the CTEQL1 PDF set is used for the parton shower. The non-perturbative effects are modelled using the AZNLO [72] tune.

---

[3]WW, WZ, or ZZ.

[4]In such a scheme, the proton contains u, d, s, and c quark flavors, but the b flavor content is negligible.

EVTGEN v1.2.0 [73] is used for the properties of bottom- and charm-hadron decays, except in samples generated with SHERPA. All simulated events are overlaid with additional minimum-bias events generated with PYTHIA v8.186 using the A2 [74]tune and the MSTW2008LO [75] PDF set to simulate the effect of multiple pp collisions per bunch crossing (pile-up). Simulated events are then weighted to have the same distribution of the number of collisions per bunch crossing as the data. All signal and background events are processed through a simulation [76] of the detector geometry and response based on GEANT4 [77] and reconstructed using the same algorithms as the data.

Signal Modeling

Charged Higgs signal is broadly organized into three categories based on $m_{H^\pm}$. Low mass signal events, from $90 - 160$ GeV, are modeled at leading order (LO), and include only $t\bar{t}$ events where one top quark decays to $H^\pm$ and a b quark. High-mass signal events, from $200 - 2000$ GeV, consists of single-top associated events generated at NLO with a 4FS. The intermediate mass range, from $160 - 180$ GeV, consists of LO non-resonant, single-top resonant, and touble top quark resonant processes with a W boson, a charged Higgs boson, and two b quarks, generated with the 4FS. In all cases, the parton-level generator is interfaced to PYTHIA v8.186 [78] with the A14 tune for the underlying event [79], and the NNPDF2.3 [80] parton distribution function (PDF) sets are used.

Background Modeling

Standard Model backgrounds with true taus are taken from Monte Carlo (MC) simulation. The largest such background is top quark production, primarily in the form of $t\bar{t}$ or

Wt. To constrain the systematic uncertainty, a dedicated $t\bar{t}$ control region is used. This region is defined by the same selection as the signal region, but the tau is replaced with a second other-flavor lepton, to give an $e + \mu$ selection, at least one of which must be trigger matched. This dilepton control region is shown in Figure 4.1a. The true-τ background also includes some contribution from semi-leptonic $Z \rightarrow \tau\tau$ and diboson events. A dilepton b-veto validation region (Figure 4.1b), with a non-negligible contribution from diboson events, is used as an additional cross check.

Although the presence of a light charged lepton suppresses much of the jet $\rightarrow \tau$ fakes from QCD, the $\tau + \ell$ final state retains a significant contribution from fakes originating from $W + \text{jets}$ events with a true ℓ from the W decay and a fake τ. Generally speaking, jet $\rightarrow \tau$ fakes are not necessarily modeled well by MC simulation, so a data-driven approach is desirable. This analysis borrows the jet $\rightarrow \tau$ fake modeling used in the $\tau + \text{jets}$ channel, which is described in [19]. The fake-factor procedure used in the analyses can be summarized as follows:

1. Define an anti-selection for taus, anti-τ, which selects objects that fail the nominal τ identification but pass a much looser selection[5].

2. Define control regions for QCD-like multi-jet (MJ) and $W + \text{jets}$ -like jet $\rightarrow \tau$ fakes. The MJ region uses a $\tau + \text{jets}$ selection with a b-veto and $E_\text{T}^\text{miss} < 80$ GeV. The $W + \text{jets}$ region uses a $\tau + \ell$ selection with a b-veto, no E_T^miss cut, and $60 \text{ GeV} < m_\text{T}(\ell, E_\text{T}^\text{miss}) < 160$ GeV.

3. Subtract the SM contribution, based on expectation from MC simulation, from true-τs passing the anti-τ selection to get $N_{\text{anti-}\tau}$, and from identified taus to get N_τ.

4. Define the fake factor $\text{FF} = \frac{N_{\text{fake-}\tau}}{N_{\text{anti-}\tau}}$ in the two control regions.

---

[5]The nominal selection is a medium p_T-dependent BDT score cut, provided by the tau working group. The loose selection must fail a working-group-provided loose BDT score cut while passing a looser fixed BDT score cut.

(a) Dilepton *b*-tag control region

(b) Dilepton *b*-veto validation region
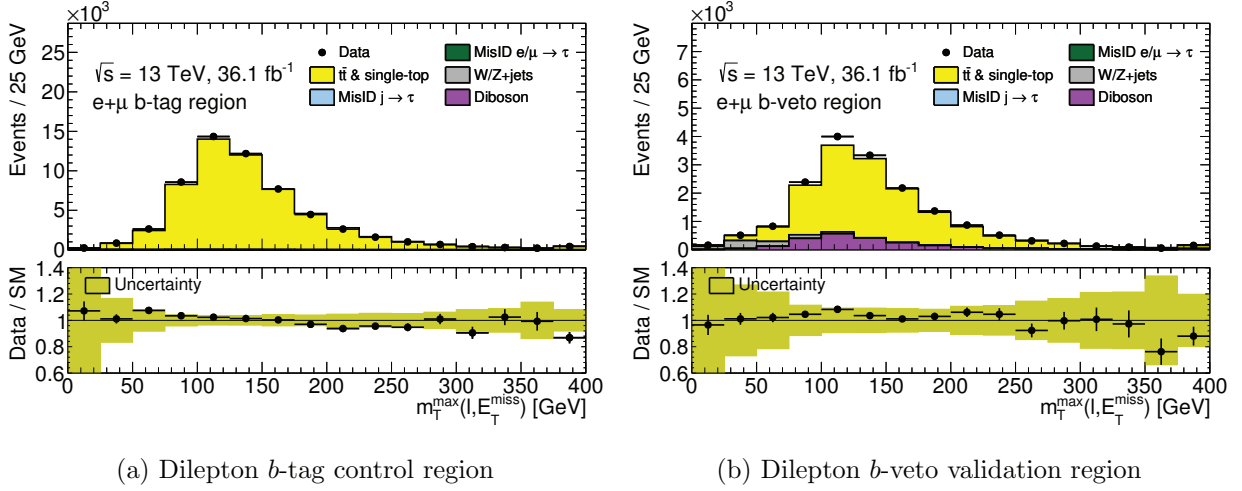
The *b*-tag region is used in the fitting machinery to constrain systematics related to the dominant background, Standard Model top-quark production.

Figure 4.1: Dilepton control regions.

5. In the signal region, measure the fraction of MJ-like jet $\to \tau$ fakes, α_{MJ}, by performing a template fit of the τ-ID score distributions of the selected anti-τs using template shapes from the anti-τ distributions in the Multi-jet and W+jets control regions, to get the relative contribution to fakes from each process.

6. Define $\mathrm{FF}_{\mathrm{sig}} = \alpha_{\mathrm{MJ}} \times \mathrm{FF}_{\mathrm{MJ}} + (1 - \alpha_{\mathrm{MJ}}) \times \mathrm{FF}_{W+\mathrm{jets}}$.

7. In the signal region, $N_{\mathrm{fake}\text{-}\tau} = \mathrm{FF}_{\mathrm{sig}} \times N_{\mathrm{anti}\text{-}\tau}$, where any contribution to $N_{\mathrm{anti}\text{-}\tau}$ from true-τs in SM processes is subtracted out using MC.

The fake factors (Figure 4.2) were measured for the τ + jets analysis and applied to both channels. Separate fake factors were produced for 1-track and 3-track τs, and binned as a function of p_{T}^{τ}. In the $\tau + \ell$ signal region, it was found that the α_{MJ} is very close to 0, due to the suppressed contribution from QCD-like fakes, but the approach was still used in the interest of consistency between the two channels. Same-sign control regions, dominated by fakes, are shown in Figure 4.3.

(a) Multi-jet and W+jets CRs

(b) After reweighting by α_{MJ}
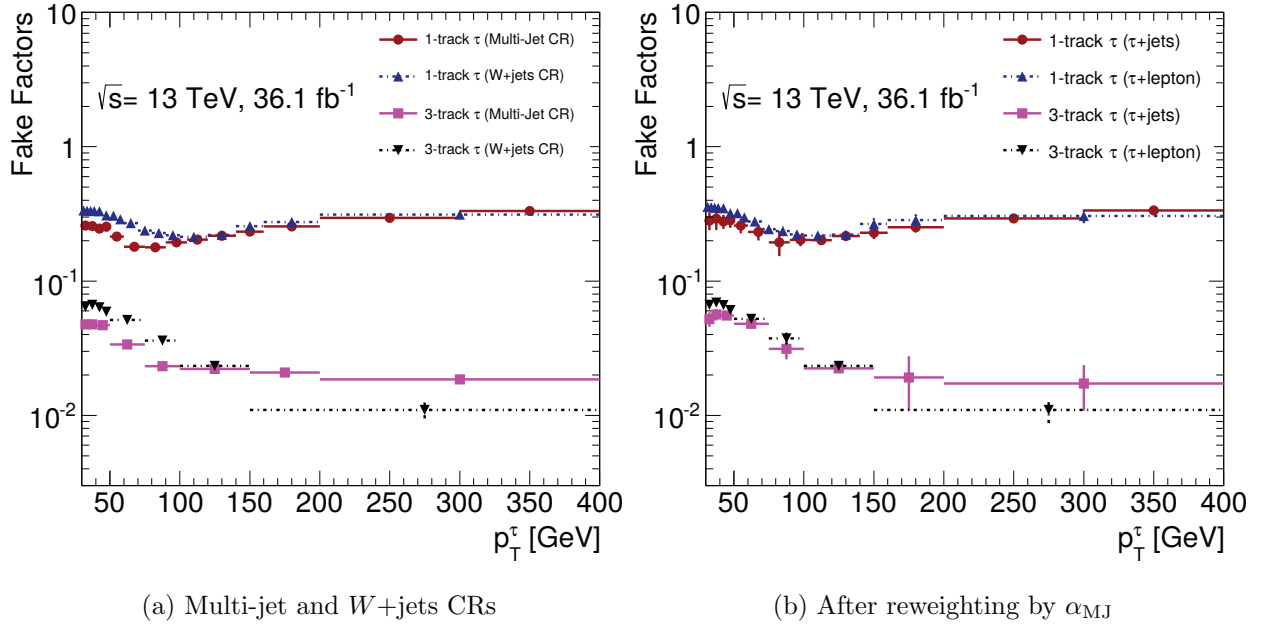
Obtained (a) in the multi-jet and W+jets CRs, (b) after reweighting by α_{MJ} in the $\tau_{\mathrm{had-vis}}$+jets and $\tau_{\mathrm{had-vis}}$+lepton channels. The errors shown come from the statistical uncertainty in a given p_{T}^{τ} bin (a) and with additional systematic uncertainties obtained from the combination in a given p_{T}^{τ} bin (b) [19].

Figure 4.2: Fake factors parameterized as a function of p_{T}^{τ} and the number of charged τ decay products.

(a) $\tau + e$ same-sign region (b) $\tau + \mu$ same-sign region
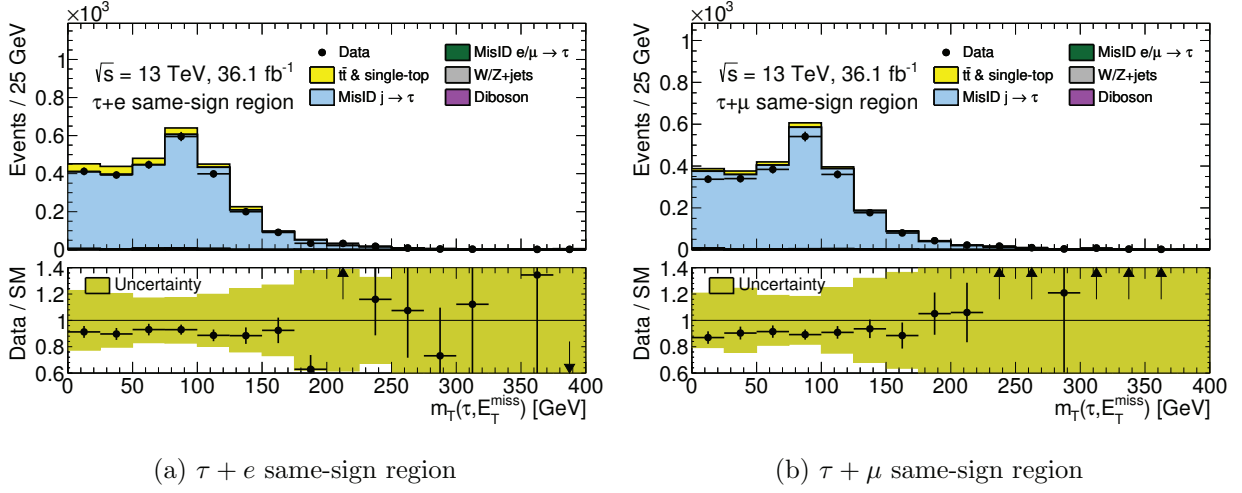
The variable shown, $m_{\mathrm{T}}(\tau, E_{\mathrm{T}}^{\mathrm{miss}}) = \sqrt{2p_{\mathrm{T}}^{\tau} E_{\mathrm{T}}^{\mathrm{miss}}(1 - \cos \Delta\phi_{\tau, E_{\mathrm{T}}^{\mathrm{miss}}})}$, was used in cut-based $H^{\pm} \to \tau\nu$ searches and as a benchmark for comparison in this analysis. Unlike other regions, the jet $\to \tau$ fakes in the same-sign regions contain a significant contribution from QCD-like events, which acts as an additional check of the α_{MJ} approach.

Figure 4.3: Same-sign control regions for the $\tau + \ell$ channel.

A validation region is used to check the true-τ background from other SM processes, primarily $Z \to \tau\tau$, and as an additional cross-check of $W \to \ell\nu$ events with jet $\to \tau$ fakes. This region is defined as the sum of the $\tau + e$ and $\tau + \mu$ signal regions, but with a b-veto applied to the selected jet(s), and is shown in Figure 4.4a. There is also a contribution from $\ell \to \tau$ fakes. These are also taken from MC simulation, and reweighted with scale factors provided by the tau combined performance group. The $e \to \tau$ contribution is then validated in a $Z \to e^{+}e^{-}$ region, shown in Figure 4.4b.

(a) b-veto control region

(b) $Z \to e^+ e^-$ control region
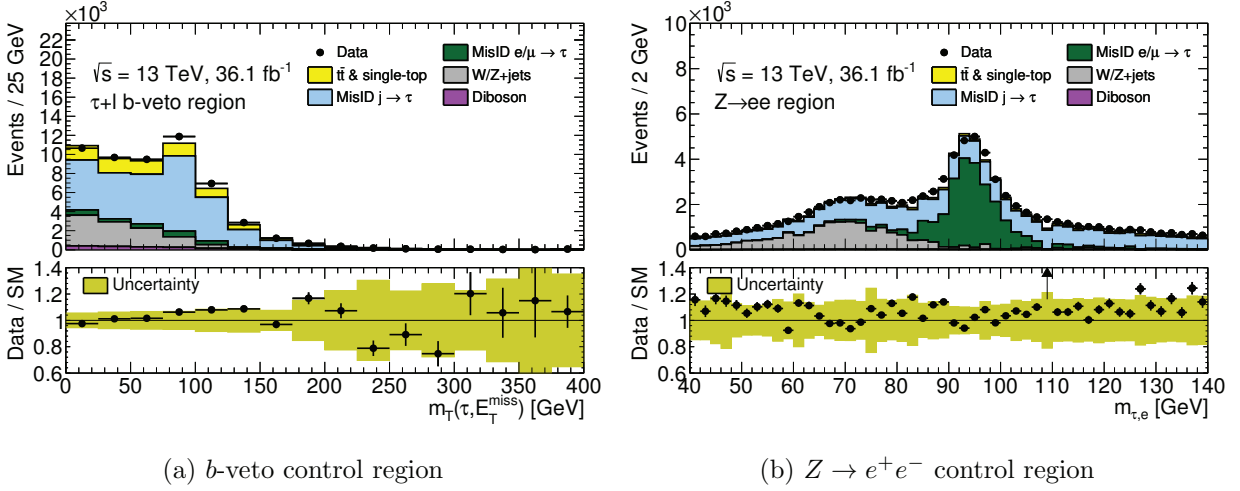
Each region applies a b-veto. The $Z \to e^+ e^-$ region removes the nominal $E_T^{miss} > 50$ GeV cut and requires the $\tau + e$ mass to fall within the displayed range.

Figure 4.4: The $\tau + \ell$ b-veto and $Z \to e^+ e^-$ control regions.

Analysis Strategy

The overall strategy of the analysis is as follows. A profile likelihood ratio is used as the test statistic in a simultaneous fit over three signal and two control regions. Signal regions are defined for the $\tau + $ jets, $\tau + e$, and $\tau + \mu$ final states. A dilepton control region, which is dominated by SM $t\bar{t}$, is used as a single-bin CR, to normalize the $t\bar{t}$ background.

The choice of discriminating variable in the SR has a large effect on the result, due to the difficulty of separating $H^{\pm}$ signal from $t\bar{t}$ or jet $\to \tau$ background over much of the mass range under consideration. This is particularly challenging for the $\tau + \ell$ channel, where the presence of an additional neutrino[6] can have a significant effect on the total E_T^{miss} in the event. A multi-variate analysis (MVA) approach was adopted to provide a discriminating variable

---

[6]From the associated leptonic top quark decay.

with a greater difference in distribution shape between signal and these backgrounds. The approach used was initially developed for the $\tau + \ell$ analysis. A compatible approach, using the same code but with different training datasets and MVA features, was later adopted by the $\tau + $ jets channel.

The remainder of this section describes the MVA procedure. This includes a high-level description of the Boosted Decision Tree model used as an MVA, the MVA training and evaluation procedure, a description of the features selected as inputs to the MVA, and validation of all available input features and output distributions in each control region.

Multi-Variate Analysis

BDTs are used to discriminate between signal and background, using the FastBDT [81] library with training via a TMVA [82] plug-in.

A decision tree (Figure 4.5) is a classifier based on a series of cuts organized into a binary tree. Beginning at a root node of the tree, a cut is selected to maximize the separation between signal and background. The tree then branches to two other nodes, for events which pass or fail the cut. In a fully grown decision tree, this process repeats until the terminal nodes of the tree contain only signal or only background. Shallow decision trees limit the number of cuts, and so they may not fully separate signal from background.

A BDT is an ensemble method. In an ensemble method, events are classified using an averaged response from multiple weak classifiers. In a BDT, shallow trees are typically[7] used as classifiers in the ensemble. The trees are trained in sequence, and misclassified events are reweighted (boosted) in the training of subsequent trees. Gradient boosting [83] is an algorithm that finds the reweighting by interpreting the problem as the minimization

---

[7]C.f. LightBGM, where trees are grown node-wise instead of layer-wise, and so they may not be shallow.
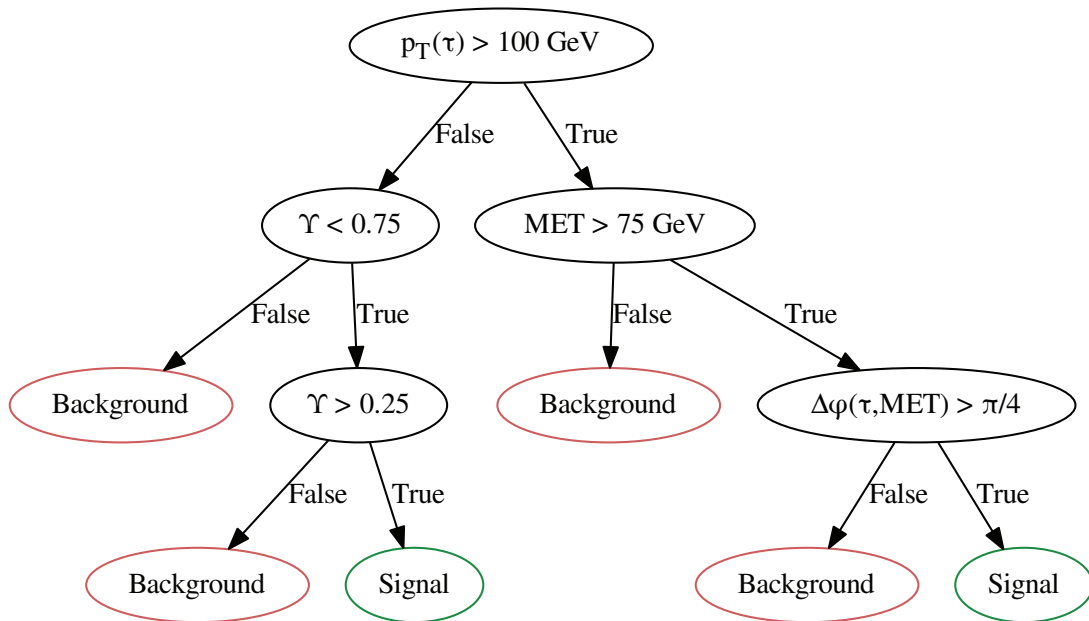
In practice, such a small tree will not fully separate signal and background, but would assign a score based on the total weights of signal and background events in the terminal node.

Figure 4.5: Example of a single decision tree.

of a cost function, and optimizes using gradient descent. FastBDT uses stochastic gradient boosting [84] for training. The motivation for using a BDT-based approach is described in Appendix C.

Training

The BDTs are trained on $H^{\pm} \to \tau\nu$ signal and $t\bar{t}$ background MC simulation using the $\tau + \ell$ selection. This includes MC simulated $t\bar{t}$ events with jet $\to \tau$ fakes. The $\tau + \ell$ event selection is applied to training events, combining the $\tau + e$ and $\tau + \mu$ final states to improve training statistics. The signal samples were divided into five mass bins, where the importance of each feature and event kinematics in each bin were found to be similar enough that the higher statistics from an inclusive training improves performance. The $H^{\pm}$ mass ranges used are:

- 90–120 GeV
- 130–160 GeV (using the low-mass 160 GeV sample)
- 160–180 GeV (using the intermediate-mass 160 GeV sample)
- 200–400 GeV
- 500–2000 GeV

The k-fold method is used in training and evaluation (Figure 4.6). Signal and background events are each sorted into k sets^{This was done based on `event_number % k`.}, and then the events in each set are evaluated evaluated[8] using a BDT which was trained on the other $k - 1$ sets. This allows each event to be evaluated with a BDT that does not include that event in its training set, which virtually eliminates the possibility of bias from overtraining.

---

[8]I.e. assigned BDT scores.

In the interest of simplicity, `event_number % k` is used to split events into disjoint sets. While $k = 2$ is sufficient to ensure independence of training and evaluation sets, $k = 5$ was used in this analysis to increase the training set size for each BDT.

Feature Selection

The features selected for the BDT are derived from the Lorentz vector components of the objects in the signal region event selection, and the track associated with the τ. Initially, the features were the Lorentz vector components, in terms of $(p_\mathrm{T}, \eta, \phi, m)$. The angular terms were replaced with angles between objects, as these are the quantities expected to be physically meaningful. Doing so effectively transforms events that were spread out over the whole detector into a narrower range of Δ terms, which is analogous to increasing training statistics. For object pairs where both $\Delta\phi$ and $\Delta\eta$ were defined, these were replaced with $\Delta\mathrm{R} = \sqrt{\Delta\eta^2 + \Delta\phi^2}$, as this reduces the number of features without affecting performance. The masses of the objects were removed, as these are either expected to be constant (in the case of the e or μ), or there's no expectation that they should be modeled as well as the other features (in the case of τs and b-jets).

In total, 10 features are used by the BDT:

- p_T^τ, p_T^ℓ, $p_\mathrm{T}^{b\text{-jet}}$, $E_\mathrm{T}^{\mathrm{miss}}$

	Fold 1	Fold 2	Fold 3	Fold 4	Fold 5	Background
Partition 1	Evaluation	Train	Train	Train	Train	Fold 1
Partition 2	Train	Evaluation	Train	Train	Train	Fold 2
Partition 3	Train	Train	Evaluation	Train	Train	Fold 3
Partition 4	Train	Train	Train	Evaluation	Train	Fold 4
Partition 5	Train	Train	Train	Train	Evaluation	Fold 5

Figure 4.6: The k-fold method for k=5.

- $\Delta\phi_{\tau,E_{\mathrm{T}}^{\mathrm{miss}}}$, $\Delta\phi_{\ell,E_{\mathrm{T}}^{\mathrm{miss}}}$, $\Delta\phi_{b\text{-jet},E_{\mathrm{T}}^{\mathrm{miss}}}$

- $\Delta R_{\tau,\ell}$, $\Delta R_{b\text{-jet},\ell}$

- $\Upsilon = 2\frac{p_{\mathrm{T}}^{\tau\text{-tracks}}}{p_{\mathrm{T}}^{\tau}} - 1$, for 1-prong τs and $m_{H^{\pm}} = 90\text{--}400$ GeV

For the highest $H^{\pm}$ mass bin, p_{T}^{τ}, $E_{\mathrm{T}}^{\mathrm{miss}}$, and $\Delta\phi_{\tau,E_{\mathrm{T}}^{\mathrm{miss}}}$ (the arguments of $m_{\mathrm{T}}(\tau, E_{\mathrm{T}}^{\mathrm{miss}})$) are sufficient to strongly separate signal and background. In the lowest mass bin, and particularly for $m_{H^{\pm}} = 90$ GeV, Υ provides most of the separation, as it is sensitive to the polarization of the τ lepton's parent particle. In the middle bins, including the intermediate mass range from 160–180 GeV, many features are of comparable importance. For consistency with the τ+jets channel, separate BDTs are trained for 1-prong and 3-prong taus below 500 GeV, with Υ included in only in the 1-prong training.

The BDT features are validated by looking in each validation region where all relevant objects are selected. BDT score are likewise validated in these regions, using a default (zero) Lorentz vector for any missing objects. This procedure and plots of the features and resulting BDT score distributions are shown in Appendix D. The analysis was blinded[9] when this validation was first preformed, and cross-checked in the signal regions after unblinding (shown in Figures 4.7–4.10).

Systematic Uncertainties

Systematic uncertainties are needed to account for effects that can alter either the event yield, leading to a change of overall normalization, or the event kinematics, which can result in the shape, of the BDT score distribution. An uncertainty of 3.2% is applied to the integrated luminosity as a normalization effect affecting all events modeled by MC simula-

---

[9]Control/validation regions were treated normally, but only background modeling was permitted in the signal region. This is done to avoid biasing the results.
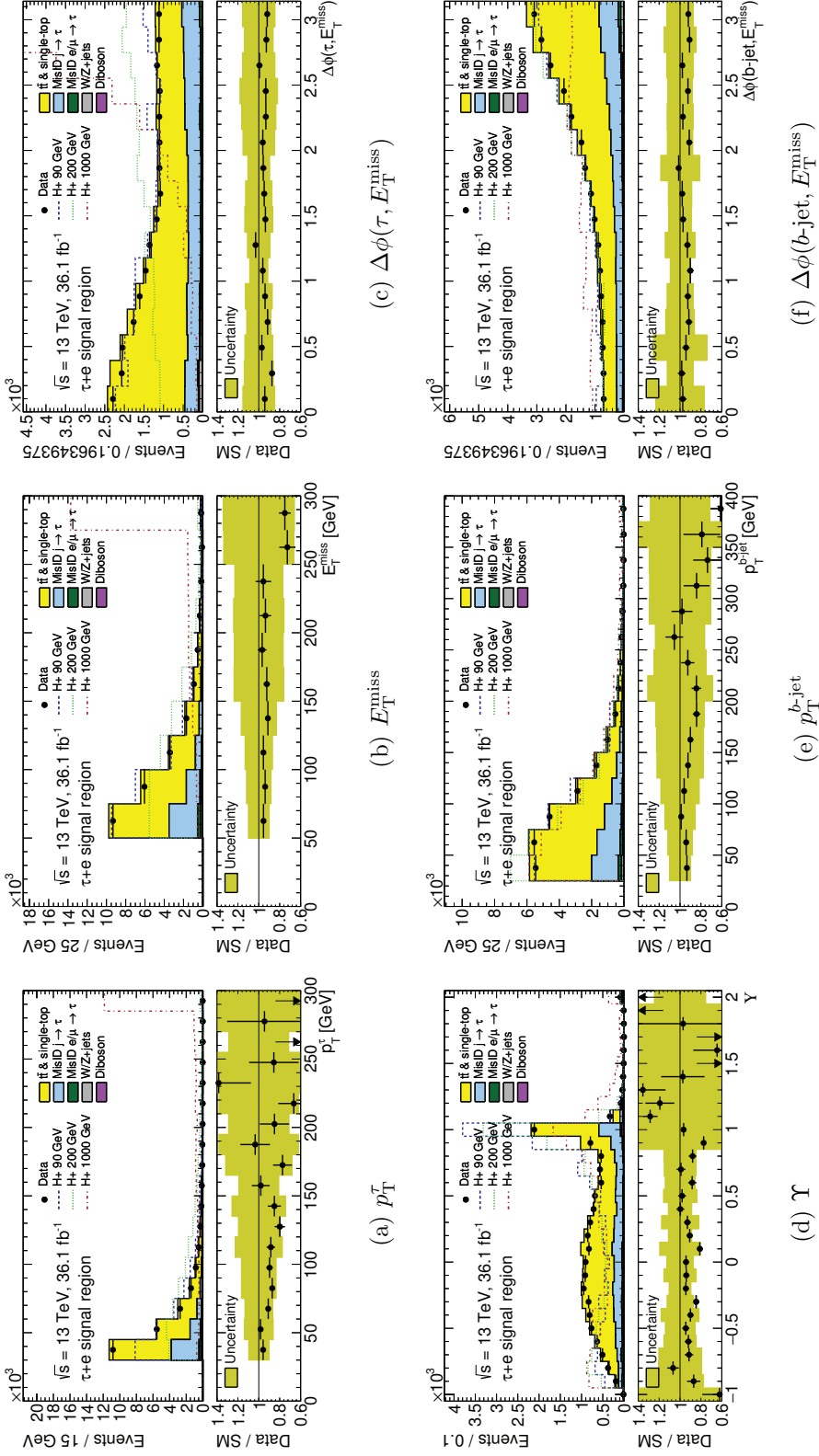
(a) p_T^τ

(b) E_T^{miss}

(c) $\Delta\phi(\tau, E_T^{miss})$

(d) Υ

(e) $p_T^{b\text{-}jet}$

(f) $\Delta\phi(b\text{-}jet, E_T^{miss})$

The uncertainty bands in the ratio plots include both the statistical and systematic uncertainties. The normalization of the signal (shown for illustration) corresponds to the integral of the background.

Figure 4.7: Features used in BDT training, shown for the $\tau + e$ signal region, excluding the features depending on an electron.
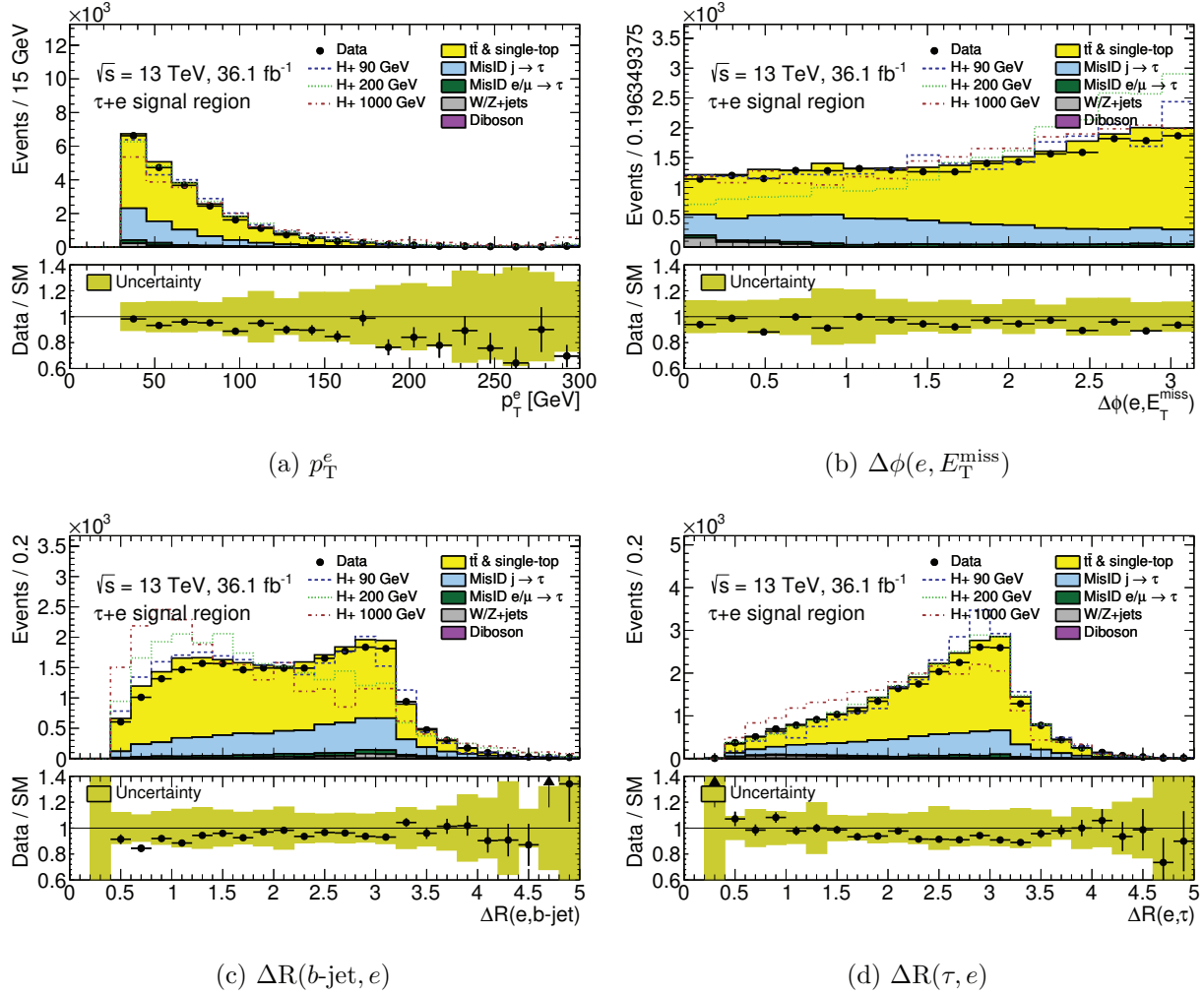
(a) p_T^e

(b) $\Delta\phi(e, E_T^{miss})$

(c) $\Delta R(b\text{-jet}, e)$

(d) $\Delta R(\tau, e)$

The uncertainty bands in the ratio plots include both the statistical and systematic uncertainties. The normalization of the signal (shown for illustration) corresponds to the integral of the background.

Figure 4.8: Features used in BDT training, shown for the $\tau + e$ signal region, including only the features depending on an electron.

(a) p_T^τ (b) E_T^{miss} (c) $\Delta\phi(\tau, E_T^{miss})$

(d) Υ (e) $p_T^{b\text{-jet}}$ (f) $\Delta\phi(b\text{-jet}, E_T^{miss})$
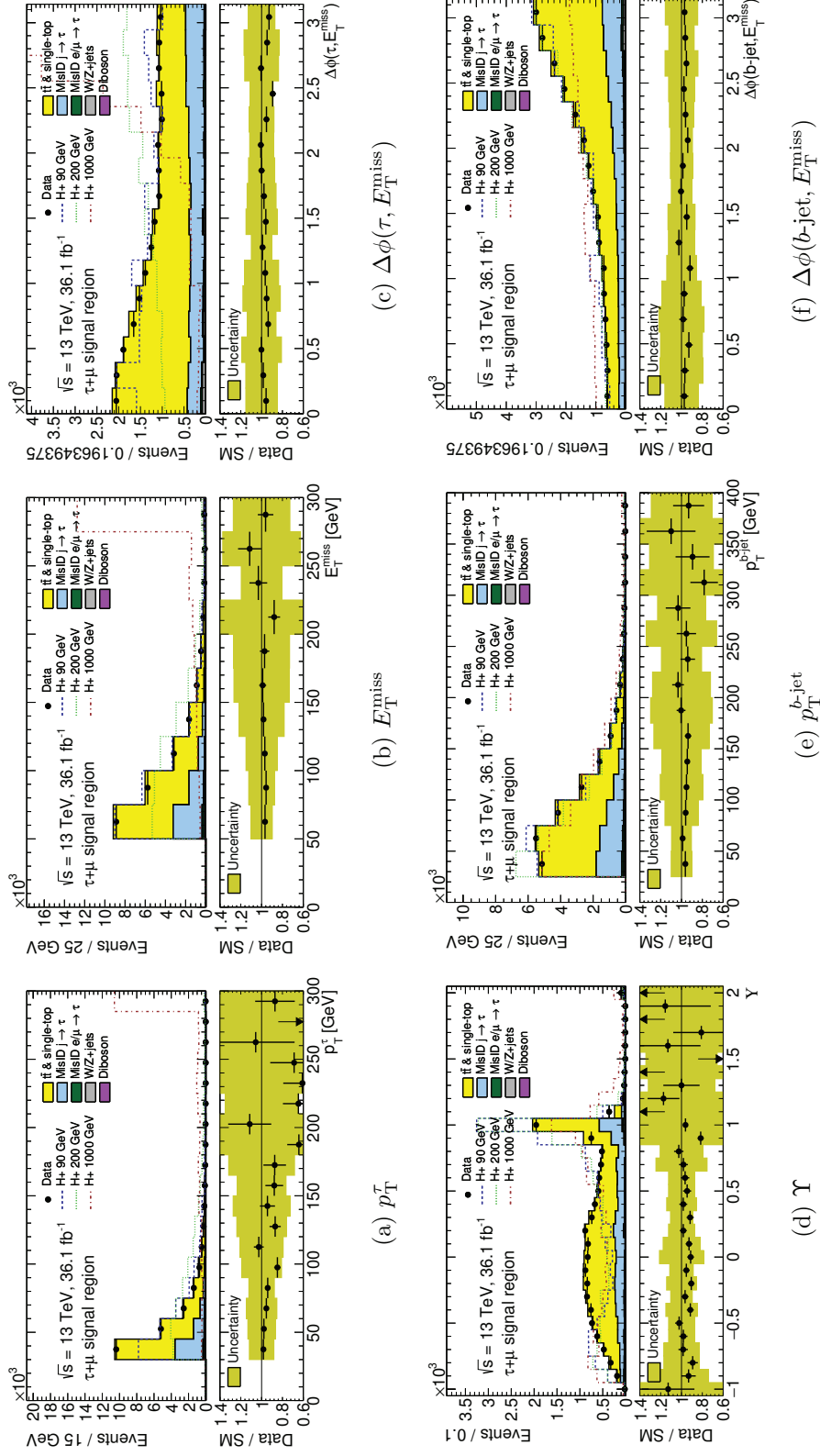
The uncertainty bands in the ratio plots include both the statistical and systematic uncertainties. The normalization of the signal (shown for illustration) corresponds to the integral of the background.

Figure 4.9: Features used in BDT training, shown for the $\tau + \mu$ signal region, excluding the features depending on a muon.

(a) p_{T}^{μ}

(b) $\Delta\phi(\mu, E_{\mathrm{T}}^{\mathrm{miss}})$

(c) $\Delta\mathrm{R}(b\text{-jet}, \mu)$

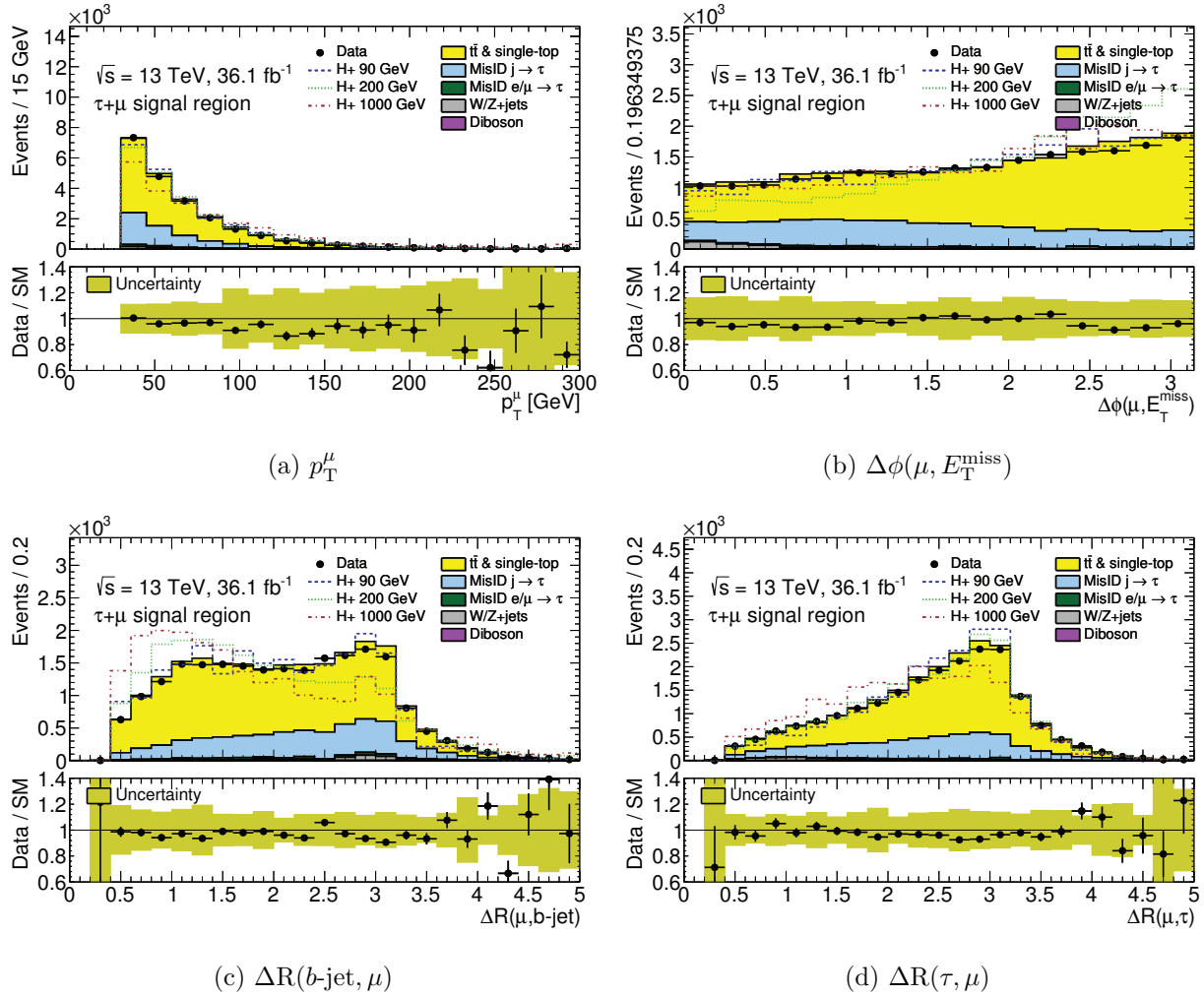(d) $\Delta\mathrm{R}(\tau, \mu)$

The uncertainty bands in the ratio plots include both the statistical and systematic uncertainties. The normalization of the signal (shown for illustration) corresponds to the integral of the background.

Figure 4.10: Features used in BDT training, shown for the $\tau + \mu$ signal region, including only the features depending on a muon.

tion. Object-level uncertainties are applied by varying the directly affected quantity by ± 1 standard deviation and observing the effect on event yields and distribution. These include reconstruction, identification, and energy scale calibration uncertainties for jets, τs, and the b-tagging algorithm. Light charged leptons (e and μ) are subject to similar treatment, and also include isolation and trigger uncertainties. The effect these uncertainties have on event yields in the dominant $t\bar{t}$ background, as well as a signal mass point at $m_{H^\pm} = 200$ GeV, are summarized in Tables 4.1 and 4.2.

Uncertainties related to the data-driven fake factor method were derived as a part of the fake-factor method used in the combined analysis, and applied to the $\tau + \ell$ channel. These include variations in the tau jet BDT score used in the anti-τ selection, a statistical uncertainty associated with the derivation of the fake factors themselves, and a shape uncertainty to the Smirnov transformation of the Υ variable. An uncertainty associated with the α_{MJ} method was found to have a negligible effect, so it was not included in the final treatment of the analysis.

Theoretical uncertainties are considered for signal and the dominant $t\bar{t}$ background. For the $t\bar{t}$ background, this includes uncertainties on the final state radiation (FSR), the matrix element generator, and the parton shower and underlying event. These were studied by replacing the nominal $t\bar{t}$ background with samples generated to study the effects of varying these parameters. Theoretical uncertainties affecting the signal are associated with the QCD scale, variations to the parton distribution function (PDF), and the parton shower and underlying event.

Results

The event yields for backgrounds, signal, and data, are summarized in Table 4.3.

Table 4.1: Effect of the main systematic uncertainties on the event yield for $t\bar{t}$ and signal events (m_{H^+} = 200 GeV) passing the nominal event selection of the $\tau_{\text{had–vis}}$+e channel

Source	Impact on the event yield (%)	
	$t\bar{t}$	H^+ 200 GeV
$\tau_{\text{had–vis}}$ reconstruction efficiency	±3.4	±3.3
$\tau_{\text{had–vis}}$-id uncertainty	±5.8	±5.8
$\tau_{\text{had–vis}}$-ℓ OLR	±0.9	±0.9
$\tau_{\text{had–vis}}$ energy scale	±4.1	±3.6
$\tau_{\text{had–vis}}$ energy scale (detector)	±0.8	±3.4
$\tau_{\text{had–vis}}$ energy scale (in-situ)	±3.8	±0.6
$\tau_{\text{had–vis}}$ energy scale (model)	±1.4	±0.9
e-id uncertainty	±0.7	±0.6
jet energy scale	±2.6	±2.2
b-jet tag efficiency	±2.1	±3.4
$E_{\text{T}}^{\text{miss}}$ soft term scale/resolution	±0.0	±1.4
trigger	±0.0	±0.0

The three components of the $\tau_{\text{had–vis}}$ energy scale uncertainty are shown here. [19]

Table 4.2: Effect of the main systematic uncertainties on the event yield for $t\bar{t}$ and signal events (m_{H^+} = 200 GeV) passing the nominal event selection of the $\tau_{\text{had–vis}}$+μ channel

Source	Impact on the event yield (%)	
	$t\bar{t}$	H^+ 200 GeV
$\tau_{\text{had–vis}}$ reconstruction efficiency	±3.4	±3.2
$\tau_{\text{had–vis}}$-id uncertainty	±5.8	±5.8
$\tau_{\text{had–vis}}$-ℓ OLR	±0.9	±1.0
$\tau_{\text{had–vis}}$ energy scale	±4.0	±3.8
$\tau_{\text{had–vis}}$ energy scale (detector)	±1.4	±3.8
$\tau_{\text{had–vis}}$ energy scale (in-situ)	±3.7	±0.0
$\tau_{\text{had–vis}}$ energy scale (model)	±0.6	±0.0
μ-id uncertainty	±1.2	±1.2
μ MS	±0.0	±1.4
jet energy scale	±2.1	±2.4
b-jet tag efficiency	±2.2	±3.1
$E_{\text{T}}^{\text{miss}}$ soft term scale/resolution	±0.0	±1.0
trigger	±1.1	±1.1

The three components of the $\tau_{\text{had–vis}}$ energy scale uncertainty are shown here. [19]

Table 4.3:   Expected event yields for the backgrounds and a hypothetical $H^\pm$ signal after all $\tau_{\text{had–vis}}$+lepton selection criteria, and comparison with 36.1 fb^{-1} of data

Sample	Event yields $\tau_{\text{had–vis}}$+electron			Event yields $\tau_{\text{had–vis}}$+muon		
True τ_{had}						
$\quad t\bar{t}$ & single-top-quark	17300	$\pm$ 90	$\pm$ 2500	15900	$\pm$ 80	$\pm$ 2500
$\quad Z \to \tau\tau$	433	$\pm$ 27	$\pm$ 80	352	$\pm$ 48	$\pm$ 43
$\quad$ Diboson (WW, WZ, ZZ)	39.3	$\pm$ 2.1	$\pm$ 4.5	32.3	$\pm$ 1.7	$\pm$ 3.6
Misidentified $e, \mu \to \tau_{\text{had–vis}}$	626	$\pm$ 27	$\pm$ 59	454	$\pm$ 16	$\pm$ 27
Misidentified jet $\to \tau_{\text{had–vis}}$	5640	$\pm$ 40	$\pm$ 450	5460	$\pm$ 40	$\pm$ 410
All backgrounds	24000	$\pm$ 100	$\pm$ 2600	22200	$\pm$ 100	$\pm$ 2500
H^+ (170 GeV), hMSSM $\tan\beta = 40$	850	$\pm$ 12	$\pm$ 65	852	$\pm$ 11	$\pm$ 66
H^+ (1000 GeV), hMSSM $\tan\beta = 40$	0.82	$\pm$ 0.02	$\pm$ 0.07	1.05	$\pm$ 0.02	$\pm$ 0.09
Data	22645			21419		

All yields are evaluated prior to using the multi-variate discriminant and applying the statistical fitting procedure. The values shown for the signal assume a charged Higgs boson mass of 170 and 1000 GeV, with a cross-section times branching fraction $\sigma(pp \to tbH^\pm) \times \text{BR}(H^\pm \to \tau\nu)$ corresponding to $\tan\beta = 40$ in the hMSSM benchmark scenario. Statistical and systematic uncertainties are quoted, respectively. [19]

A fit is performed, with $\tilde{q}_\mu$ [85] as the test statistic, which is based on a profile (log-)likelihood ratio. The likelihood is based on a product of Poisson distributions per bin of the test histogram(s). The likelihood ratio is defined as the ratio between the conditional maximum-likelihood (ML) estimator of the nuisance parameters (NPs) for a given signal hypothesis μ, to the unconditional ML estimators for μ and the NPs[10].

---

[10]In plain English: suppose we have a histogram, with some number of bins, where each bin has some number of observed events, expected background events, and a variable number of expected signal events (depending on the signal hypothesis μ). For a given μ, we can compute how likely each bin would taken on the observed value. The likelihood that all bins take on the observed value is the product of the probabilities for each bin. However, there are uncertainties – nuisance parameters – associated with the estimate for each bin. We can account for this by taking the probability that each NP is to contain some value, times the probability that we would see the observed bin contents if it had taken on that value. For a given μ, we select the value for each NP that maximizes the likelihood. That gives us the numerator of the ratio. The denominator is the same, but instead of using a fixed μ, it uses the μ value that maximizes the likelihood. The test statistic $\tilde{q}_\mu$ uses the log of the likelihood, because it reaches a maximum at the same point while being easier to work with.

The fit is performed over three signal regions for $\tau + \text{jets}$, $\tau + e$, and $\tau + \mu$, and a dilepton control region dominated by SM $t\bar{t}$. To perform the fit, templates are extracted for $\pm 1\sigma$ variations of each NP, and factored into separate shape and normalization components.

Templates extracted from the systematic variations are used in the fit to constrain systematic uncertainties, wherein the shape and normalization components are accounted for separately. Post-fit BDT score distributions in the signal region are shown in Figures 4.11 and 4.12.

The fit results are found to be in good agreement with the background-only hypothesis. The CL_s [86] procedure is used on the fit results to set a 95% confidence level upper limit on $\sigma(pp \rightarrow H^{\pm}) \times \text{BR}(H^{\pm} \rightarrow \tau\nu)$ as a function of $m_{H^{\pm}}$, with the results summarized in Figure 4.13. These correspond to upper limits between 4.2 pb and 2.5 fb for $m_{H^{\pm}}$ between 90 and 2000 GeV, or a branching fraction $\text{BR}(t \rightarrow bH^+) \times \text{BR}(H^+ \rightarrow \tau\nu)$ of between 0.25% and 0.031% for $m_{H^{\pm}}$ in the range of 90 to 160 GeV. These limits are interpreted in the hMSSM[11] [87] benchmark scenario to obtain a model-dependent exclusion on $\tan\beta$ and $m_{H^{\pm}}$ in Figure 4.14.
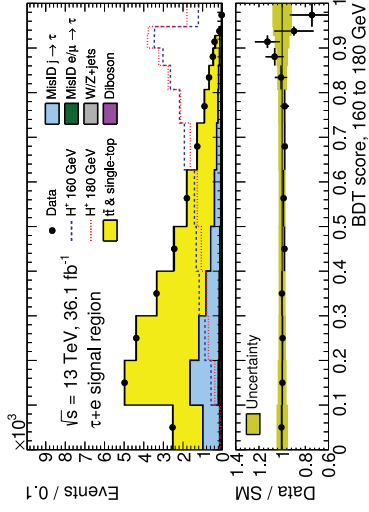
---

[11]The hMMSM scenario is based on a 125 GeV light Higgs boson h, and that the SUSY-breaking scale must be high enough to have not observed SUSY particles yet.
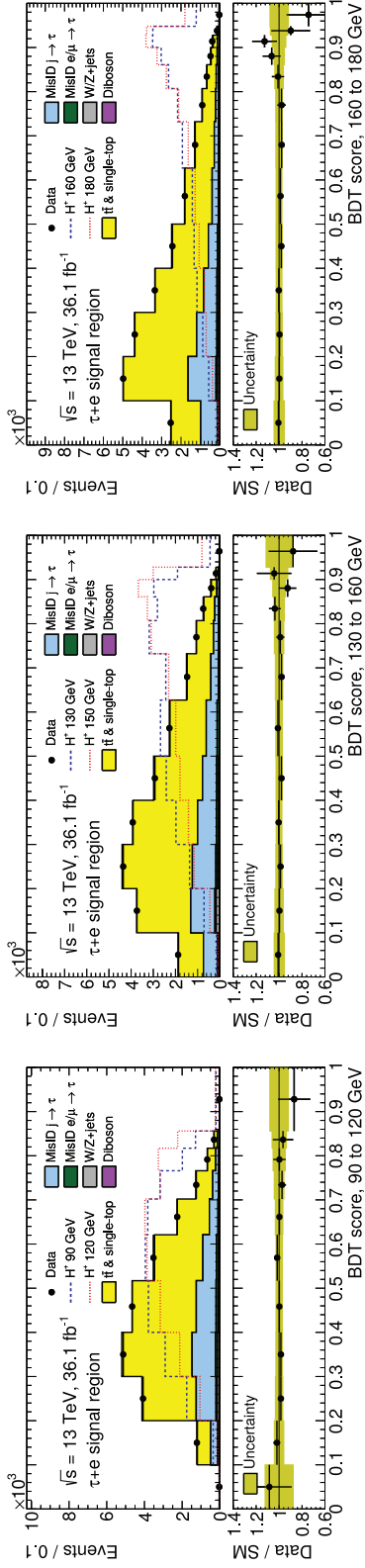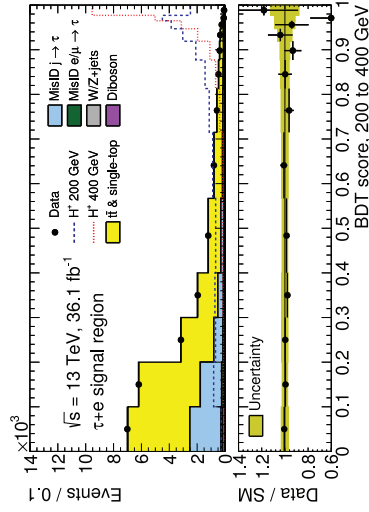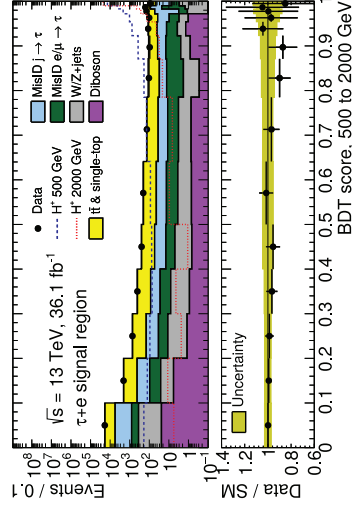
(a) $\tau + e$ SR 90–120 GeV
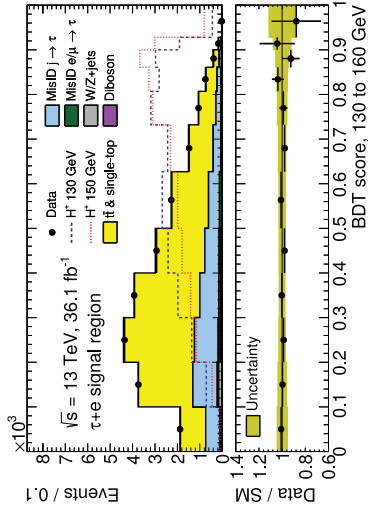
(b) $\tau + e$ SR 130–160 GeV
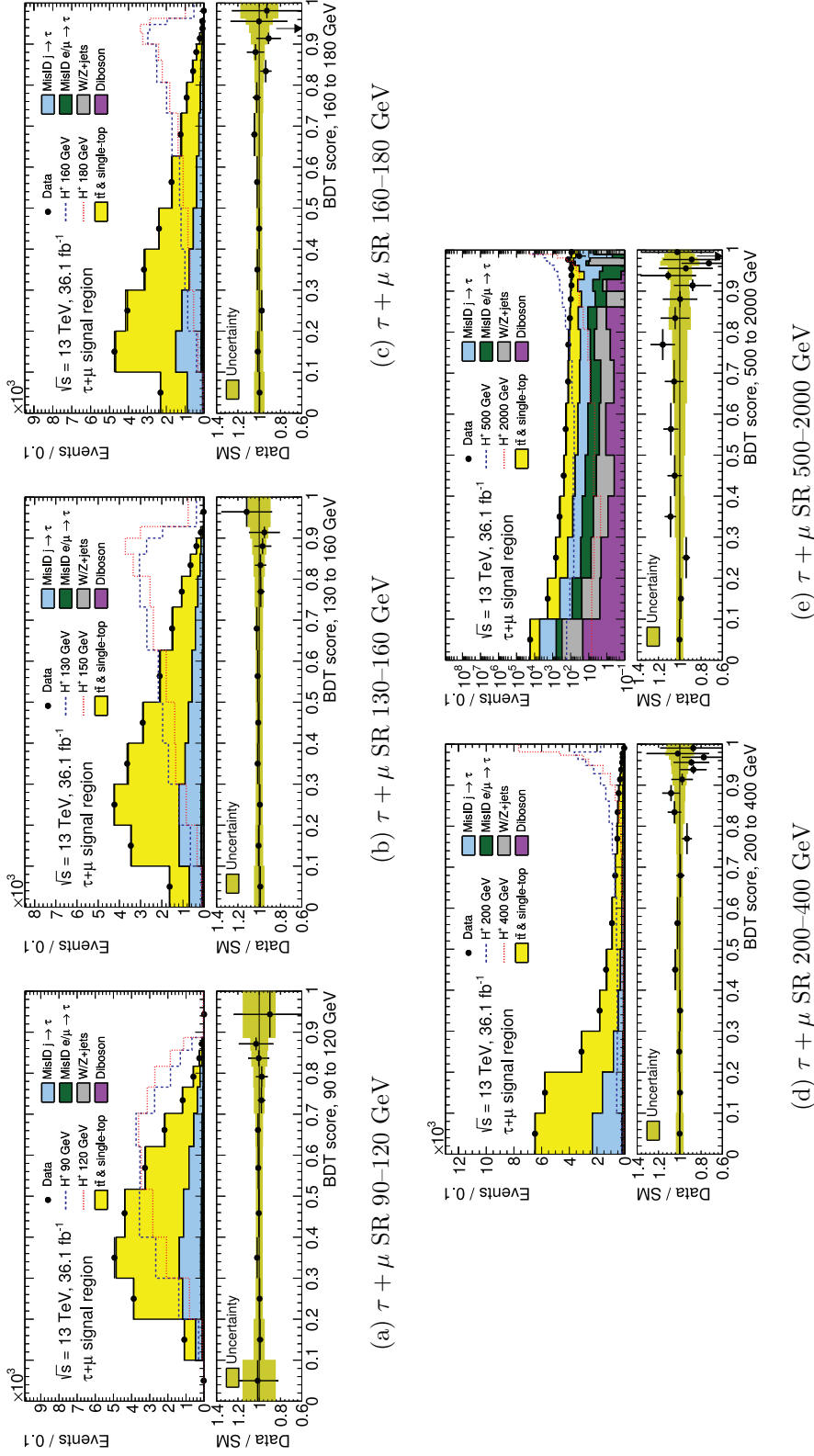
(c) $\tau + e$ SR 160–180 GeV

(d) $\tau + e$ SR 200–400 GeV

(e) $\tau + e$ SR 500–2000 GeV

Figure 4.11: BDT score distributions in the signal region of the $\tau + e$ channel.
Shown in the five mass ranges used for the BDT trainings after a fit to the data with the background-only hypothesis. The uncertainty bands in the ratio plots include both the statistical and systematic uncertainties. The normalization of the signal (shown for illustration) corresponds to the integral of the background.

(a) $\tau + \mu$ SR 90–120 GeV

(b) $\tau + \mu$ SR 130–160 GeV

(c) $\tau + \mu$ SR 160–180 GeV

(d) $\tau + \mu$ SR 200–400 GeV

(e) $\tau + \mu$ SR 500–2000 GeV

Figure 4.12: BDT score distributions in the signal region of the $\tau + \mu$ channel. Shown in the five mass ranges used for the BDT trainings after a fit to the data with the background-only hypothesis. The uncertainty bands in the ratio plots include both the statistical and systematic uncertainties. The normalization of the signal (shown for illustration) corresponds to the integral of the background.

(a) Limits in the low-mass range.

(b) Limits over the full mass range.
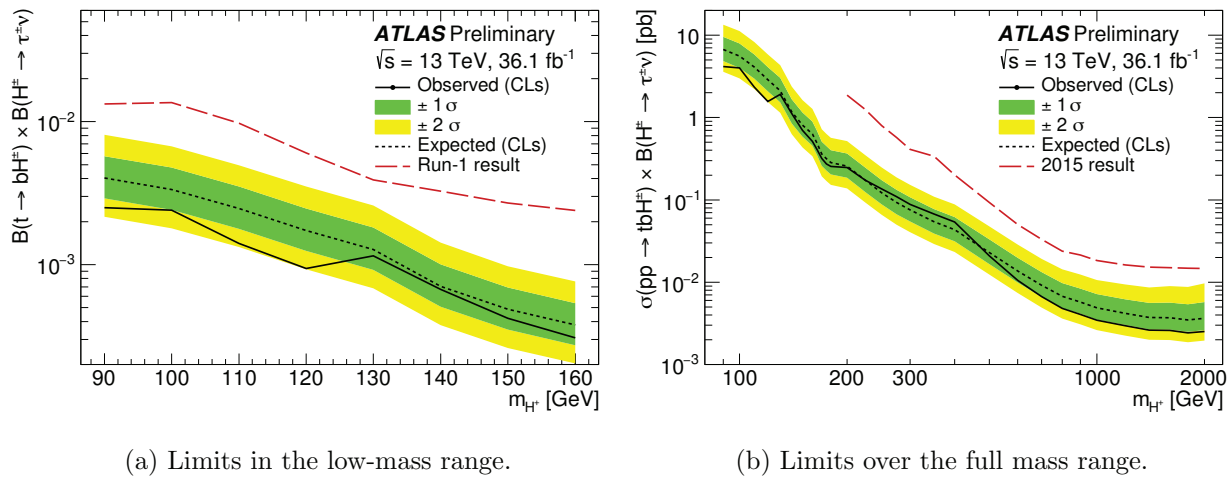
Figure 4.13: Expected and observed limits on the charged Higgs production and $H^{\pm} \to \tau\nu$ decay over the low and full mass ranges [19].
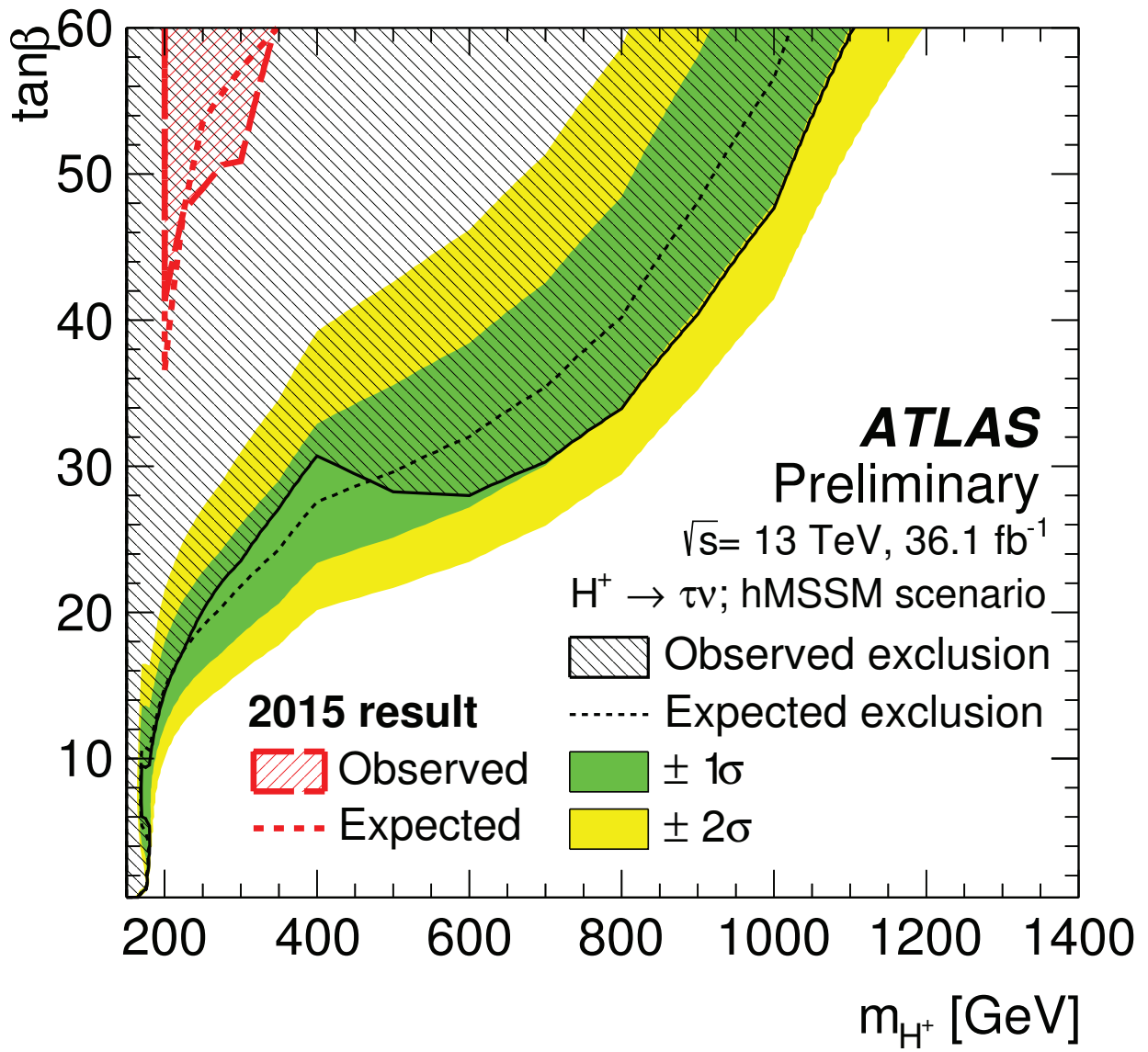
Figure 4.14: hMSSM paramter space, in terms of $\tan\beta$ vs $m_{H^\pm}$ [19].

CHAPTER 5

CONCLUSION

Charged Higgs bosons are expected in some Beyond Standard Model theories, most notably the Minimal Supersymmetric Standard Model. Observation of a charged Higgs boson would be a clear sign of new physics. Failing that, setting limits on the production and decay rates of charged Higgs bosons into their expected final states serves to constrain the available parameter space for BSM theories. Such constraints are necessary to motivate the creation of new models, refine the phenomenology of existing ones, and guide future searches.

A search for charged Higgs bosons has been performed using the ATLAS detector at the LHC for the $H^{\pm} \to \tau\nu$ channel in association with a leptonically decaying top quark in $36.1\,\text{fb}^{-1}$ of pp collision data at $\sqrt{s} = 13\,\text{TeV}$, and used in combination with the fully hadronic channel to set limits on the $H^{\pm}$ production cross section times its branching ratio into τ and ν_{τ}. Standard Model backgrounds with true taus or $\ell \to \tau$ fakes have been accounted for with Monte Carlo simulation. A data driven approach has been adopted, reusing work from the complementary fully hadronic channel, for jet $\to \tau$ fake modeling. The analysis considers charged Higgs bosons with masses between 90 and 2000 GeV, which includes for the first time masses in the "intermediate" mass range near the top quark mass, between about 160 and 180 GeV. Limits are set on the charged Higgs production cross section, times the branching ratio of $H^{\pm} \to \tau\nu$. These correspond to upper limits between 4.2 pb and 5.2 fb for $m_{H^{\pm}}$ between 90 and 2000 GeV, or a branching fraction $\text{BR}(t \to bH^{+}) \times \text{BR}(H^{+} \to \tau\nu)$ of between 0.25% and 0.031% for $m_{H^{\pm}}$ in the range of 90 to 160 GeV. These limits are then interpreted as limits on $m_{H^{\pm}}$ and $\tan\beta$ in the hMSSM benchmark scenario.

The limits set by the combined analysis are a significant improvement over previous $H^\pm \to \tau\nu$ analyses. The strength of these limits is attributed in part to the inclusion of the semi-leptonic channel and associated dilepton control region, and to migration of the analysis from a cut-based approach using $m_{\mathrm{T}}(\tau, E_{\mathrm{T}}^{\mathrm{miss}})$ to a Multi-Variate Analysis (MVA) approach. The presence of orthogonal signal regions and a dilepton control region serves to constrain the systematics associated with the large SM $t\bar{t}$ background, while the MVA approach improves sensitivity compared to $m_{\mathrm{T}}(\tau, E_{\mathrm{T}}^{\mathrm{miss}})$ for all but the highest masses. Care was taken to ensure that all features used by the MVA are observable in one or more control regions, that the background for each of these features is modeled well in each validation region where they are well defined, and that the resulting BDT score is likewise modeled well. A version of the k-fold approach with $k = 5$ was used to ensure that the training dataset was kept statistically independent from the dataset scored with each BDT, while preserving the full signal statistics for use in the analysis.

Leading up to the Run 2 data taking period and this analysis, I worked on a number of ATLAS service tasks that have an indirect bearing on the work presented here. The most relevant and significant contributions, outlined in the appendices, were from time spent as a Data Quality coordinator for the Tile Calorimeter, and from work as software developer for the tau working group. The Tile DQ work contributed to a successful Long Shutdown 1 maintenance and consolidation effort, and to a remarkably efficient 2015 data taking period in which there were no data losses attributed to the TileCal. As the hadronic calorimeter for the barrel region of the ATLAS detector, successful maintenance and operation of the TileCal is necessary for jet reconstruction and flavor tagging, including b-jets and jets from hadronic tau decays, and to $E_{\mathrm{T}}^{\mathrm{miss}}$ reconstruction. A portion of the tau software work was part of a wider LS1 software migration effort, which was necessary to keep up with the Run 2 data taking rate, without which this and other tau related analyses would suffer.

REFERENCES

[1] M. Shochet et al. Fast TracKer (FTK) Technical Design Report. Technical Report CERN-LHCC-2013-007. ATLAS-TDR-021, CERN, Jun 2013. ATLAS Fast Tracker Technical Design Report. URL: https://cds.cern.ch/record/1552953.

[2] David J. Gross and F. Wilczek. Ultraviolet behavior of non-abelian gauge theories. *Phys. Rev. Lett.*, 30:1343–1346, Jun 1973. URL: https://link.aps.org/doi/10.1103/PhysRevLett.30.1343, doi:10.1103/PhysRevLett.30.1343.

[3] H. D. Politzer. Reliable perturbative results for strong interactions? *Phys. Rev. Lett.*, 30:1346–1349, Jun 1973. URL: https://link.aps.org/doi/10.1103/PhysRevLett.30.1346, doi:10.1103/PhysRevLett.30.1346.

[4] S. L. Glashow. Partial Symmetries of Weak Interactions. *Nucl. Phys.*, 22:579–588, 1961. doi:10.1016/0029-5582(61)90469-2.

[5] Wikipedia contributors, Particle Data Group. Standard model of elementary particles, 2017. File: Standard Model of Elementary Particles.svg. URL: https://en.wikipedia.org/wiki/File:Standard_Model_of_Elementary_Particles.svg.

[6] J. J. Aubert et al. Experimental observation of a heavy particle j. *Phys. Rev. Lett.*, 33:1404–1406, Dec 1974. URL: https://link.aps.org/doi/10.1103/PhysRevLett.33.1404, doi:10.1103/PhysRevLett.33.1404.

[7] J. E. Augustin et al. Discovery of a narrow resonance in e^+e^- annihilation. *Phys. Rev. Lett.*, 33:1406–1408, Dec 1974. URL: https://link.aps.org/doi/10.1103/PhysRevLett.33.1406, doi:10.1103/PhysRevLett.33.1406.

[8] F. J. Hasert et al. Search for Elastic ν_μ Electron Scattering. *Phys. Lett.*, B46:121–124, 1973. [,5.11(1973)]. doi:10.1016/0370-2693(73)90494-2.

[9] F. J. Hasert et al. Observation of Neutrino Like Interactions Without Muon Or Electron in the Gargamelle Neutrino Experiment. *Phys. Lett.*, B46:138–140, 1973. [,5.15(1973)]. doi:10.1016/0370-2693(73)90499-1.

[10] A. Salam. Weak and Electromagnetic Interactions. *Conf. Proc.*, C680519:367–377, 1968.

[11] S. Weinberg. A model of leptons. *Phys. Rev. Lett.*, 19:1264–1266, Nov 1967. URL: https://link.aps.org/doi/10.1103/PhysRevLett.19.1264, doi:10.1103/PhysRevLett.19.1264.

[12] F. Englert and R. Brout. Broken symmetry and the mass of gauge vector mesons. *Phys. Rev. Lett.*, 13:321–323, Aug 1964. URL: `https://link.aps.org/doi/10.1103/PhysRevLett.13.321`, `doi:10.1103/PhysRevLett.13.321`.

[13] P. W. Higgs. Broken symmetries and the masses of gauge bosons. *Phys. Rev. Lett.*, 13:508–509, Oct 1964. URL: `https://link.aps.org/doi/10.1103/PhysRevLett.13.508`, `doi:10.1103/PhysRevLett.13.508`.

[14] G. S. Guralnik, C. R. Hagen, and T. W. B. Kibble. Global conservation laws and massless particles. *Phys. Rev. Lett.*, 13:585–587, Nov 1964. URL: `https://link.aps.org/doi/10.1103/PhysRevLett.13.585`, `doi:10.1103/PhysRevLett.13.585`.

[15] S. Dimopoulos and H. Georgi. Softly Broken Supersymmetry and SU(5). *Nucl. Phys.*, B193:150–162, 1981. `doi:10.1016/0550-3213(81)90522-8`.

[16] S. P. Martin. A Supersymmetry primer. 1997. Adv. Ser. Direct. High Energy Phys.18,1(1998). `arXiv:hep-ph/9709356`.

[17] ATLAS Collaboration. Observation of a new particle in the search for the Standard Model Higgs boson with the ATLAS detector at the LHC. *Phys. Lett.*, B716:1–29, 2012. `arXiv:1207.7214`, `doi:10.1016/j.physletb.2012.08.020`.

[18] CMS Collaboration. Observation of a new boson at a mass of 125 GeV with the CMS experiment at the LHC. *Phys. Lett.*, B716:30–61, 2012. `arXiv:1207.7235`, `doi:10.1016/j.physletb.2012.08.021`.

[19] ATLAS Collaboration. Search for charged Higgs bosons in the τ+jets and τ+lepton final states with 36.1 fb^1 of pp collision data recorded at $\sqrt{s} = 13\,TeV$ with the ATLAS experiment. (ATLAS-HIGG-2016-11-002), Jun 2018. URL: `https://atlas.web.cern.ch/Atlas/GROUPS/PHYSICS/PAPERS/HIGG-2016-11`.

[20] M. Flechl et al. Improved cross-section predictions for heavy charged Higgs boson production at the LHC. *Phys. Rev.*, D91(7):075015, 2015. `arXiv:1409.5615`, `doi:10.1103/PhysRevD.91.075015`.

[21] J. R. Andersen et al. Handbook of LHC Higgs Cross Sections: 3. Higgs Properties. 2013. `arXiv:1307.1347`, `doi:10.5170/CERN-2013-004`.

[22] M. Carena et al. MSSM Higgs Boson Searches at the LHC: Benchmark Scenarios after the Discovery of a Higgs-like Particle. *Eur. Phys. J.*, C73(9):2552, 2013. `arXiv:1302.7033`, `doi:10.1140/epjc/s10052-013-2552-1`.

[23] ATLAS Collaboration. Search for charged Higgs bosons in the τ+jets final state using 14.7 fb^{-1} of pp collision data recorded at $\sqrt{s} = 13$ TeV with the ATLAS experiment. Technical Report ATLAS-CONF-2016-088, CERN, Geneva, Aug 2016. URL: `https://cds.cern.ch/record/2206282`.

[24] ATLAS Collaboration. Search for charged Higgs bosons produced in association with a top quark and decaying via $H^{\pm} \to \tau\nu$ using pp collision data recorded at $\sqrt{s} = 13$ TeV by the ATLAS detector. *Phys. Lett.*, B759:555–574, 2016. `arXiv:1603.09203`, `doi:10.1016/j.physletb.2016.06.017`.

[25] ATLAS Collaboration. Search for charged Higgs bosons decaying via $H^{\pm} \to \tau^{\pm}\nu$ in fully hadronic final states using pp collision data at $\sqrt{s} = 8$ TeV with the ATLAS detector. *JHEP*, 03:088, 2015. `arXiv:1412.6663`, `doi:10.1007/JHEP03(2015)088`.

[26] CMS Collaboration. Search for charged Higgs bosons with the $H^{\pm} \to \tau^{\pm}\nu_{\tau}$ decay channel in the fully hadronic final state at $\sqrt{s} = 13$ TeV. Technical Report CMS-PAS-HIG-16-031, CERN, Geneva, 2016. URL: `https://cds.cern.ch/record/2223865`.

[27] CERN. The Large Electron-Positron Collider. Jul 2012. URL: `https://cds.cern.ch/record/1997351`.

[28] C. Pralavorio. Record luminosity: well done LHC. Nov 2017. URL: `https://cds.cern.ch/record/2295027`.

[29] O. S. Brüning et al. *LHC Design Report.* CERN Yellow Reports: Monographs. CERN, Geneva, 2004. URL: `https://cds.cern.ch/record/782076`.

[30] ATLAS Collaboration. The ATLAS Experiment at the CERN Large Hadron Collider. *JINST*, 3:S08003, 2008. `doi:10.1088/1748-0221/3/08/S08003`.

[31] J. Pequenao. Computer generated image of the whole ATLAS detector. Mar 2008. URL: `https://cds.cern.ch/record/1095924`.

[32] J. Pequenao and P. Schaffner. An computer generated image representing how ATLAS detects particles. Jan 2013. URL: `https://cds.cern.ch/record/1505342`.

[33] ATLAS Collaboration. *ATLAS inner detector: Technical Design Report, 1.* Technical Design Report ATLAS. CERN, Geneva, 1997. URL: `https://cds.cern.ch/record/331063`.

[34] M. Capeans et al. ATLAS Insertable B-Layer Technical Design Report. Technical Report CERN-LHCC-2010-013. ATLAS-TDR-19, Sep 2010. URL: `https://cds.cern.ch/record/1291633`.

[35] ATLAS Collaboration. *ATLAS liquid-argon calorimeter: Technical Design Report.* Technical Design Report ATLAS. CERN, Geneva, 1996. URL: `https://cds.cern.ch/record/331061`.

[36] ATLAS Collaboration. *ATLAS tile calorimeter: Technical Design Report.* Technical Design Report ATLAS. CERN, Geneva, 1996. URL: `https://cds.cern.ch/record/331062`.

[37] ATLAS Collaboration. *ATLAS muon spectrometer: Technical Design Report.* Technical Design Report ATLAS. CERN, Geneva, 1997. URL: `https://cds.cern.ch/record/331068`.

[38] ATLAS Collaboration. *ATLAS magnet system: Technical Design Report, 1.* Technical Design Report ATLAS. CERN, Geneva, 1997. URL: `https://cds.cern.ch/record/338080`.

[39] ATLAS Collaboration. *ATLAS central solenoid: Technical Design Report.* Technical Design Report ATLAS. CERN, Geneva, 1997. Electronic version not available. URL: `https://cds.cern.ch/record/331067`.

[40] J. P. Badiou et al. *ATLAS barrel toroid: Technical Design Report.* Technical Design Report ATLAS. CERN, Geneva, 1997. Electronic version not available. URL: `https://cds.cern.ch/record/331065`.

[41] ATLAS Collaboration. *ATLAS end-cap toroids: Technical Design Report.* Technical Design Report ATLAS. CERN, Geneva, 1997. Electronic version not available. URL: `https://cds.cern.ch/record/331066`.

[42] B. Mindur. ATLAS Transition Radiation Tracker (TRT): Straw tubes for tracking and particle identification at the Large Hadron Collider. Technical Report ATL-INDET-PROC-2016-001, CERN, Geneva, Mar 2016. URL: `https://cds.cern.ch/record/2139567`.

[43] T Cornelissen, M Elsing, I Gavrilenko, W Liebig, E Moyse, and A Salzburger. The new atlas track reconstruction (newt). *Journal of Physics: Conference Series*, 119(3):032014, 2008. URL: `http://stacks.iop.org/1742-6596/119/i=3/a=032014`.

[44] ATLAS Collaboration. Topological cell clustering in the ATLAS calorimeters and its performance in LHC Run 1. *Eur. Phys. J.*, C77:490, 2017. `arXiv:1603.02934`, `doi:10.1140/epjc/s10052-017-5004-5`.

[45] ATLAS Collaboration. Muon reconstruction performance of the ATLAS detector in protonproton collision data at $\sqrt{s} =$ 13 TeV. *Eur. Phys. J.*, C76(5):292, 2016. `arXiv:1603.05598`, `doi:10.1140/epjc/s10052-016-4120-y`.

[46] ATLAS Collaboration. Electron efficiency measurements with the ATLAS detector using the 2015 LHC proton-proton collision data. Technical Report ATLAS-CONF-2016-024, CERN, Geneva, Jun 2016. URL: `https://cds.cern.ch/record/2157687`.

[47] ATLAS Collaboration. Electron identification measurements in ATLAS using $\sqrt{s} =$ 13 TeV data with 50 ns bunch spacing. Technical Report ATL-PHYS-PUB-2015-041, CERN, Geneva, Sep 2015. URL: `https://cds.cern.ch/record/2048202`.

[48] ATLAS Collaboration. Properties of Jets and Inputs to Jet Reconstruction and Calibration with the ATLAS Detector Using Proton-Proton Collisions at $\sqrt{s} = 13$ TeV. Technical Report ATL-PHYS-PUB-2015-036, CERN, Geneva, Aug 2015. URL: `https://cds.cern.ch/record/2044564`.

[49] M. Cacciari, G. P. Salam, and G. Soyez. The Anti-k(t) jet clustering algorithm. *JHEP*, 04:063, 2008. `arXiv:0802.1189`, `doi:10.1088/1126-6708/2008/04/063`.

[50] ATLAS Collaboration. Optimisation of the ATLAS *b*-tagging performance for the 2016 LHC Run. Technical Report ATL-PHYS-PUB-2016-012, CERN, Geneva, Jun 2016. URL: `https://cds.cern.ch/record/2160731`.

[51] K. A. Olive et al. Review of Particle Physics. *Chin. Phys.*, C38:090001, 2014. `doi:10.1088/1674-1137/38/9/090001`.

[52] ATLAS Collaboration. Commissioning of the reconstruction of hadronic tau lepton decays in ATLAS using *pp* collisions at $\sqrt{s} = 13$ TeV. Technical Report ATL-PHYS-PUB-2015-025, CERN, Geneva, Jul 2015. URL: `https://cds.cern.ch/record/2037716`.

[53] ATLAS Collaboration. Performance of missing transverse momentum reconstruction with the ATLAS detector using proton-proton collisions at $\sqrt{s} = 13$ TeV. 2018. `arXiv:1802.08168`.

[54] ATLAS Collaboration. Tagging and suppression of pileup jets with the ATLAS detector. Technical Report ATLAS-CONF-2014-018, CERN, Geneva, May 2014. URL: `https://cds.cern.ch/record/1700870`.

[55] P. Nason. A New method for combining NLO QCD with shower Monte Carlo algorithms. *JHEP*, 11:040, 2004. `arXiv:hep-ph/0409146`, `doi:10.1088/1126-6708/2004/11/040`.

[56] S. Frixione, P. Nason, and C. Oleari. Matching NLO QCD computations with parton shower simulations: the POWHEG method. *JHEP*, 11:070, 2007. `arXiv:0709.2092`, `doi:10.1088/1126-6708/2007/11/070`.

[57] S. Alioli et al. A general framework for implementing NLO calculations in shower Monte Carlo programs: the POWHEG BOX. *JHEP*, 06:043, 2010. `arXiv:1002.2581`, `doi:10.1007/JHEP06(2010)043`.

[58] H. L. Lai et al. New parton distributions for collider physics. *Phys. Rev.*, D82:074024, 2010. `arXiv:1007.2241`, `doi:10.1103/PhysRevD.82.074024`.

[59] S. Dulat et al. New parton distribution functions from a global analysis of quantum chromodynamics. *Phys. Rev.*, D93(3):033006, 2016. `arXiv:1506.07443`, `doi:10.1103/PhysRevD.93.033006`.

[60] T. Sjöstrand, S. Mrenna, and P. Z. Skands. PYTHIA 6.4 physics and manual. *JHEP*, 05:026, 2006. `arXiv:hep-ph/0603175`, `doi:10.1088/1126-6708/2006/05/026`.

[61] J. Pumplin et al. New generation of parton distributions with uncertainties from global QCD analysis. *JHEP*, 07:012, 2002. `arXiv:hep-ph/0201195, doi:10.1088/1126-6708/2002/07/012`.

[62] P. Z. Skands. Tuning Monte Carlo generators: The Perugia tunes. *Phys. Rev.*, D82:074018, 2010. `arXiv:1005.3457, doi:10.1103/PhysRevD.82.074018`.

[63] T. Gleisberg et al. Event generation with SHERPA 1.1. *JHEP*, 02:007, 2009. `arXiv:0811.4622, doi:10.1088/1126-6708/2009/02/007`.

[64] R. D. Ball et al. Parton distributions for the LHC Run II. *JHEP*, 04:040, 2015. `arXiv:1410.8849, doi:10.1007/JHEP04(2015)040`.

[65] T. Gleisberg and S. Höche. Comix, a new matrix element generator. *JHEP*, 12:039, 2008. `arXiv:0808.3674, doi:10.1088/1126-6708/2008/12/039`.

[66] F. Cascioli, P. Maierhofer, and S. Pozzorini. Scattering Amplitudes with Open Loops. *Phys. Rev. Lett.*, 108:111601, 2012. `arXiv:1111.5206, doi:10.1103/PhysRevLett.108.111601`.

[67] S. Schumann and F. Krauss. A Parton shower algorithm based on Catani-Seymour dipole factorisation. *JHEP*, 03:038, 2008. `arXiv:0709.1027, doi:10.1088/1126-6708/2008/03/038`.

[68] S. Höche et al. QCD matrix elements + parton showers: The NLO case. *JHEP*, 04:027, 2013. `arXiv:1207.5030, doi:10.1007/JHEP04(2013)027`.

[69] C. Anastasiou et al. High precision QCD at hadron colliders: Electroweak gauge boson rapidity distributions at NNLO. *Phys. Rev.*, D69:094008, 2004. `arXiv:hep-ph/0312266, doi:10.1103/PhysRevD.69.094008`.

[70] K. Melnikov and F. Petriello. Electroweak gauge boson production at hadron colliders through $O(\alpha(s)^2)$. *Phys. Rev.*, D74:114017, 2006. `arXiv:hep-ph/0609070, doi:10.1103/PhysRevD.74.114017`.

[71] R. Gavin et al. FEWZ 2.0: A code for hadronic Z production at next-to-next-to-leading order. *Comput. Phys. Commun.*, 182:2388–2403, 2011. `arXiv:1011.3540, doi:10.1016/j.cpc.2011.06.008`.

[72] ATLAS Collaboration. Measurement of the Z/γ^* boson transverse momentum distribution in *pp* collisions at $\sqrt{s} = 7$ TeV with the ATLAS detector. *JHEP*, 09:145, 2014. `arXiv:1406.3660, doi:10.1007/JHEP09(2014)145`.

[73] D. J. Lange. The EvtGen particle decay simulation package. *Nucl. Instrum. Meth.*, A462:152–155, 2001. `doi:10.1016/S0168-9002(01)00089-4`.

[74] ATLAS Collaboration. Summary of ATLAS Pythia 8 tunes. ATL-PHYS-PUB-2012-003, 2012. URL: https://cds.cern.ch/record/1474107.

[75] A. D. Martin, W. J. Stirling, R. S. Thorne, and G. Watt. Parton distributions for the LHC. *Eur. Phys. J.*, C63:189–285, 2009. arXiv:0901.0002, doi:10.1140/epjc/s10052-009-1072-5.

[76] ATLAS Collaboration. The ATLAS Simulation Infrastructure. *Eur. Phys. J.*, C70:823–874, 2010. arXiv:1005.4568, doi:10.1140/epjc/s10052-010-1429-9.

[77] S. Agostinelli et al. GEANT4 – a simulation toolkit. *Nucl. Instrum. Meth.*, A506:250–303, 2003. doi:10.1016/S0168-9002(03)01368-8.

[78] T. Sjöstrand, S. Mrenna, and P. Z. Skands. A brief introduction to PYTHIA 8.1. *Comput. Phys. Commun.*, 178:852–867, 2008. arXiv:0710.3820, doi:10.1016/j.cpc.2008.01.036.

[79] ATLAS Collaboration. ATLAS Run 1 Pythia8 tunes. ATL-PHYS-PUB-2014-021, 2014. URL: https://cds.cern.ch/record/1966419.

[80] R. D. Ball et al. Parton distributions with LHC data. *Nucl. Phys.*, B867:244–289, 2013. arXiv:1207.1303, doi:10.1016/j.nuclphysb.2012.10.003.

[81] T. Keck. FastBDT: A speed-optimized and cache-friendly implementation of stochastic gradient-boosted decision trees for multivariate classification. *ArXiv e-prints*, September 2016. arXiv:1609.06119.

[82] A. Hoecker et al. TMVA: Toolkit for Multivariate Data Analysis. *PoS*, ACAT:040, 2007. arXiv:physics/0703039.

[83] J. H. Friedman. Greedy function approximation: A gradient boosting machine. *Annals of Statistics*, 29:1189–1232, 2000.

[84] J. H. Friedman. Stochastic gradient boosting. *Computational Statistics and Data Analysis*, 38:367–378, 1999.

[85] G. Cowan et al. Asymptotic formulae for likelihood-based tests of new physics. *Eur. Phys. J.*, C71:1554, 2011. [Erratum: Eur. Phys. J.C73,2501(2013)]. arXiv:1007.1727, doi:10.1140/epjc/s10052-011-1554-0,10.1140/epjc/s10052-013-2501-z.

[86] A. L. Read. Presentation of search results: the cl_s technique. *Journal of Physics G: Nuclear and Particle Physics*, 28(10):2693, 2002. URL: http://stacks.iop.org/0954-3899/28/i=10/a=313.

[87] A. Djouadi et al. The post-Higgs MSSM scenario: Habemus MSSM? *Eur. Phys. J.*, C73:2650, 2013. arXiv:1307.5205, doi:10.1140/epjc/s10052-013-2650-0.

[88] ATLAS Collaboration. Reconstruction, Energy Calibration, and Identification of Hadronically Decaying Tau Leptons in the ATLAS Experiment for Run-2 of the LHC. Technical Report ATL-PHYS-PUB-2015-045, CERN, Geneva, Nov 2015. URL: `https://atlas.web.cern.ch/Atlas/GROUPS/PHYSICS/PUBNOTES/ATL-PHYS-PUB-2015-045`.

[89] ATLAS Collaboration. Tau public collision plots, 2016. Performance Plot for ICHEP 2016 (July 2016). URL: `https://twiki.cern.ch/twiki/bin/view/AtlasPublic/TauPublicCollisionPlots`.

[90] ATLAS Collaboration. Approved tile calorimeter plots, 2016. Cosmics/Single beam, Calibrations, Testbeam, Upgrades. URL: `https://twiki.cern.ch/twiki/bin/view/AtlasPublic/ApprovedPlotsTile`.

[91] E. Gross and O. Vitells. Transverse mass observables for charged Higgs boson searches at hadron colliders. *Phys. Rev.*, D81:055010, 2010. `arXiv:0907.5367`, `doi:10.1103/PhysRevD.81.055010`.

APPENDIX A

TAU RECONSTRUCTION

Tau (τ) leptons are the only flavor of lepton massive enough to decay hadronically, with $m_\tau = 1.78$ GeV. Since the proper decay length is only 87 microns, taus decay well before reaching the detector, so they must be reconstructed from their decay products. Hadronic decays produce a narrow energy deposit (with respect to QCD) in the calorimeter, associated with low track multiplicity (generally 1- or 3-"prongs", or tracks from charged pions) and 0 or more neutral constituents, with significant missing transverse energy carried away by the neutrino. Therefore, we can directly measure only the hadronic component, referred to as $\tau_{\text{had-vis}}$.

Hadronic tau reconstruction is seeded by an anti-k_t jet with $\Delta R = 0.4$, $|\eta| < 2.5$, and $p_{\text{T}} > 10$ GeV. In events with pileup, the default primary vertex does not always correspond to the vertex at which the tau lepton was produced. The Tau Vertex Association algorithm uses tracks in a $\Delta R = 0.2$ cone around the seed jet direction to identify the primary vertex associated with the tau. The p_{T} of the tracks is summed, and the vertex with the largest fraction of the sum is selected as the tau vertex. The tau vertex is used to determine the direction of the visible tau decay products, define the coordinate system used to recalculate impact parameters and identification variables, and perform track selection. The performance of tau reconstruction is summarized in Figure A.1.

Tracks are associated with the tau if they meet the following criteria: they must be within $\Delta R < 0.2$ of the tau jet center, with $p_{\text{T}} > 1$ GeV, 2 Pixel hits (with the Insertable B-Layer), 7 Pixel + Semi-Conductor-Tracker hits, $d_0 < 1.0$ mm, and with $|z_0 \sin\theta| < 1.5$ mm. This selection is designed to maximize the fraction of 1-prong and 3-prong taus reconstructed with the correct number of tracks. The leading source of underestimation of tracks is from tracking inefficiency due to hadronic interactions in the inner detector. The leading source of overestimation of tracks is from photon conversion tracks that fulfill the track selection criteria.
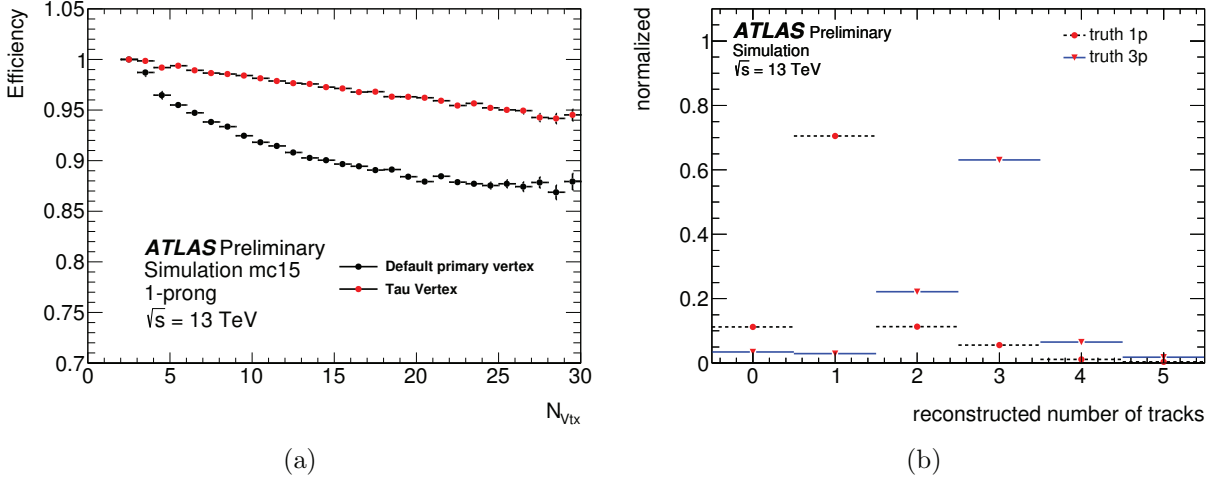
(a) Efficiency for correct production vertex assignment in 1-prong tau decays for the tau reconstruction algorithm and the default choice of the vertex with the highest Σp_T^2, as a function the number of reconstructed vertices in the event, and (b) the number of reconstructed tracks for $\tau_\mathrm{had\text{-}vis}$ candidates from true 1-prong and 3-prong tau decays. [88]

Figure A.1: Tau production vertex and track reconstruction efficiency.

A Boosted Decision Tree (BDT)-based identification is used to distinguish taus from other sources of hadronic jets.

Working points (shown in Figure A.2)are defined for 60 (50), 55 (40) and 45 (30) % reco+ID efficiency for 1-prong (3-prong) taus, with efficiencies approximately constant vs p_T and pileup. Separate BDTs are trained for 1-prong and 3-prong taus on $Z/\gamma \to \tau\tau$ signal and dijet backgrounds. Identification (ID) variables constructed from tracks and topological calorimeter clusters (topoclusters) in the $\Delta R < 0.2$ core region and corrected for pileup. Electron ID is relevant to the discrimination between electrons and taus. If an electron is found within $\Delta R < 0.4$ of a tau, with a log-likelihood (LLH)-based electron ID score above threshold, then the tau is rejected. The nominal working point for electron rejection is defined for 95% tau ID efficiency.

(a)

(b)

(c)
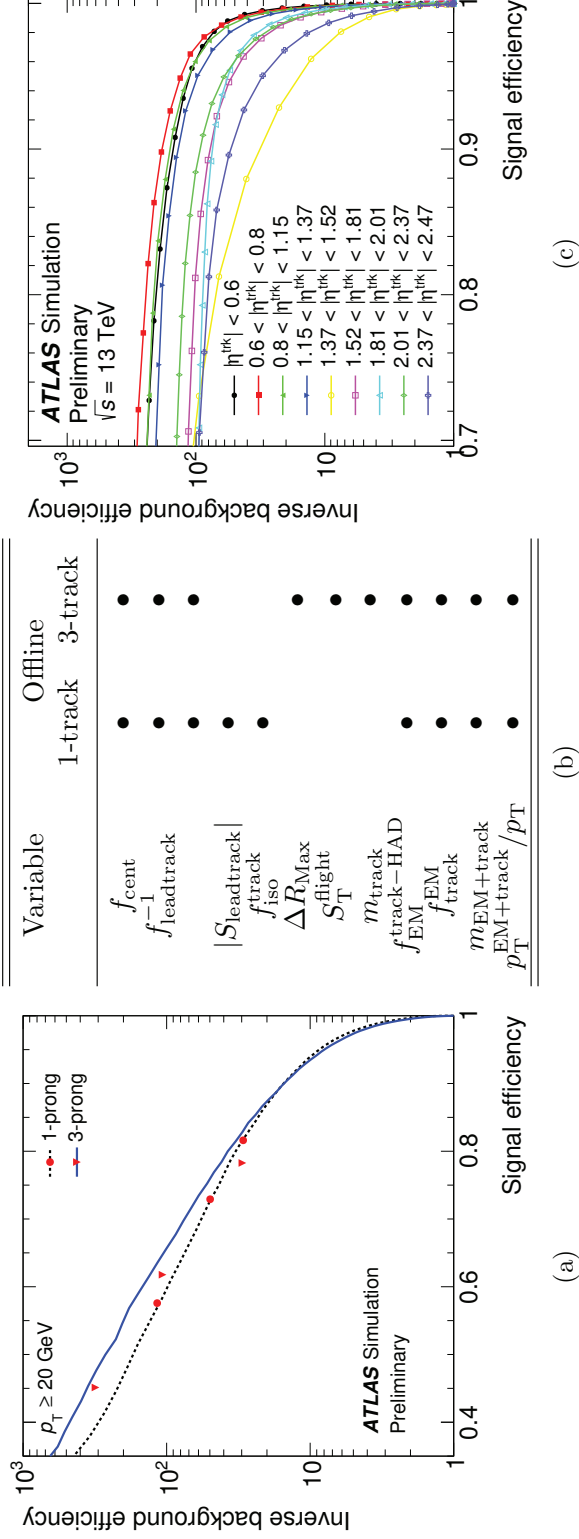
(a) Inverse of the efficiency for mis-tagging QCD jets as a function of the identification efficiency for $\tau_{\text{had-vis}}$ candidates. The two lines refer to 1-track and 3-track candidates. The EM Loose, EM Medium, and EM Tight working points are shown on these lines. The working points do not stay exactly on the line because they implement variable cuts to achieve a reduced p_{T}-dependency of the efficiency. (b) Discriminating variables used as input to the tau identification algorithm at offline reconstruction and at trigger level, for 1-track and 3-track candidates. The bullets indicate whether a particular variable is used for a given selection. The $|S_{\text{leadtrack}}|$ and $S_{\text{T}}^{\text{flight}}$ variables are calculated with respect to the beam line in the trigger. (c) The inverse of electron mis-identification efficiency as a function of the tau identification efficiency for different $|\eta|$ regions. The nominal working point corresponds to a tau identification efficiency of 95%. [88]

Figure A.2: Tau identification and working point selection.

Tau Energy Scale (TES) calibration applies a correction of the form $E_{\text{calib}} = \frac{E_{\text{LC}} - E_{\text{pileup}}}{R(E_{\text{LC}} - E_{\text{pileup}}, \eta, n_p)}$, where E_{LC} is uncalibrated energy, and n_p is the number of prongs in the tau decay. E_{pileup} is a pileup correction found to be linear with the number of vertices in the event, and R is a function that accounts for variations in detector response due to calorimeter thresholds, and decay products not reaching the calorimeters or falling outside the tau cone. This factor is extracted as the Gaussian mean of $(E_{\text{LC}} - E_{\text{pileup}})/E_{\text{true}}^{\text{vis}}$, and energy resolution is computed as the Gaussian width of $E_{\text{calib}}/E_{\text{true}}^{\text{vis}}$.

Performance of the online (trigger) and offline tau identification and the energy calibration are measured using $Z \rightarrow \tau\tau$ events selected from the data. Semileptonic events, where one tau decays to a muon and the other hadronically, are used to select data events with a high purity of true hadronic decays of taus, as shown in Figure A.3. Electron rejection is measured in $Z \rightarrow ee$ events.

Contribution

I acted as one of the tau software domain experts for approximately the period I was at CERN – around early 2013 to mid 2016 – with some ramp up and ramp down at the start and end of that period. My focus was on the tau reconstruction code and related tools. This involved a wide range of software support and maintenance activities during this period, from bug fixes and status reports to implementing new algorithms and presenting at software tutorials, as well as participation in a number of ATLAS-wide software efforts.

The most significant tasks during the LS1 period were the Eigen[1] and xAOD[2] migrations, as part of the ATLAS-wide efforts towards Run 2 readiness. The former involved rewriting

---

[1] A matrix algebra library, having previously used CLHEP, see: <eigen.tuxfamily.org>

[2] A new format for analysis object data.
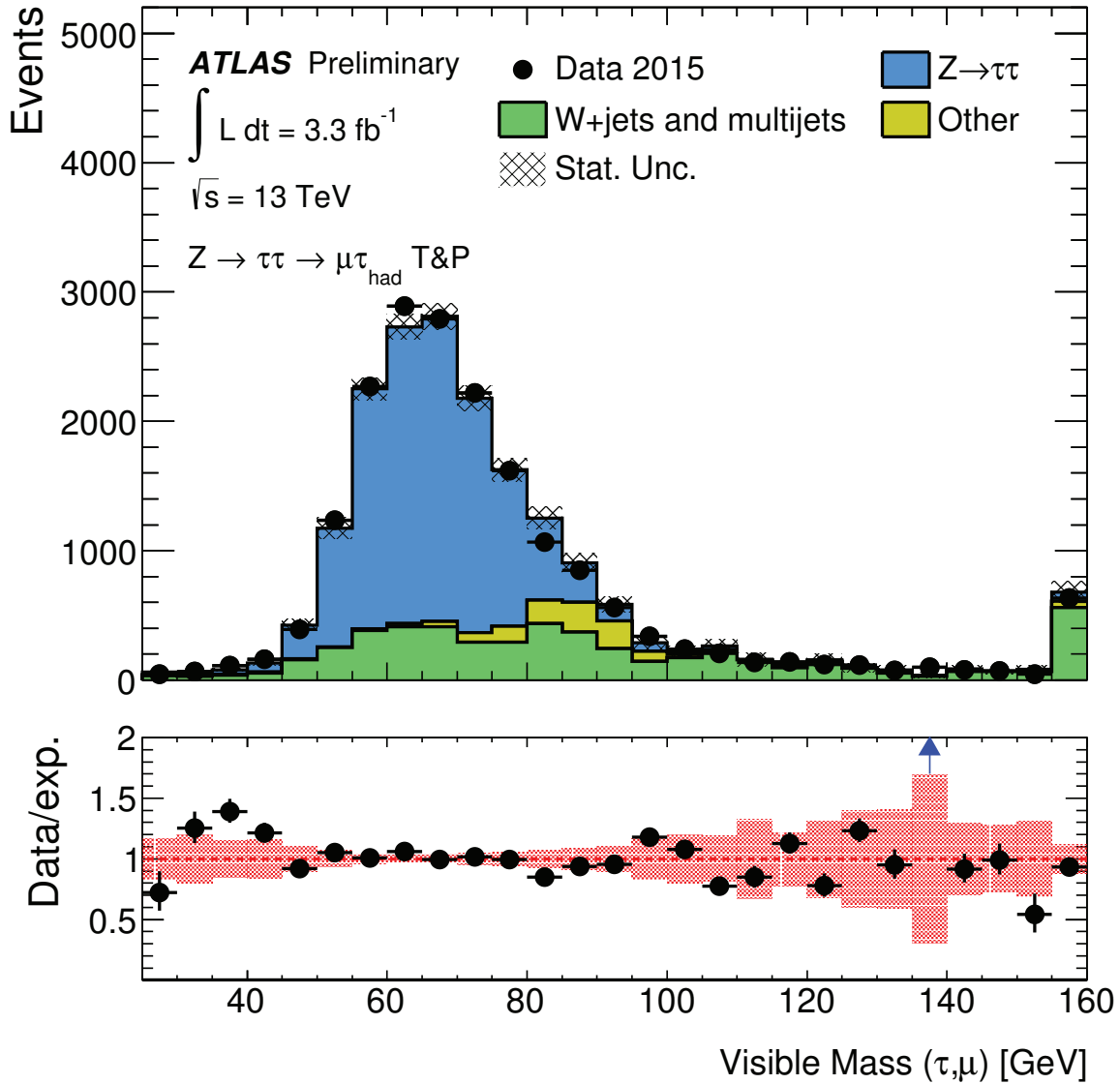
The Z mass peak is observed in an enriched sample of $Z \to \tau\tau \to \mu\tau(\mathrm{had})$ events from the 2016 dataset in 13 TeV collisions, corresponding to an integrated luminosity of 7.1 fb^{-1} [89]. These events are collected using a single-muon trigger. Event selections and background estimations are described in [52]. Only statistical uncertainties are shown.

Figure A.3: The visible mass reconstructed using isolated muons and offline tau candidates passing the offline loose identification requirement.

portions of the ATLAS reconstruction software to use the Eigen library for vector and matrix algebra, instead of the Class Library for High-Energy Physics (CLHEP), as part of the effort to reduce CPU usage in Run 2. These changes, while numerous, were relatively straightforward for the most part, so I was able to make quick work of nearly the entire tau domain.

The xAOD migration was a great deal more involved. In run 1, reconstructed physics events were saved in the Analysis Object Data (AOD) format, with derived physics data stored in a simpler D3PD format for most analyses. The migration to xAOD was part an effort to use a simpler event data model for in-memory objects, which can more easily be stored on disk. Among other things, this reduces the on-disk size of physics data and makes it easier to possible to work with the xAODs without needing the full ATLAS software environment. As this was a larger migration effort, it required more manpower, with the tau migration team consisting of myself, Felix Friedrich, and Michel Janus.

As a results of the xAOD migration, it became possible to read physics data from (D)xAOD files in either the ATLAS athena software environment, or in a standalone ROOT environment. Because athena can be resource intensive and difficult to work with at an analysis level, analyzers prefer to work in standalone ROOT, so an Analysis Base Release set of tools was written to accommodate this. By the end of LS1, it was apparent that there was some interest in running at least a portion of tau reconstruction and calibration in the ABR–referred to as making the tools dual-use. So, beginning near the end of LS1 and extending into Run 2, I began working along side Justin Griffiths and Dirk Duschinger on the dual-use tool migration. This was while my involvement in the tau domain was ramping down, so I did not get to see much day-to-day use out of this effort, but by the end of my time there it was possible (if a little impractical) to re-run many parts of the reconstruction and calibration chain from ROOT.

APPENDIX B

TILE DATA QUALITY

Tile monitoring includes identifying and masking problematic channels (Figure B.1), correcting for timing jumps, monitoring data corruption or other hardware issues, and (since 2015) monitoring and correcting for changes in pedestal. Immediately after a physics run ends, a subset of data, called the "Express Stream", is processed and reviewed. There is a short delay, known as the calibration loop, which typically lasts 48 hours, before the full dataset is processed, during which any problems identified in the express stream may be corrected with or accounted for in conditions updates. Changes to Tile timing within collision runs are monitored by Laser calibration events in the empty bunch crossings of physics runs, used to apply timing offset corrections to data.

The Tile Data Quality Validator (DQV) remote shifter reviews the express stream processing of each run to check for any issues. Tile uses a specialized web interface to generate an initial report for the shifter to finish, based on the results of automated data quality monitoring tests. The Tile Data Quality Leader (DQL) shifter reviews the DQV's report and takes any necessary action. If a problem cannot be corrected, it is entered into the ATLAS Defect database. If the problem is considered intolerable, then the affected data are removed from the ATLAS Good Run List and are not used in physics analyses.

A fraction of Tile data losses in Run 1 were related to sporadic tripping of Low-Voltage Power Supply (LVPS) units, including changes to timing after trip recovery (Figure B.2). Redesigned LVPS units were tried on a part of the detector in 2012, and found to virtually eliminate the problem. All older units were then replaced by the new ones during Long Shutdown 1 (2013-2014). This exercise is also thought to have led to a significant reduction in the number of bad channels from Run 1 to Run 2, as well as a reduction in timing jumps. Tile achieved 100% DQ efficiency in 2015, with minor ($< 1\%$) losses by the start of October, 2016.
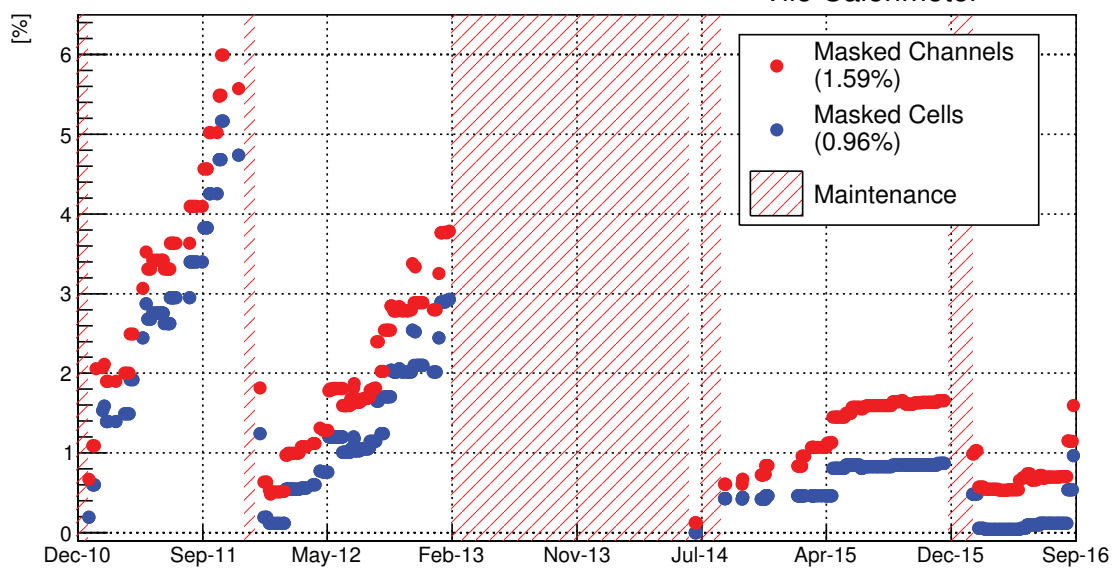
The stability improvement from the start of 2015 correlates with the installation of new Low Voltage Power Supplies (LVPS) during the long shutdown period (2013-2014). [90]

Figure B.1: Time evolution of masked Tile cells and channels.
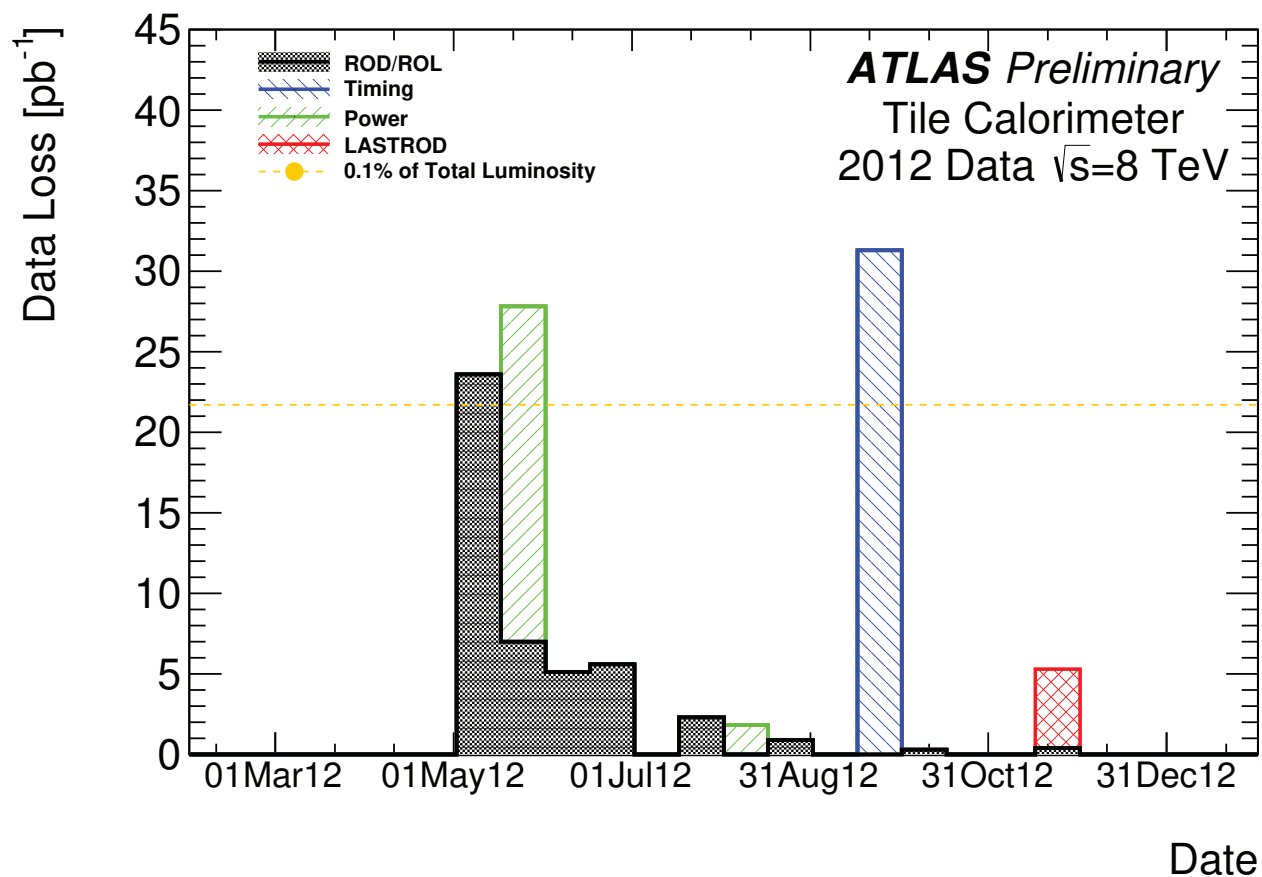
Some losses, including power cuts and timing jumps, are correlated with LVPS trips. [90]

Figure B.2: Data losses during the $\sqrt{s} = 8$ TeV data taking period (2012).

Contribution

My main contribution to Tile was serving as one of the two data quality co-coordinators, along side Tibor Zenis as the other co-coordinator, from the start of 2014 until the end of 2015. I continued some involvement in Tile DQ for the first half of 2016, as I prepared to return to the US and Puja Saha began to take over.

As the on-site coordinator, I was tasked with providing instruction and assistance to the DQL shifter, giving the final report and sign-off of each run at the weekly ATLAS Data Quality Meetings, and managing the overall Data Quality effort. This included convening weekly Tile DQ meetings to discuss ongoing issues and tool development. I also maintained several of the DQ scripts and tools, including the web interface used by DQV shifters to check and report on collision runs. There were no collisions to check during the LS1 period, so the DQ activities were limited to calibration runs, with a particular emphasis on identifying issues for the maintenance team to fix as part of the LS1 consolidation effort.

I also briefly acted as the administrator of the Tile Conditions Database, for an approximately 6 month period at the end of 2013 and beginning of 2014, between the departure of the previous database expert (Guillherme Lima) and the hiring of a permanent replacement (Yuri Smirnov).

APPENDIX C

MOTIVATION FOR BDT

Historically, $m_T(\tau, E_T^{\text{miss}})$ has been used as a discriminant variable in charged Higgs analyses. In the $\tau + $ jets channel, there is a physical interpretation to this variable: the only significant sources of E_T^{miss} are from the prompt ν_τ produced by the $H^\pm$ decay, and a second ν_τ in the hadronic tau decay. As a result, in the absence of detector resolution or particle misidentification effects, $m_T(\tau, E_T^{\text{miss}})$ has a kinematic edge at $m_{H^\pm}$.

The situation in the $\tau + \ell$ channel is not a good. Another neutrino is produced by the leptonic portion of the associated top quark decay, which contributes significantly to $E_T^{\text{miss}1}$.

In principle, the 4-momentum components of the ν_ℓ can be constrained by the kinematics of the top decay, the masses $m_\nu (= 0)$, m_W, and m_t, and the observable ℓ and b-jet decay products, using the procedure described in [91].

The procedure is briefly summarized as follows. First, define:

$$\mathbf{A_1} = \begin{pmatrix} E^{\bar{b}} & -p_z^{\bar{b}} \\ E^{l^-} & -p_z^{l^-} \end{pmatrix}, \ \mathbf{A_2} = \begin{pmatrix} -p_x^{\bar{b}} & -p_y^{\bar{b}} \\ -p_x^{l^-} & -p_y^{l^-} \end{pmatrix},$$

$$\eta = \begin{pmatrix} E^{\bar{\nu}_\ell} \\ -p_z^{\bar{\nu}_\ell} \end{pmatrix}, \ \xi = \begin{pmatrix} p_x^{\bar{\nu}_\ell} \\ p_y^{\bar{\nu}_\ell} \end{pmatrix}, \ m = \frac{1}{2} \begin{pmatrix} m_{\text{top}}^2 - m_W^2 - m_{\ell b}^2 + m_\ell^2 \\ m_W^2 - m_\ell^2 \end{pmatrix}$$

where $m_{\ell b}^2$ is the mass squared of the $\ell + b$ system. The constraints from the parent particle and neutrino masses can then be written, respectively, as:

$$\mathbf{A_1}\eta + \mathbf{A_2}\xi = m \tag{C.1}$$

$$\eta^T g \eta + \xi^T \xi = 0 \tag{C.2}$$

where g is the $1 + 1$ Lorentz metric. These equations are solved by:

---

[1] As the neutrino comes from the associated top, this contribution is relatively insensitive to $m_{H^\pm}$, while the contribution from $H^\pm$ is very sensitive to mass. As a result, the effect is expected to be more significant at low masses, which would unfortunately degrade $\tau + \ell$ performance in the region where it is most critical.

$$\xi_\pm(\phi) = \mathbf{L}^{-1}(\pm\sqrt{Q}\hat{r}(\phi) - \omega) \tag{C.3}$$

where:

$$\mathbf{A} = \mathbf{A_1}^{-1}\mathbf{A_2},$$

$$\mathbf{L}^T\mathbf{L} = 1 - \mathbf{A}^T g\mathbf{A}, \text{ via the Cholesky decomposition,}$$

$$Q = |\mathbf{L}\xi + \omega|^2 = \omega^T\omega + \tilde{m}^T g\tilde{m},$$

$$\omega = (\mathbf{L}^T)^{-1}\mathbf{A}^T g\tilde{m},$$

$$\tilde{m} = \mathbf{A_1}^{-1}m$$

Each solution is parameterized in terms of a free variable ϕ. Following from the definition of ξ, interpreting it as the contribution to the $E_\mathrm{T}^\mathrm{miss}$ from the ν_ℓ in the leptonic top decay, we can subtract this term from the total $E_\mathrm{T}^\mathrm{miss}$ to obtain a corrected transverse mass variable for a given ϕ hypothesis. We then define $M_T^{H^\pm\text{-min}}$ by selecting the ϕ parameter which minimizes[2] the resulting transverse mass. At the parton level, this has the property $M_T^{H^\pm\text{-min}} \leq M_T^{H^\pm\text{-truth}} \leq m_{H^\pm}$ – there is a kinematic edge at the charged Higgs mass.

This sounds nice, but in practice, detector resolution effects and imperfect particle identification leads to some smearing of the distribution[3]. We decided to test an MVA approach instead, using this variable as one of the inputs. This variable was eventually dropped, as it was found not to increase sensitivity[4] when compared with including the kinematic variables use in the computation.

A number of different MVA approaches were considered. I ultimately decided to go with a BDT model using stochastic gradient boosting. Other models that were considered include

[2]The $\pm$ sign in $\xi_\pm$ is equivalent to a phase shift in ϕ, so it can be dropped during the minimization.

[3]This is, unfortunately, also more significant at low masses.

[4]The area under the receiver operating characteristic (ROC) curve was used as a metric.

neural networks, support vector machines and kernel vector machines, and several variations of random forests.

A Neural networks (NNs) can be modeled as a graph of nodes linked together. A relatively simple model to understand, in my opinion, is a feed forward NN. Such a NN is built from multiple layers of nodes. Nodes within a layer are connected to all nodes in the previous or next layer, but never with nodes in the current layer, and the number of nodes per layer need not be the same. The first layer is used as an input layer, where the input features are fed into the NN. Links to the next layer are weighted, with the input at each node being from the sum of the products of each link weight times the activation in the previous node. The node's input is then passed through an activation function, typically with a sigmoid shape, such as tanh. The last layer is used as an output layer, where the activation of a small number of nodes is used to, in this example, classify events as signal-like or background-like.

Training a NN consists of defining link weights such that the output layer produces the expected results. There are multiple approaches, but the general trend is that NN tend to be slower to train than the other models that were considered. Modern NN are known for preforming well when given a large number of low-level features. While this is useful for many problems, it doesn't align well with the analysis at hand, so it wasn't considered further.

Support vector machines (SVMs) find the boundary that maximizes the margin of separation between data points in some space. In practice, many problems are not linearly separable, so it is useful to lift the points into a higher dimensional space where the classes become linearly separable. While an explicit transformation into such a space is possible, the transformation itself is unnecessary, as only the distance between points is significant when finding the hyperplane. The kernel trick is used to define an inner product space which lifts to a higher dimension.

While I like SVMs in general, and think it could be adapted to work well in an analysis such as this, I wasn't happy with any of the implementations I encountered when running preliminary tests. The list of available kernel functions is often short and not easily extended. The kernel functions that are available, including the popular Gaussian radial basis function, tend to be sensitive to the scale and distribution shape of the input variables, so significant work can be required to transform the inputs into something appropriate to the problem. The training process also tends to scale worse than linear with training set size, which can theoretically become problematic given the large background dataset size in this analysis. While none of these problems are insurmountable, some quick tests suggested that in aggregate it was impractical for the analysis workflow, given the performance and speed of other methods.

Several tree-based ensemble methods were considered, including a few different BDT and random forest (RF) implementations. In contrast to BDTs, RFs grow the decision trees until classes are fully separated, and use a random sub-sampling of events per tree, and a randomized cut strategy[5], to achieve statistical independence. The RF approaches seemed to work well on test problems with larger training dataset sizes, but I observed larger error rates when training set sizes were small. The resulting models tended to be larger – both in terms of the number of trees and the size of each tree – than the BDT approaches. This causes the RF models to be slower to apply, by a noticeable margin, than the other models considered. Given the large number of systematic variations which must be scored by the MVA, I had concerns that this would become a bottleneck in the analysis.

---

[5]There are several variations of this, depending on the implementation. The base line example is to select a random subset of features, and greedily optimize the cuts election over that subset. Some variations also randomize the cut values, and then select which ever variable happened to achieve the best separation with a random cut.

BDTs tended to perform the better on small training sets, and the resulting MVA was faster to apply. Even so, additional steps were needed[6] to deal with the limited signal statistics. Gradient boosting seemed to give the same or better separation than adaptive boosting in early tests on the analysis dataset. The FastBDT library was ultimately selected because of a number of convenience factors. In particular, I saw slightly better separation than with the TMVA implementation of gradient boosting, but it was still usable via a TMVA plugin[7], and it benchmarked significantly faster at both training and application than its TMVA counterpart. Using a faster implementation made it easier to optimize the BDT hyperparameters and test different combinations of training features, which otherwise fall somewhere between difficult and impractical, depending on the approach used, due to the computational cost and manpower requirements.

---

[6]Such as by grouping signal samples into kinematically similar mass ranges, and using the k-fold method with $k = 5$ instead of the more common $k = 2$.

[7]While I don't personally care about TMVA support, the first thing every MVA analysis is asked is to show sets of plots that TMVA produces automatically, so this saves some time.

APPENDIX D

ADDITIONAL VALIDATION PLOTS

The data/background modeling of each variable is validated in the control regions where the relevant objects are present. In particular, b-jet variables are validated in the Dilepton b-tag control region (Figure D.1), and τ variables are validated in the $\tau + \ell$ b-veto regions (Figure D.2). Variables that depend only on E_T^{miss} and e or μ are validated in all control regions (Figures D.3, D.4).

The Υ variable is, to within constant factors, equivalent to one of the τ-ID variables used to define working points. As a result, the data driven jet $\to \tau$ fakes have a biased Υ distribution by default. A Smirnov transformation is applied to map the cumulative distribution function (CDF) of anti-selected τ leptons in the fake factor regions onto the distribution for events passing the nominal τ selection. This transformation is then applied in the signal region and other control/validation regions to correct for the selection bias. [19]

The BDT score distribution for each mass bin is validated in the control regions. In the Dilepton b-tag region (Figure D.5), τ are not selected, and both e and μ are in the event. By construction, b-jets are not expected in the b-veto region (Figure D.6). When an object is missing, BDT variables are calculated with respect to a default (zero) Lorentz vector. The Υ variable is also set equal to zero in events without τ objects. In the dilepton regions, the p_T, η, and ϕ of the lepton is taken as the sum of those components of the e and μ. Neither the handling of missing variables nor the BDT score distributions in control regions are meant to be physically meaingful, but the BDT scores are expected to preserve data/background modeling, due to the consistent treatment of missing variables for data and background.
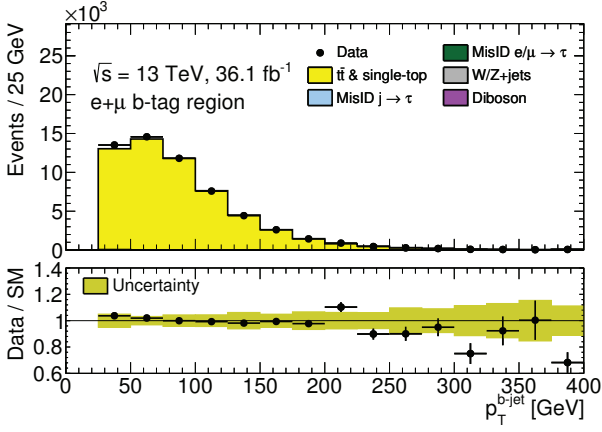
(a) $p_T^{b\text{-jet}}$
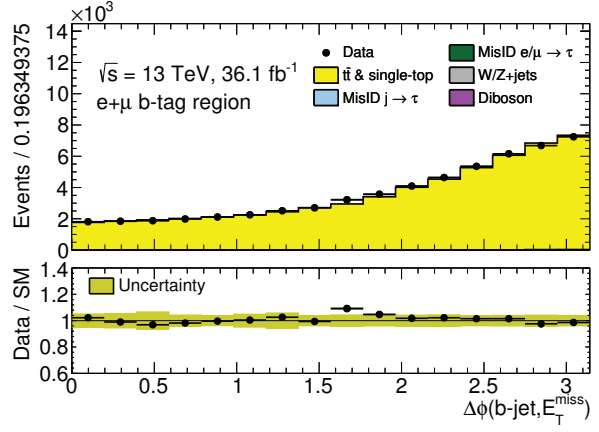
(b) $\Delta\phi(b\text{-jet}, E_T^{\text{miss}})$
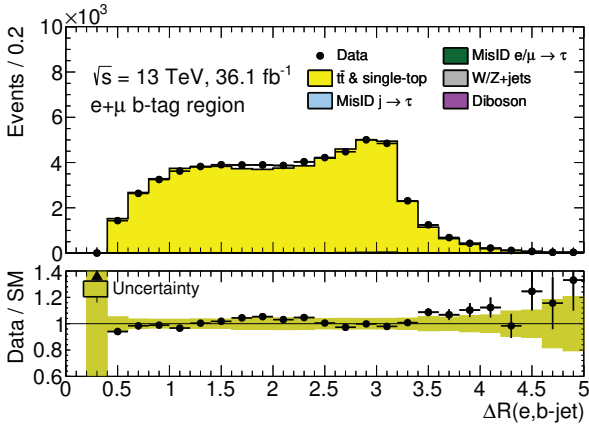
(c) $\Delta R(b\text{-jet}, e)$
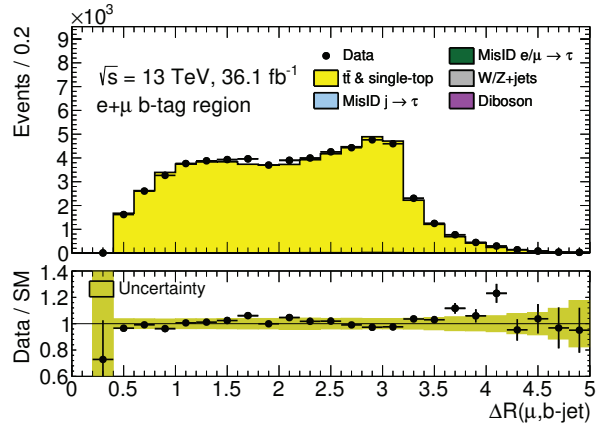
(d) $\Delta R(b\text{-jet}, \mu)$

Figure D.1: Features involving b-jets, in the $e + \mu$ b-tag control region.

(a) p_T^τ

(b) Υ
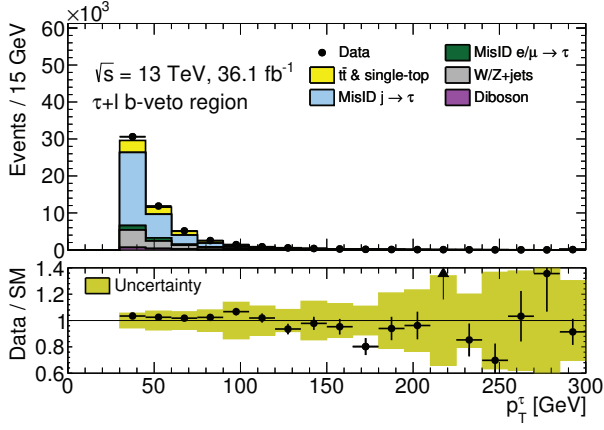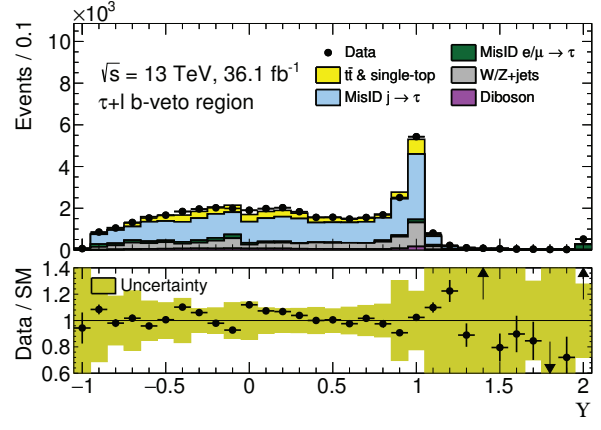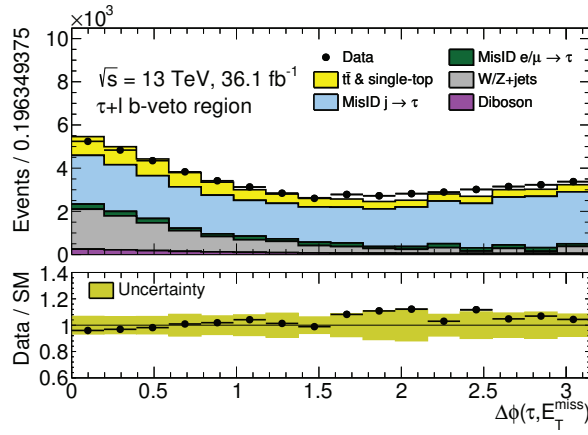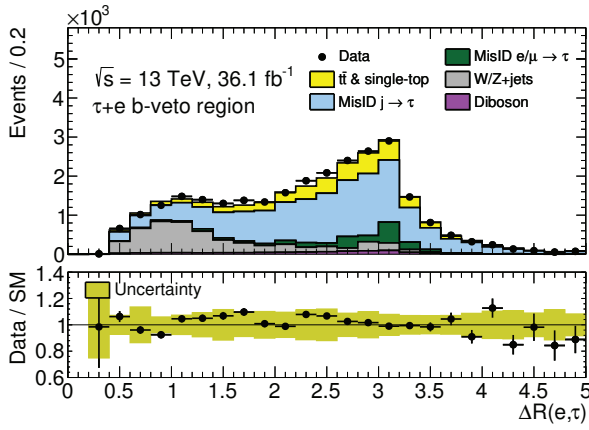
(c) $\Delta\phi(\tau, E_T^{\mathrm{miss}})$

(d) $\Delta\mathrm{R}(\tau, e)$
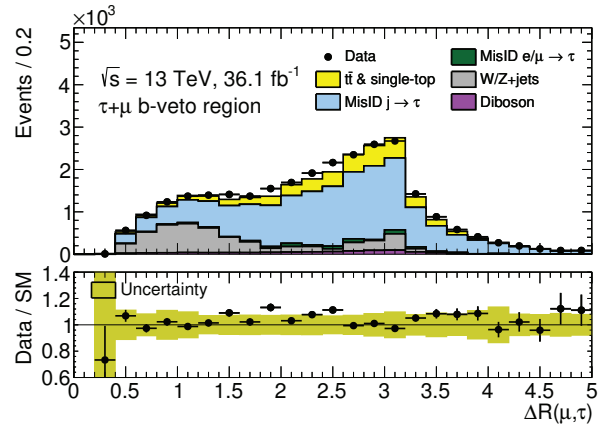
(e) $\Delta\mathrm{R}(\tau, \mu)$

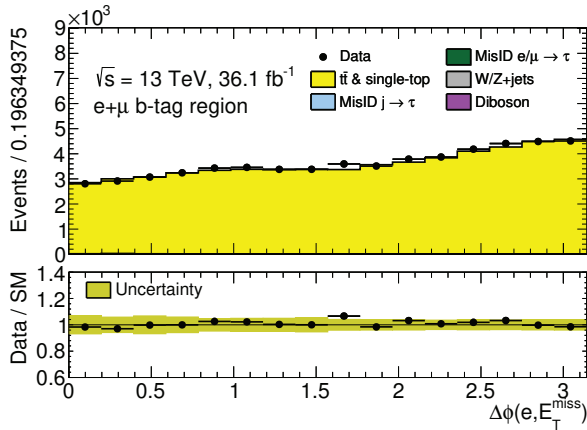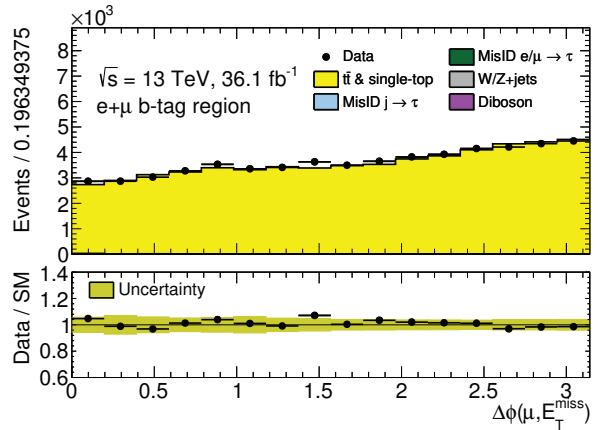Figure D.2: Features involving τs, in the $\tau + \ell$ b-veto control regions.

(a) p_T^e

(b) p_T^μ
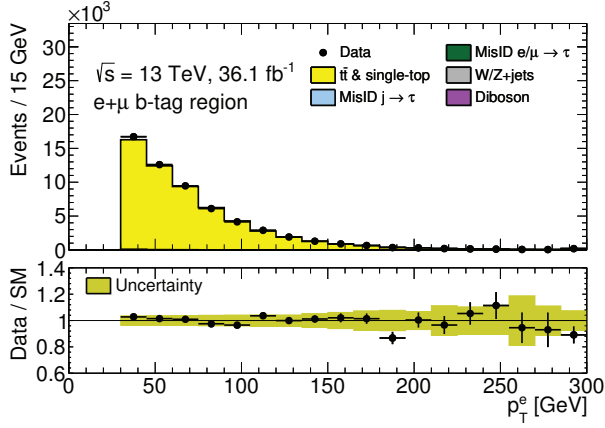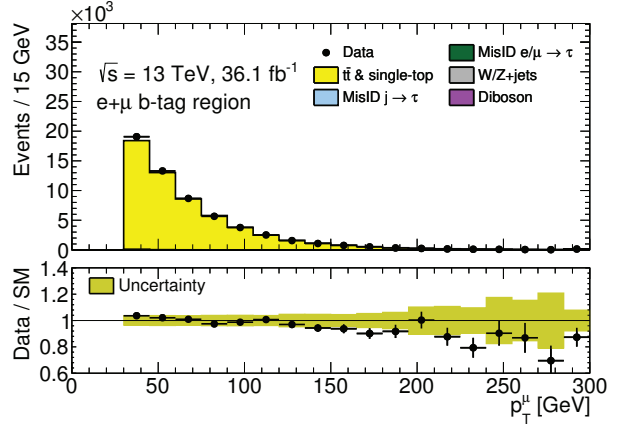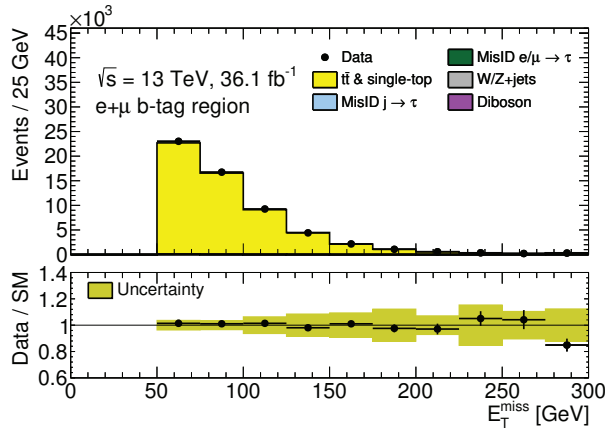
(c) $E_\mathrm{T}^\mathrm{miss}$

(d) $\Delta\phi(e, E_\mathrm{T}^\mathrm{miss})$

(e) $\Delta\phi(\mu, E_\mathrm{T}^\mathrm{miss})$

Figure D.3: Additional features in the $e + \mu$ b-tag control region.

(a) p_T^e

(b) p_T^μ
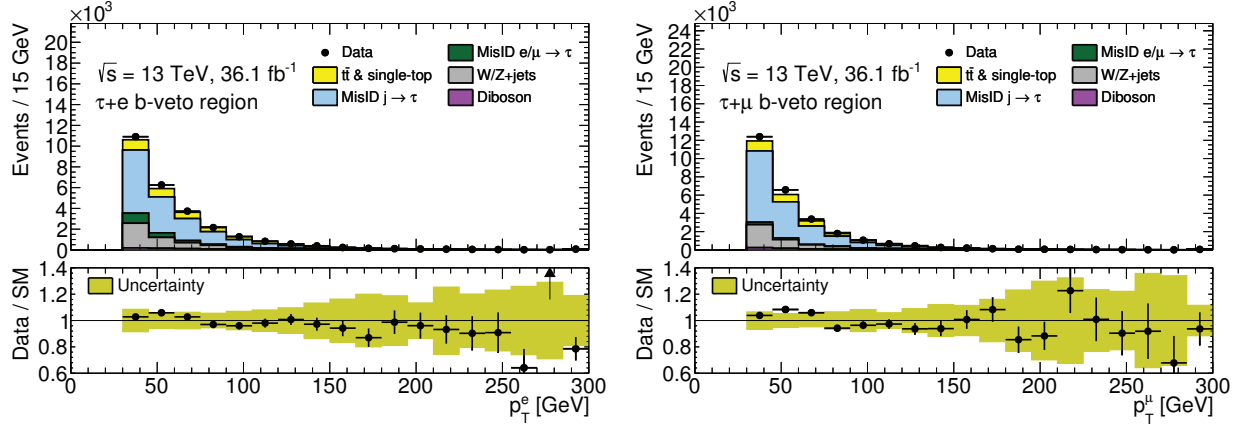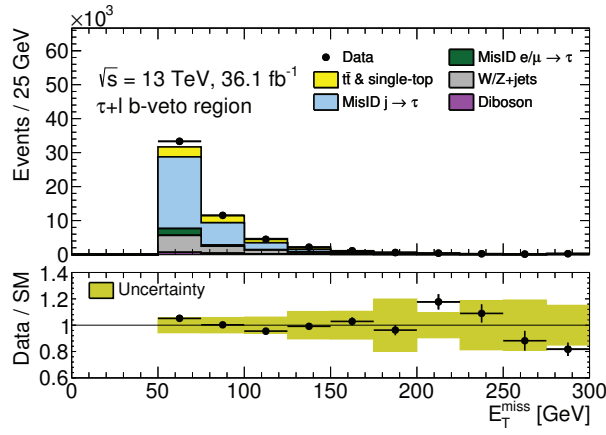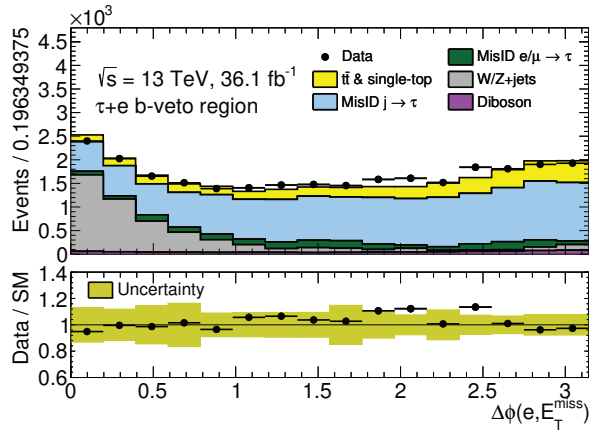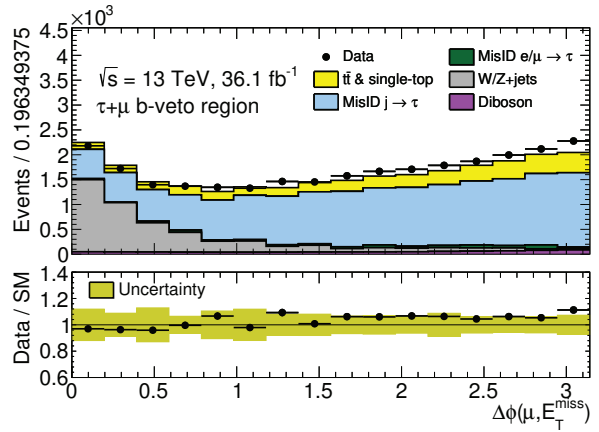
(c) E_T^{miss}

(d) $\Delta\phi(e, E_T^{\mathrm{miss}})$

(e) $\Delta\phi(\mu, E_T^{\mathrm{miss}})$

Figure D.4: Additional features in the $\tau + \ell$ b-veto control region.
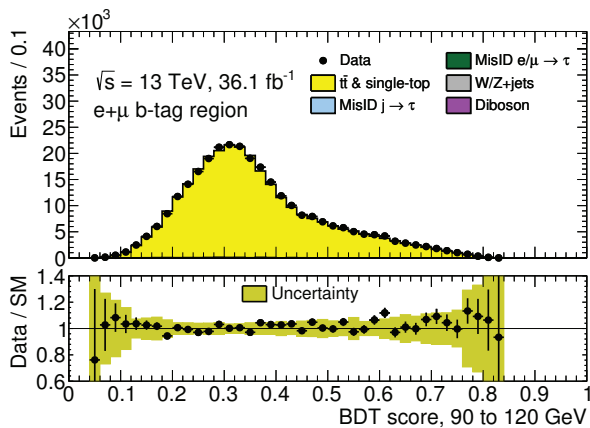
(a) $e + \mu$ b-tag CR 90–120 GeV
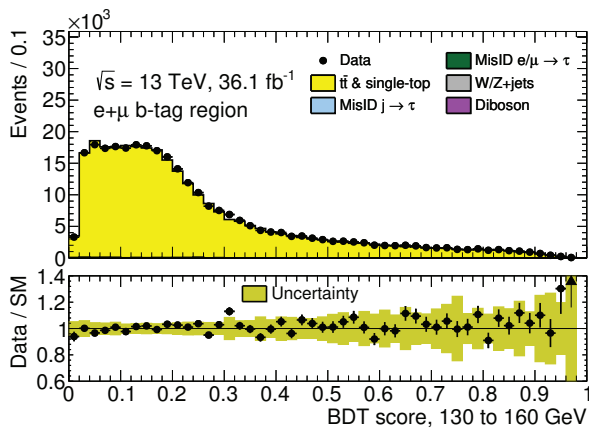
(b) $e + \mu$ b-tag CR 130–160 GeV
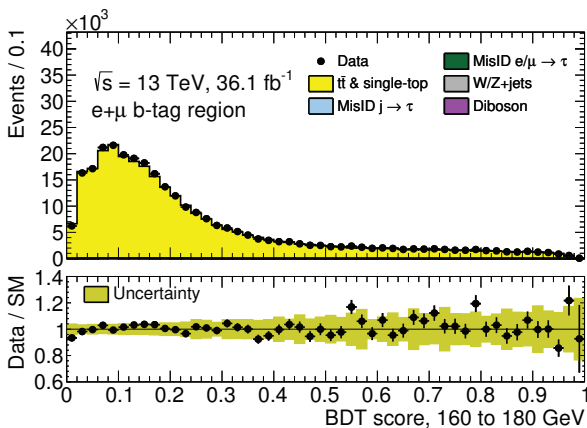
(c) $e + \mu$ b-tag CR 160–180 GeV
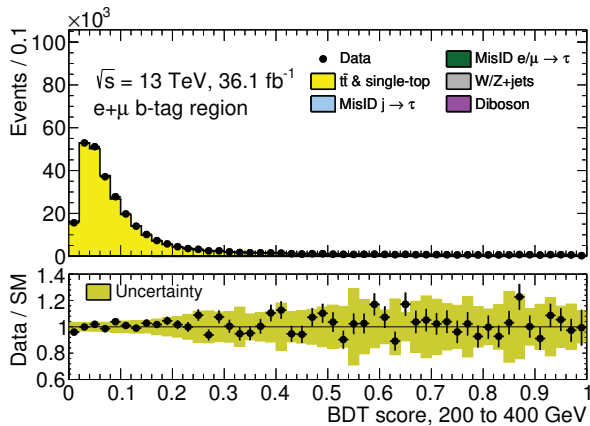
(d) $e + \mu$ b-tag CR 200–400 GeV
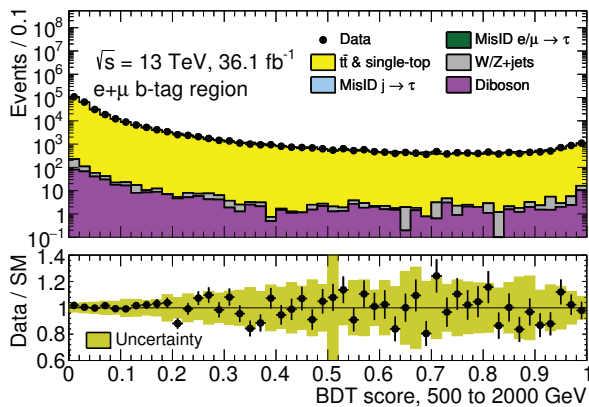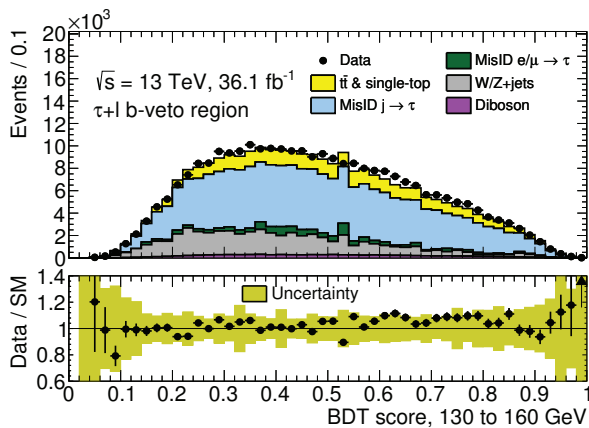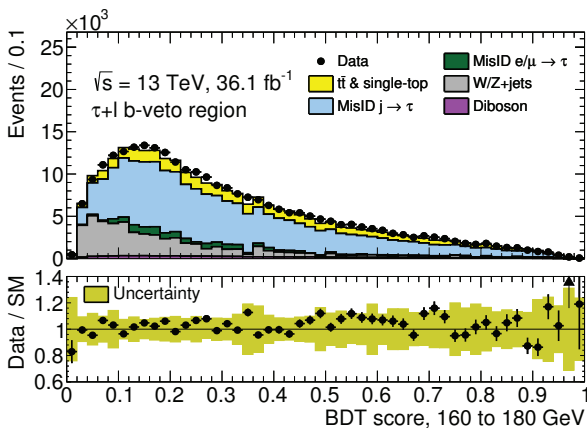
(e) $e + \mu$ b-tag CR 500–2000 GeV

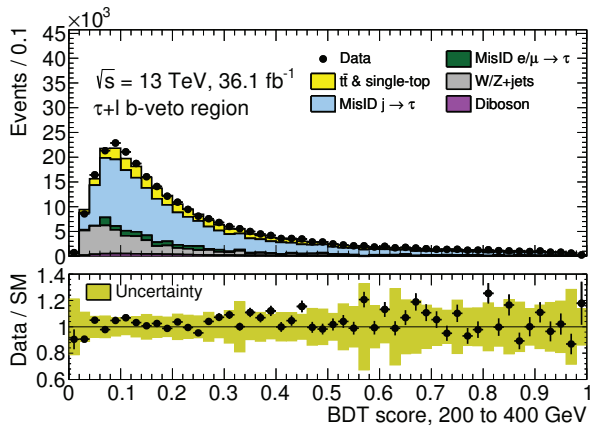Figure D.5: BDT scores in the $e + \mu$ b-tag control region.
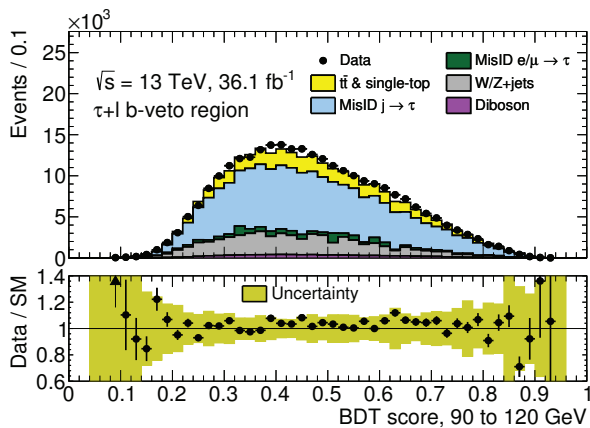
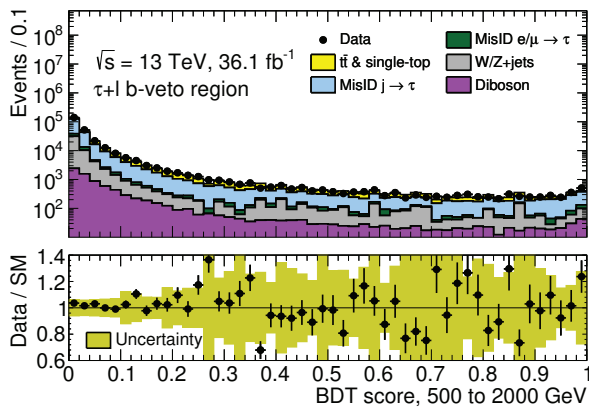(a) $\tau + \ell$ b-veto CR 90–120 GeV

(b) $\tau + \ell$ b-veto CR 130–160 GeV

(c) $\tau + \ell$ b-veto CR 160–180 GeV

(d) $\tau + \ell$ b-veto CR 200–400 GeV

(e) $\tau + \ell$ b-veto CR 500–2000 GeV

Figure D.6: BDT scores in the $\tau + \ell$ b-veto control region ($\ell = e$ or μ).